design and development of a vibrating sample magnetometer for high magnetic field measurements of superconductors

Robert Luscombe

Luscombe, Robert (1994) design and development of a vibrating sample magnetometer for high magnetic field measurements of superconductors. Masters thesis, Durham University.

Design and Development of a Vibrating Sample Magnetometer for High Magnetic Field Measurements of Superconductors.

by

Robert Luscombe

A Thesis submitted in partial fulfilment of the requirements for the degree of Master of Science.

University of Durham

Department of Physics

1994

To Roz

"In a strange sort of way I'm almost glad I had my ...... experience. I wouldn't like to repeat it, but I'm glad that it happened"
Andy McNab, "Bravo Two-Zero"

Abstract

A Vibrating Sample Magnetometer (VSM) has been designed, constructed and developed. The design specification was for a VSM to work in magnetic fields up to 15T, and provide a variable temperature environment for the sample from 4.2K to 130K. A probe has been made to protect the detection coils and provide the variable temperature environment. The detection coils have been designed using computer modelling techniques such that a 4mm long sample may be measured. A low-field insert has been used to eliminate problems with flux jumping in the high field magnet system causing extremely high noise at magnetic fields below 2T. The VSM has been calibrated against a nickel standard in fields up to 15T. Considering electrical noise, the sensitivity of the VSM is 10^{-6}A.m^2. Hopefully, this may be improved upon by modifications made to the VSM that have not yet been fully tested. The temperature measurement is accurate to ±200mK from 4.2K to 30K in a liquid helium bath and from 77K to 130K in a liquid nitrogen bath. Outside these ranges it is necessary to use a temperature sensor mounted on the sample holder to ensure accurate temperature measurement.

The VSM has been used to study the superconducting properties of two single crystals of $YBa_2Cu_3O_{7-\delta}$ grown under identical conditions. This study was done in applied fields up to 220mT and at temperatures from 77K to 95K. It is shown from the transition temperature and the magnetisation critical current densities that the crystals do not exhibit identical superconducting properties. Some high field measurements have also been performed with the VSM. Studies of multifilamentary niobium-titanium wires have been made and the information has been used to modify and develop the VSM, as have measurements on a tape of $Bi_2Sr_2Ca_2Cu_3O_x$. Magnetic hysteresis of a multifilamentary $Bi_2Sr_2CaCu_2O_x$ wire has been measured at 4.2K and the magnetisation critical current density determined. This agrees well with transport critical current measurements.

Acknowledgements

Firstly I wish to acknowledge the Engineering and Physical Sciences Research Council (and formerly the Science and Engineering Research Council) for providing financial support for this work.

I wish to thank Professors A.D. Martin and D. Bloor for the use of the facilities of the Department of Physics and Dr. D.P. Hampshire who has been my supervisor throughout this research.

Many thanks are due to the following people who have assisted me greatly during this work:

Dr. L. Le Lay for assistance with the computerisation of the experiment, and along with Dr. C.I. Gregory, for useful discussions. F. Gencer and Dr. J.S. Abell at the U.K. National Growth Facility for Superconducting Oxides at the University of Birmingham for the $YBa_2Cu_3O_{7-\delta}$ single crystals; Dr.T.P. Beales of BICC Ltd. for supplying the $Bi_2Sr_2Ca_2Cu_3O_x$ tape; J.Tenbrink of Vacuumschmelze GmbH for supplying the multifilamentary $Bi_2Sr_2Ca_2Cu_3O_x$ wire.

Mr. P. Armstrong and his staff in the Student Workshop, Mr. G. Teasdale, Mr. M. Greener and Mr. P. Luke, without whose excellent work and cooperation this work could not have progressed so far. Without the efforts of Mr. C. Mulaney from the Electronics Workshop the VSM head would not have been fully operational.

Mr. G. Dixon and Mrs. P. Russell for preparation of some diagrams in this thesis. Mr. M. Lee and Miss. V. Greener for teaching me how to tame the Photocopier.

Mr. P. Foley, Mr. J. Dobson, Mr. W. Hogg and the staff of the Department's Main Workshop who have helped with many small technical jobs in the laboratories and provided excellent service with cryogenic liquids and gas cylinders.

Miss J. Bell, Mrs N. Bingham, Miss P. Carse, Miss C. Hedley, Miss R. Lumpkin and Mrs. L. Wilkinson for secretarial services and handling various orders and enquiries.

Salamat Ali, Chris Friend, Hamidi Hamid, Alton Horsfall, Tony Holland, John Hudson, John Makar, Caroline Moore, Ian Pape, Harry Ramsbottom and Stephen Westwood who have all made the Solid State Postgraduate Office such an interesting and exciting place to work.

Don Davison, Rorie Dempster, Paul Harley, Annette Harrison, Stuart Harrison, Peter Ratcliffe, Craig Robson and Jon Tait who have been valuable points of contact with the world outside physics!

My parents for supporting me during this work, and last but not least, Roz Vendy, whose endless encouragement and advice has been so invaluable.

Declaration

I declare that the work contained in this thesis has not been submitted for a degree at this University or any other. All work presented was conducted by the author unless stated otherwise.

Contents

1. Introduction

2. General Superconductivity

3. The Magnetic Properties of Superconductors.

4. The Durham Superconductivity Group Vibrating Sample Magnetometer.

5. Thermometry.

6. Low Field Magnetic Behaviour of Single Crystals of $YBa_2Cu_3O_{7-\delta}$.

7. High Field Magnetisation Measurements.

Appendix

1. Introduction.

1.1 History of Superconductivity.

Superconductivity was first discovered in Leiden in 1911 during studies of the resistivity of metals at very low temperatures. The resistance of pure mercury was found to drop catastrophically below the detectible limit [1] at a certain temperature known as the critical temperature, T_c, as shown in figure 1.1.

Since this discovery many elements and compounds have been found to be superconducting [3]. The progression in the maximum critical temperature is shown in figure 1.2. The rapid progression since the late 1980's was triggered when Bednorz and Müller made a Nobel Prize winning discovery [4] that the ceramic compound $Ba_xLa_{5-x}Cu_5O_{5(3-y)}$ was superconducting up to 30K.

True high temperature superconductivity (HTSC) was born when $YBa_2Cu_3O_{7-\delta}$ was discovered in 1987 [5]. This was the first compound with a critical temperature above 77K, the boiling point of the common cryogen liquid nitrogen. This has precipitated the discovery of many other groups of compounds with higher critical temperatures such as $Bi_2Sr_2Ca_2Cu_3O_x$ [6] ($T_c \approx 110K$), $Tl_2Sr_2Ca_2Cu_3O_x$ [7] ($T_c \approx 125K$) and $HgBa_2Cu_3O_{7-\delta}$ [8] ($T_c \approx 135K$).

1.2 Why study superconductivity?

The concept of zero resistance, and therefore persistent currents does raise some interesting scientific questions. What causes it? Why is it preferential to a resistive state? How can it be controlled? When does it break down?

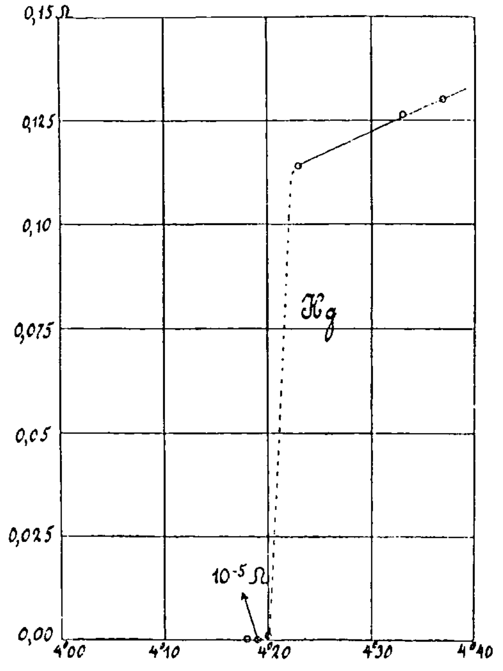

Figure 1.1 Drop in resistivity in mercury [1].

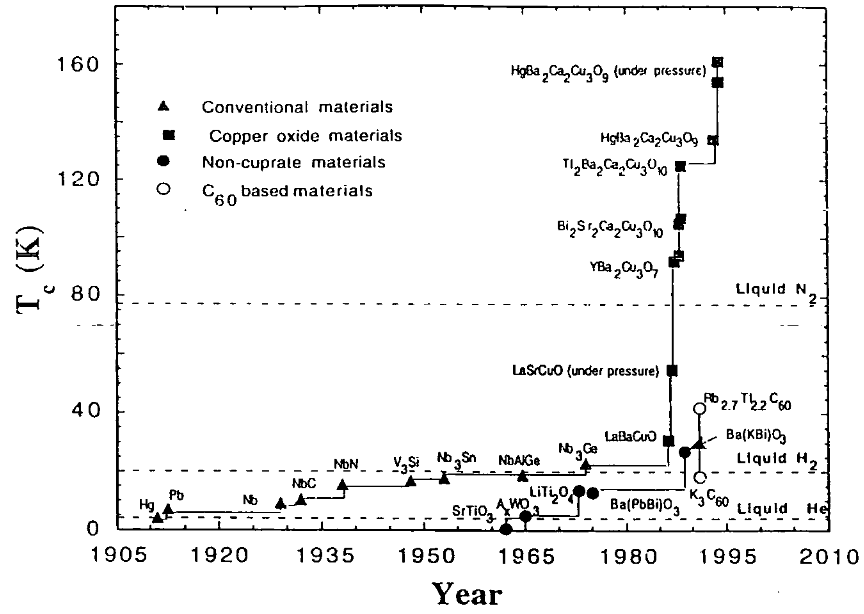

Figure 1.2 Progression in maximum critical temperature.

The possibility of industrial applications has led to much investment in superconductivity research. The flow of current flow without energy loss may be utilised for the generation of large magnetic fields. These may be utilised in research tools or for magnetic resonance imaging [9], levitating transport [10] or superconducting magnetic energy storage systems [11]. Low current applications include high speed electronics [12] and superconducting quantum interference devices (SQUID's) [13] used for magnetic field detection.

1.3 Aims of this Thesis.

This thesis begins with an overview of general superconductivity, and then more specifically the magnetic properties. It is shown here how useful magnetisation measurements can be for studying the superconducting state of a wide range of materials.

The major work in the thesis is the extensive details of the design and construction of the vibrating sample magnetometer for studying the magnetic response of materials. The complex technicalities of building a stable, accurate and reliable variable temperature environment within a small bore are discussed in detail.

A range of low and high field measurements made with the system on a range of low and high temperature superconductors is discussed in detail. The conclusions of the work so far are given, as are suggestions for further work.

1.4 References.

[1] H.K. Onnes *Akad. van Wetenschappen (Amsterdam)* 14 (1911) 818.

[2] C. Kittel "Introduction to Solid State Physics. 6th ed." *J. Wiley* (1985)

[3] P.J Allen "Small Angle Neutron Scattering from Superconductors" *Ph.D. Thesis, University of Durham, U.K.* (1990)

[4] J.G. Bednorz and K.A. Müller "Possible High T_c Superconductivity in the Ba-La-Cu-O System" *Z.Phys.B.* **64** (1986) 189.

[5] M.K. Wu, J.R. Ashburn, C.J. Torng, P.H. Hor, R.L. Meng, L.Gao, Z.J. Huang, Y.Q. Wang and C.W. Chu "Superconductivity at 93K in a New Mixed-Phase Y-Ba-Cu-O Compound System at Ambient Pressure" *Phys.Rev.Lett.* 58 (1987) 908.

[6] H. Maeda, Y. Tanaka, M. Fukotomi and T. Asano "A new high-T_c oxide superconductor without a rare earth element" *Jap.Jour.Appl.Phys.* 27 (1988) L209.

[7] Z.Z. Sheng and A.M. Hermann "Bulk superconductivity at 120K in the Tl-Ca/Ba-Cu-O system" *Nature* 332 (1988) 138.

[8] A. Schilling, M. Cantoni, J.D. Guo and H.R. Ott "Superconductivity above 130K in the Hg-Ba_Ca-Cu-O system" *Nature* 363 (1993) 56.

[9] A. Oppelt and T. Grandke "Magnetic Resonance Imaging" *Supercond.Sci.Technol.* 6 (1993) 381.

[10] T. Saitoh, N. Maki, T. Kobayashi, M. Schibata and T. Takizawa "Electromagnetic force and eddy current loss in dynamic behaviour of a superconducting magnetically levitating vehicle" *IEEE.Trans.Appl.Supercond.* 3 (1993) 417.

[11] J.M. Pfotenhauer, M.K. Abdelsalem, F. Bodker, D. Huttleston, Z. Jiang, O.D. Lokken, D. Scherbarth, B.Tao and D. Yu "Test results from the SMES proof of principle experiment" *IEEE.Trans.Mag.* 27 (1991) 1704.

[12] K.K. Likharev "Superconducting Devices and Electronics" *Concise Encyclopedia of Magnetic and Superconducting Materials* (1992) ed. J.Evetts, Pergamon Press, Oxford, U.K.

[13] G.B. Donaldson, A. Cochran, L.N.C. Morgan and J.C. Macfarlane "Recent progress in the application of SQUIDs to NDE" *Applied Superconductivity vol.2 p.1295* (1993) ed. H.C. Freyhardt.

2. General Superconductivity.

2.1 Introduction.

In the years since 1911 substantial progress has been made towards understanding the behaviour of materials in the superconducting state. This has been through several major advances. In this chapter these developments in understanding the superconducting state are outlined in a historical context, as each new set of ideas relies on what has gone before.

It is shown in this chapter that a superconductor is distinct from a perfect conductor as defined by Maxwell's equations. The phenomenological theories of the London brothers and of Ginzburg and Landau are covered. These describe the observed effects of superconductivity but do not give any insight into the fundamental mechanism of the superconducting state. From these theories it can be shown that there are two types of superconducting material and the differences between the two are discussed. The theory of Bardeen, Cooper and Schrieffer is highlighted. This describes a mechanism by which superconductivity may occur and provides several predictions of superconducting behaviour that may be tested. Finally a summary is given of the work discussed.

2.2 What defines a Superconductor?

As has been shown in figure 1.1 a superconductor has zero resistance. The lower limit on the decay time of a persistent current in a superconducting loop as determined by precision nuclear magnetic resonance experiments [1] is 100,000 years. However, this zero resistance could simply describe a perfect conductor. In 1933 Meissner and Ochsenfeld discovered that if a superconductor is cooled through its transition temperature, T_c, while in a magnetic field then the flux is excluded [2], as in figure 2.1. A perfect conductor will only oppose *changes* in magnetic field, and so the flux would be trapped.

The concept of a *Critical Temperature, T_c,* above which the superconducting state is destroyed has been introduced in chapter 1 (also seen in figure 1.1). There also exists a *Critical Magnetic Field, B_c,* at which the superconducting state is destroyed. (There are in fact several magnetic fields that are referred to as "critical", these will be discussed in detail in section 2.5). There is a third parameter by which the superconducting state can be characterised, the *Critical Current Density, J_c.* It is defined as that current density which destroys the superconducting state.

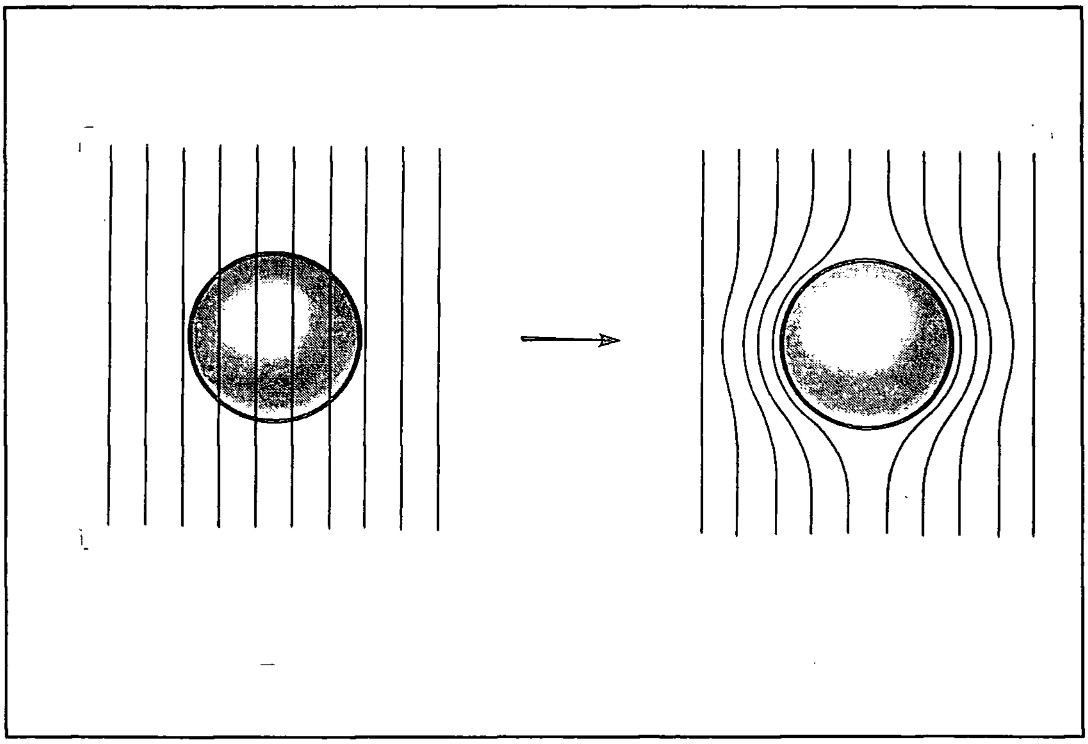

Figure 2.1 Behaviour of a superconductor on cooling through T_c in the presence of a magnetic field [5].

2.3 The London Equations.

In 1935 the London brothers postulated a two fluid model of superconductivity in which only a temperature dependant fraction, n_s, of electrons were in the superconducting state, the rest being in the normal state [3]. They suggested that the superconducting properties of zero resistivity and the Meissner-Ochsenfeld effect could be described by some additions to Maxwell's equations. The first London equation describes perfect conductivity:

$$\frac{\partial \vec{J}}{\partial t} = \frac{\vec{E}}{\mu_0 \lambda_L^2}$$

where λ_L is the *London Penetration Depth*, defined to be:

$$\lambda_L = \sqrt{\frac{m_e}{\mu_0 n_s e^2}}$$

where m_e is the electron mass and e is the electronic charge. The second London equation is:

$$\vec{\nabla} \times \vec{J} = \frac{-\vec{B}}{\mu_0 \lambda_L^2}$$

this describes the Meissner-Ochsenfeld effect by ensuring that any time-independent magnetic field is zero. When this second equation is combined with Maxwell's equation:

$$\vec{\nabla} \times \vec{B} = \mu_0 \vec{J}$$

it gives:

$$\nabla^2 \vec{B} = \frac{B}{\lambda_L^2}$$

which when solved for field parallel to surface gives,

$$B(x) = B_0 e^{\frac{-x}{\lambda_L}} \qquad (B \neq 0)$$

i.e. the field decays exponentially within the sample within the London penetration depth. While this is a satisfactory description of what happens, it does not give any insight into the mechanisms at work. The model is also limited as it does not allow for any variation in n_s when the applied magnetic field or current is changed.

2.4 Ginzburg - Landau Theory.

This generalisation of the London work is in a paper written in 1950 by Ginzburg and Landau [4]. In their paper they introduced the wavefunction, Ψ, such that the number density of the superconducting electrons is given by:

$$n_s = |\Psi|^2$$

Minimising a general expression for the free energy of a second-order phase transition, Ψ must satisfy the *Ginzburg-Landau Equation*,

$$\frac{1}{2m^*}\left(-i\hbar\nabla - e\vec{A} \right)^2\Psi + \beta|\Psi|^2\Psi = -\alpha(T)\Psi$$

where A is the vector potential and α and ß are constants. This is similar to the familiar Schrödinger equation, but has a non-linear term. A detailed explanation of this derivation has been outlined by Kittel [5].

From this equation a characteristic length called the *Ginzburg-Landau Coherence Length,* ξ_{GL}, may be deduced. This is the length over which the energy associated with Ψ does not vary significantly.

$$\xi_{GL}(T) = \frac{\hbar}{[2m^*\alpha(T)]^{1/2}}$$

Near to the transition the coherence length and the penetration depth have the same temperature dependence. Therefore the ratio of the penetration depth λ, and the coherence length ξ, is often used to characterise superconducting materials. This temperature independent ratio is called the *Ginzburg-Landau Parameter,* κ, and its significance will be dealt with in the next section.

$$\kappa = \frac{\lambda}{\xi}$$

2.5 Type I and Type II Superconductors.

The Ginzburg-Landau parameter (see section 2.4) can be used to distinguish between two types of superconductors. These are called *type I* and *type II* superconductors, and are detailed below.

2.5.1 Type I Superconductors.

A superconducting material may be classified as type I if the Ginzburg-Landau parameter fulfils the condition:

$$\kappa < \frac{1}{\sqrt{2}}$$

These materials are usually the superconducting elements such as lead and mercury.

The behaviour of the type I superconducting material may be easily seen in the magnetisation curve. This is shown as the dashed line in figure 2.2. The sample behaves as a perfect diamagnet up to a certain field, B_c, at which the magnetisation drops instantaneously to zero. This field is known as the *thermodynamic critical field* as it is defined as the field at which the magnetic energy is equivalent to the difference in free energy between the superconducting (f_s) and normal (f_n) states, i.e.

$$\frac{B_c^2}{\mu_0} = f_n - f_s$$

Typical values of B_c for type I superconductors such as lead (80mT) and titanium (10mT) are too low for them to be of any technological use for making magnets or power cables.

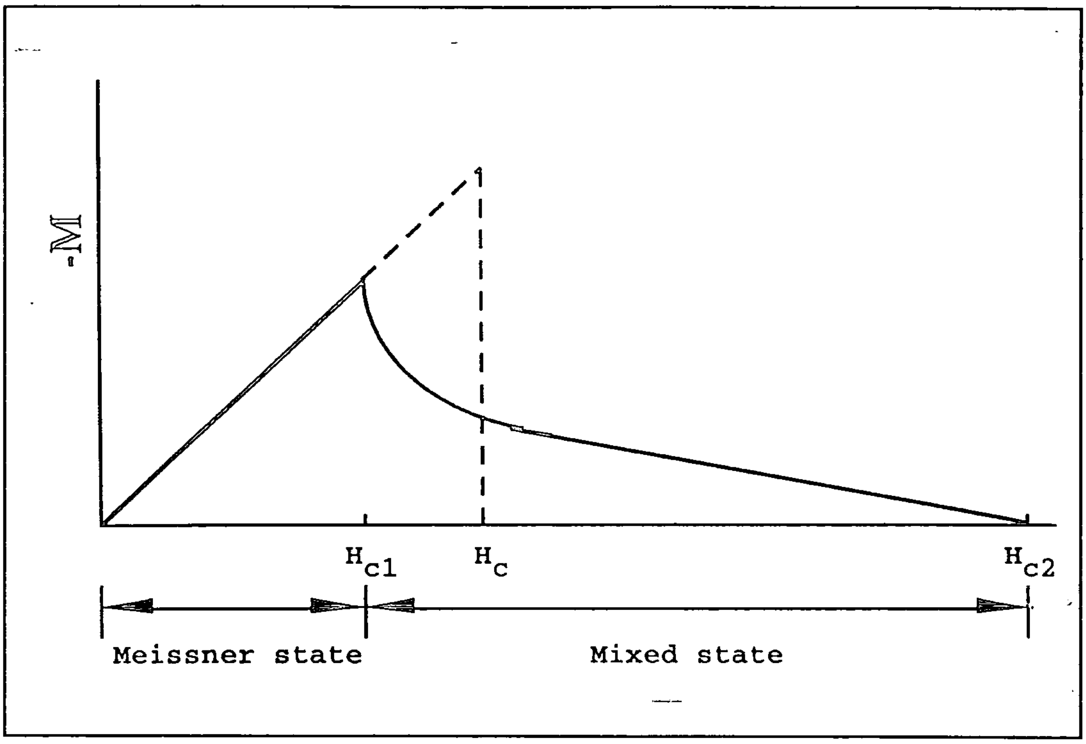

Figure 2.2 Comparative magnetisation curves of a type I (dashed line) and type II (solid line) superconductor [7].

2.5.2 Type II Superconductors.

A superconducting material is considered to be type II when the Ginzburg-Landau parameter satisfies the following condition:

$$\kappa > \frac{1}{\sqrt{2}}$$

These materials are usually alloys.

The magnetisation curve for a type II superconductor (figure 2.2, solid line) can be seen to be very different to that for the type I superconductor. The superconductor exhibits perfect diamagnetism below the *lower critical field*, B_{c1}. This field is less than the thermodynamic critical field. It was proposed by Abrikosov [6] that above the lower critical field the magnetic field is allowed to penetrate the superconductor. This is known as the *mixed state*. This penetration happens until the magnetic field reaches the *upper critical field*, B_{c2}.

The flux enters the superconductor in quanta known as *fluxons*. Each of these contains a quantum of magnetic flux, Φ_0, where:

$$\Phi_0 = \frac{h}{2e} \simeq 2\times10^{-11}\ Wb$$

That flux is quantised in this way was confirmed experimentally in the early 1960's by two separate groups [8, 9]. This idea has however recently been challenged [10]. Each of these fluxons consists of magnetic flux surrounded by circulating superconducting electrons. The core is in the normal state. The distribution of magnetic field around the fluxon and the values of the order parameter are shown in figure 2.3. Note that when the magnetic field is a maximum the order parameter is zero at the centre of the fluxon.

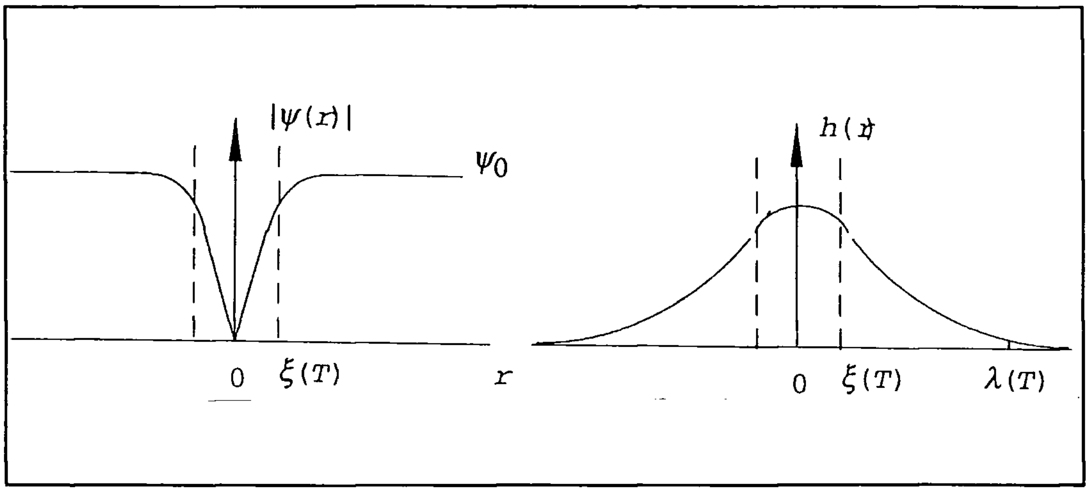

Figure 2.3 Representation of the order parameter Ψ and magnetic field B around a fluxon [7].

Values of upper and lower critical fields may be calculated from Ginzburg-Landau theory in terms of the coherence length and penetration depth in the following way:

$$B_{c1} = \frac{\Phi_0}{\lambda^2}\ln(\kappa) \quad : \quad B_{c2} = \frac{\Phi_0}{2\pi\xi^2}$$

2.6 Bardeen, Cooper and Schrieffer (BCS) Theory.

It was shown in 1956 by Cooper [11] that it is possible for two electrons to attract each other. This idea was extended by Bardeen, Cooper and Schrieffer in 1957 [12] to form their Nobel Prize winning theory (referred to as BCS theory).

In BCS theory the "particle" responsible for superconductivity is the *Cooper pair*. This is a pair of electrons in a bound state with opposite spins. BCS theory provides a physical meaning to *coherence length* as the distance over which the Cooper pairs interact. The attraction of the electrons to form a Cooper pair can be described thus:

(i) An electron passes an ion in the lattice and there is mutual attraction between the two. The positive ion moves from its equilibrium position.

(ii) This locally causes an imbalance in the charge of the lattice.

(iii) Another passing electron is attracted towards the excess positive charge in the lattice.

From this it may be said that the electrons have attracted each other through the exchange of a virtual phonon. This idea is supported by the *isotope effect*, which was observed [13, 14] some years before BCS theory. These studies measured the effect on T_c of the isotopic mass M, and the result was:

$$T_c \propto M^{\alpha}$$

The constant α is equal to 0.5 for many superconductors as predicted by BCS theory.

From this theory it was possible to predict the zero temperature values and temperature dependencies of several superconducting properties, some of these are detailed below.

a) Critical Temperature

The BCS theory predicts that the transition temperature in zero applied magnetic field is:

$$T_c = 1.13\frac{\hbar\omega_D}{k_B}\exp\left(-\frac{1}{N(E_F)V}\right)$$

where ω_D is the Debye frequency, k_B is Boltzmann's constant, $N(E_F)$ is the density of states at the Fermi level and V is an electron-phonon coupling constant. If V is invariant then $\omega_D \propto M^{½}$, which gives the isotope effect.

b) Energy Gap

BCS theory predicts that the Cooper pairs are bound with the following energy at zero temperature:

$$\Delta(0) = 1.76 k_B T_c$$

and this energy gap has the following temperature dependence when $T \rightarrow T_c$:

$$\Delta(0) = 1.74\left(1 - \frac{T}{T_c}\right)^{½}$$

The validity of these predictions of the energy gap and the temperature dependence have been confirmed experimentally by infra-red absorption [15], ultrasound attenuation [16] and tunnelling experiments [17].

c) Thermodynamic Critical Field

Over the full temperature range up to T_c BCS theory predicts that the thermodynamic critical field varies with temperature as:

$$\frac{B_c(T)}{B_c(0)} \approx 1 - \left(\frac{T}{T_c}\right)^2$$

This prediction has been verified experimentally [18] for lead, mercury and aluminium.

d) Low Temperature Specific Heat

This is predicted by BCS to have the following dependence on temperature:

$$\frac{c_s(T)}{\gamma T_c} = 1.34\left(\frac{\Delta(0)}{T}\right)^{\frac{3}{2}} e^{\frac{-\Delta(0)}{T}}$$

γ is from the linear term in the normal state specific heat. This dependence has been confirmed for tin and vanadium [19].

Unfortunately, for the new high temperature superconductors this theory is not so successful. One of the basic effects of the BCS theory, the isotope effect, is absent in $YBa_2Cu_3O_{7-\delta}$ [20]. While substituting O^{18} for O^{16} changes the lattice frequency significantly, T_c remains unchanged. It is also observed that the relation between the energy gap at absolute zero and the critical temperature predicted by BCS theory is not observed in the high T_c superconductors.

2.7 Summary.

In this chapter it has been shown that a superconductor is not simply a material that has zero resistance, as was believed prior to the discovery of flux exclusion (Meissner-Ochsenfeld effect). A phenomenological theory that described these two properties but did not give insight into the causes of them was formulated by the London brothers. This was later extended into a very successful general theory by Ginzburg and Landau. Abrikosov introduced the idea of quantised fluxons to explain the properties of type II superconductors. An explanation of the fundamental mechanism of superconductivity has been provided by Bardeen, Cooper and Schrieffer. This theory successfully predicts many properties of superconducting materials. However the new high-T_c materials are more complicated and do not conform so well to these well established theories.

2.8 References.

[1] J. File and R.G. Mills "Observation of persistent current in a superconducting solenoid" *Phys.Rev.Lett* 10 (1963) 93.

[2] W. Meissner and R. Ochsenfeld *Naturwissenschaften* 21 (1933) 787.

[3] F. London and H. London "The Electromagnetic Equations of the Supraconductor" *Proc.Roy.Soc.* A149 (1935) 71.

[4] V.L. Ginzburg and L.D. Landau *Zh.eksp.teor.Fiz.* 20 (1950) 1064.

[5] C. Kittel "*Introduction to Solid State Physics*" 6th ed. (1986) J.Wiley and Sons.

[6] A.A. Abrikosov "On the magnetic Properties of Superconductors of the Second Group" *Soviet.Phys.JEPT.* 5 (1957) 1174.

[7] D.N. Zheng "An experimental study of flux pinning in high temperature superconductors" *Ph.D. Thesis, University of Cambridge, U.K.* (1994).

[8] R. Doll and M. Näbauer "Experimental proof of magnetic flux quantisation in a superconducting ring" *Phys.Rev.Lett.* 7 (1961) 51.

[9] B.S. Deaver Jr. and W.M. Fairbank "Experimental evidence for quantized flux in superconducting cylinders" *Phys.Rev.Lett.* 7 (1961) 43.

[10] J.R. Kirtley in *High T_c Update* **8** (1994) number 8.

[11] L.N. Cooper "Bound Electron Pairs in a Degenerate Fermi Gas" *Phys.Rev.* **104** (1956) 1189.

[12] J. Bardeen, L.N. Cooper and J.R. Schrieffer "Theory of Superconductivity" *Phys.Rev.* **108** (1957) 1175.

[13] B. Serin, C.A. Reynolds and C. Lohman "The Isotope Effect in Superconductivity. II. Tin and Lead" *Phys.Rev.* **86** (1952) 162.

[14] E. Maxwell "Superconductivity of the Isotopes of Tin" *Phys.Rev.* **86** (1952) 235.

[15] P.L. Richards and M. Tinkham "Far-Infrared Energy Gap Measurements in Bulk Superconducting In, Sn, Hg, V, Pb, and Nb" *Phys.Rev.* **119** (1960) 575.

[16] R.W. Morse and H.V. Bohm "Superconducting Energy Gap from Ultrasonic Attenuation Measurements" *Phys.Rev.* **108** (1957) 1094.

[17] I. Giaever and K. Megerle "Study of Superconductors by Electron Tunnelling" *Phys.Rev.* 122 (1961) 1101.

[18] J.C. Swihart, D.J. Scalapino and Y.Wada "Solution of the gap equation for Pb, Hg and Al" *Phys.Rev.Lett.* 14 (1965) 106.

[19] M.A. Biondi, A.T. Forrester, M.P. Garfunkel and C.B. Satterthwaite "Experimental Evidence for an Energy Gap in Superconductors" *Rev.Mod.Phys.* 30 (1958) 1109.

[20] B. Batlogg, R.J. Cava, A. Jayaraman, R.B. van Dover, G.A. Kourouklis, S. Sunshine, D.W. Murphy, L.W. Rupp, H.S. Chen, A. White, K.T. Short, A.M. Mujsce and E.A. Reitman "Isotope Effect in the High-T_c Superconductors $Ba_2YCu_3O_7$ and $Ba_2EuCu_3O_7$" *Phys.Rev.Lett.* **58** (1987) 2333.

3. Magnetic Properties of Superconductors.

3.1 Introduction.

Abrikosov proposed that magnetic flux enters a type II superconductor in discrete quanta called fluxons [1]. Their existence has been shown by magnetic decoration techniques [2], and Lorentz microscopy [3]. It is important to understand how these fluxons interact with each other and the superconducting material. Another important feature of type-II superconductors is their magnetic hysteresis. These effects must be explained and it is shown how these measurements may be useful in studies of the superconducting state.

Firstly in this chapter the flux line lattice is introduced and its interactions with the material are discussed. It is seen that universal scaling laws are followed for the forces involved in these interactions. The laws have led to the development of models for the interactions and these are briefly discussed. A model that explains the magnetic hysteresis of type II superconductors is explained. This model allows the magnetisation critical current density to be calculated and this is shown too.

3.2 The Flux Line Lattice and its Interactions.

When the fluxons enter the superconducting material they will attempt to organise themselves in such a way as to minimise their energy. The array of fluxons is known as the *Flux Line Lattice*. In a homogeneous superconductor Abrikosov calculated that the fluxons would arrange themselves in a square lattice [1]. Kleiner and co-workers [4] corrected the calculation to arrive at a solution of a triangular lattice. An example of this triangular lattice may be seen in figure 3.1.

This regular array of fluxons can be distorted by the nature of the material. A fluxon consists of a core that is in the normal state (i.e. the Ginzburg-Landau order parameter, $\Psi = 0$) surrounded by two superconducting electrons. If regions within the material exist where the order parameter is lower than in the bulk then it may be energetically favourable for the fluxon to locate there instead of its usual position if it were only interacting with other fluxons. Examples of regions where the order parameter may be reduced are dislocations, crystal defects, twin boundaries and non-superconducting precipitates. The phenomena of such regions fixing the flux line lattice within the material is known as *pinning*.

The strength with which the pinning holds the flux line lattice in equilibrium is known as the *volume pinning force, F_P*, which is defined as:

$$\vec{F}_P = \vec{J}_c \times \vec{B}$$

therefore a higher current can be carried at a higher magnetic field if the volume pinning force is greater. In order to make commercial wires that have high critical current density, defects are often deliberately introduced [5].

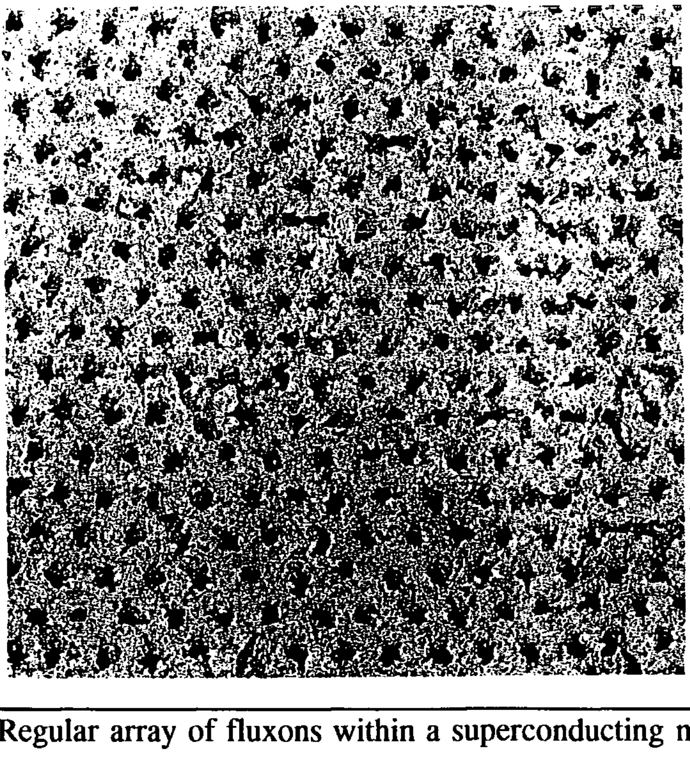

Figure 3.1 Regular array of fluxons within a superconducting material [19].

3.3 Scaling Laws.

Measurements of the volume pinning force of cold-worked wires of niobium alloys [6] by Fietz and Webb lead to the discovery that the volume pinning force could be represented on a universal curve at all temperatures. They found that:

$$F_P \propto [B_{c2}]^{\alpha}.f(b)$$

where b is the reduced field ($b=B/B_{c2}$). The function f(b) and the constants are independent of temperature.

Models have been proposed to define the function f(b). The model postulated by Kramer [7] suggests that at low values of the reduced field, line pins are the dominant source of pinning the flux line lattice. At higher values of reduced field the pinning force is due to shearing of flux lines past each other. This model, while fitting some materials very well is not general enough to account for the huge variety of superconducting materials. The form deduced from this model for the scaling is:

$$F_P \propto B_{c2}^{2.5}.b^{\frac{1}{2}}.(1-b)^2$$

The same problem was addressed in a more general fashion in a paper by Dew-Hughes [8]. In his paper he considered the possible pinning sites and the nature of their interaction with the fluxons. He successfully predicted the form of the scaling law for many materials. By using his model, the dominant pinning mechanism in a material may be deduced from the volume pinning force data.

While this works well for most low-T_c materials, in the new high-T_c compounds uncertainty in the determination of B_{c2} (often greater than 50T) makes the application of scaling laws difficult.

3.4 Irreversible Magnetisation - The Critical State Model.

In 1964 a model to explain hysteretic behaviour in superconductors was proposed by C.P. Bean [9]. This model is known either as *Bean's Model* or the *Critical State Model.* The model is based around four assumptions about the superconductor that is being studied:

(i) The self-field of the sample is much less than the applied magnetic field. This ensures that the critical current is uniform in all of the sample.

(ii) The lower critical field is zero. This condition is fulfilled if the applied field is much greater than the lower critical field. Typically for type II superconductors the ratio $B_{c2}/B_{c1} \approx 1000$.

(iii) There are only three allowable current densities in the sample, 0 and $\pm J_c$, the critical current density.

(iv) The sample is homogeneous, allowing current to flow throughout the sample.

To formulate the model the four above assumptions are combined with one of Maxwell's equations:

$$\vec{\nabla} \times \vec{B} = \mu_0 \vec{J}$$

this equation may be interpreted as the field gradient is proportional to the current density, i.e.

$$\frac{dB}{dx} \propto J$$

Consider a virgin slab of superconducting material of thickness 2a with a magnetic field applied perpendicular to the slab's axis as in figure 3.2. As can be seen current densities of $\pm J_c$ flow to shield out the applied magnetic field to a depth d, where:

$$d = \frac{H}{J_c}$$

The field has penetrated the sample with a uniform flux gradient in accordance with the first assumption.

As the applied field increased the sample is eventually fully penetrated and this is shown in figure 3.3. At this field, current is flowing in the whole sample. The current density may be related to the full penetration field, H*:

$$H^* = aJ_c$$

Using a geometric argument and the relationship;

$$B = \mu_0(H+M)$$

the magnetisation can be expressed in terms of the full penetration field, and hence the current density:

$$M = \frac{H^*}{2} = \frac{aJ_c}{2}$$

this may be re-arranged:

$$J_c = \frac{2M}{a}$$

so the critical current density is shown to be a function of the magnetisation of the sample, a result that will be useful later.

If the applied field is further increased the field and current density profiles are represented in figure 3.4. Here the field gradient across the sample is less, and the values of the current density are lower. Eventually at B_{c2} the applied field is not screened at all.

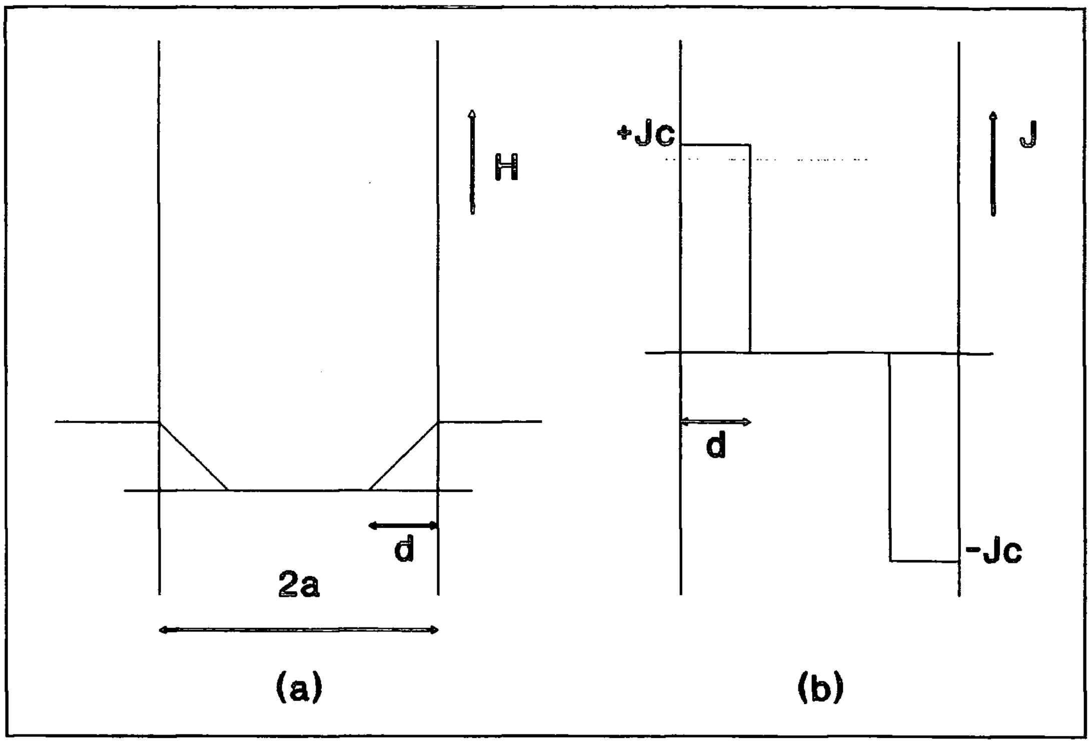

Figure 3.2 (a) Magnetic field and, (b) current density profiles for a slab shaped sample of a type II superconductor in a low applied magnetic field.

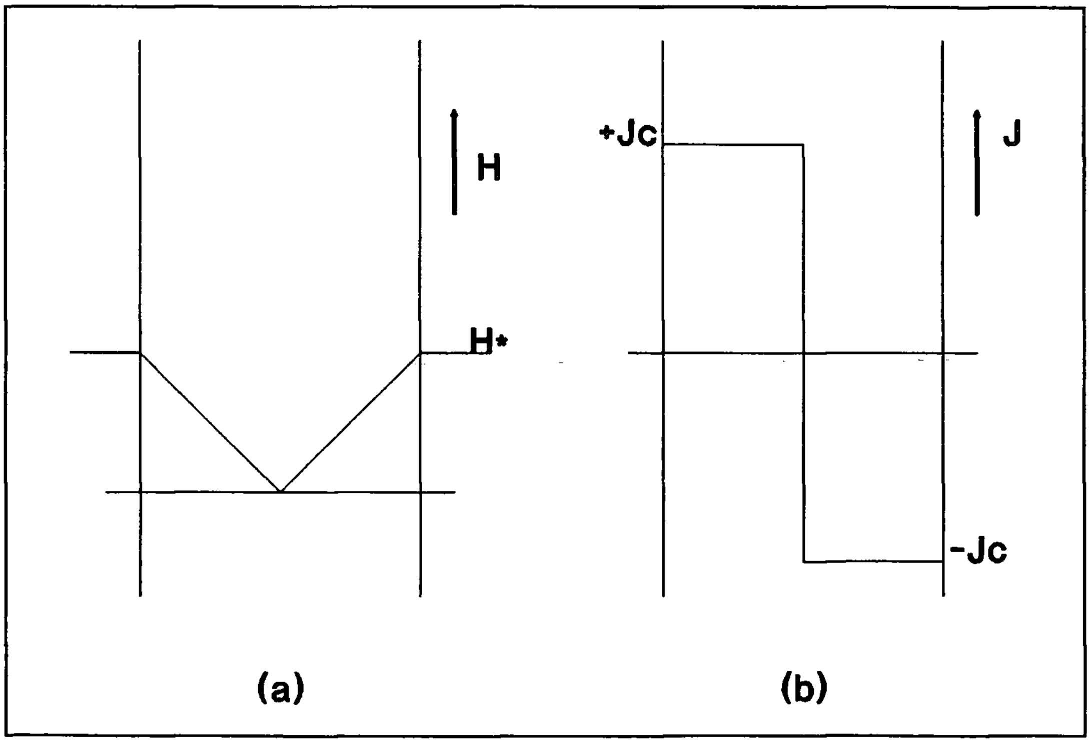

Figure 3.3 Magnetic field, (a), and current density, (b), profiles for a slab shaped sample of type II superconductor at the full penetration field, H^*.

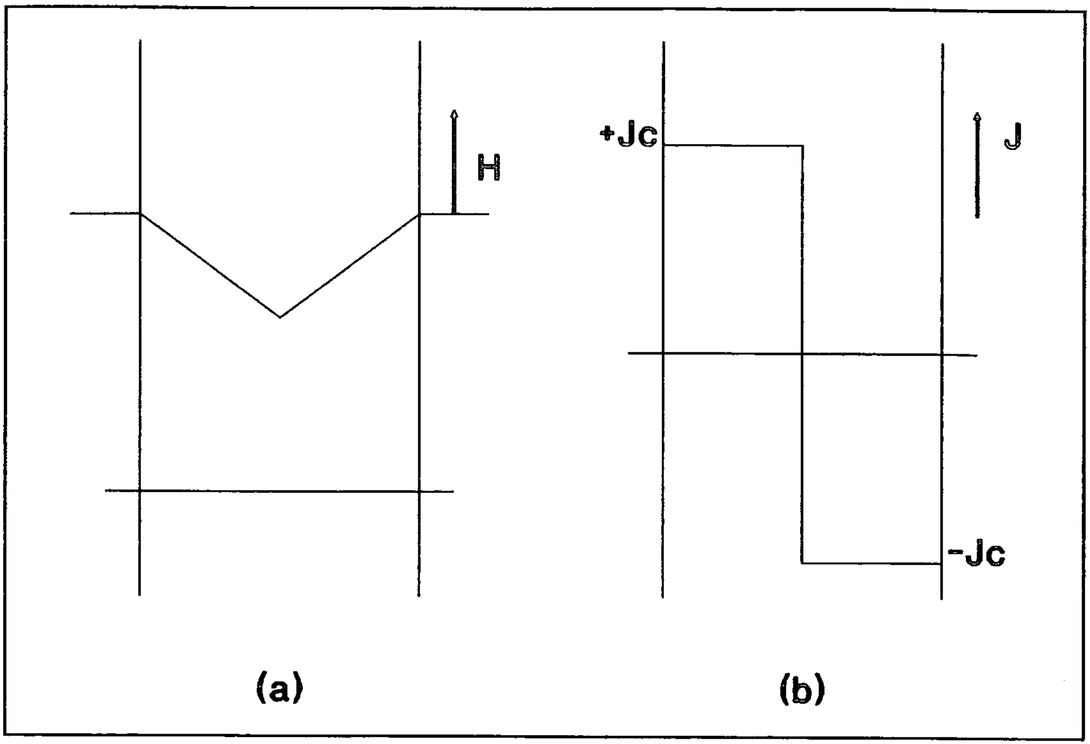

Figure 3.4 (a) Magnetic field and, (b) current density distributions in a slab shaped sample of type II superconductor at applied magnetic field $H^{*} < H < H_{c2}$.

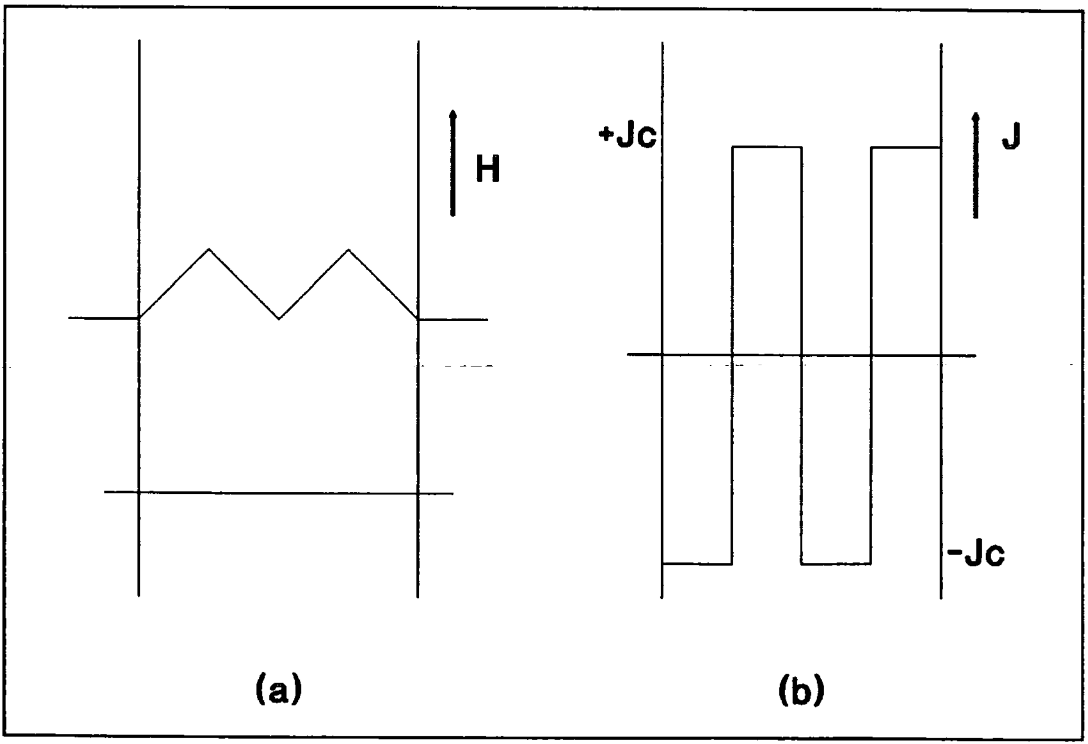

Figure 3.5 (a) Magnetic Field and, (b) current density distributions throughout a slab shaped sample of type-II superconductor after the applied magnetic field has been slightly reduced.

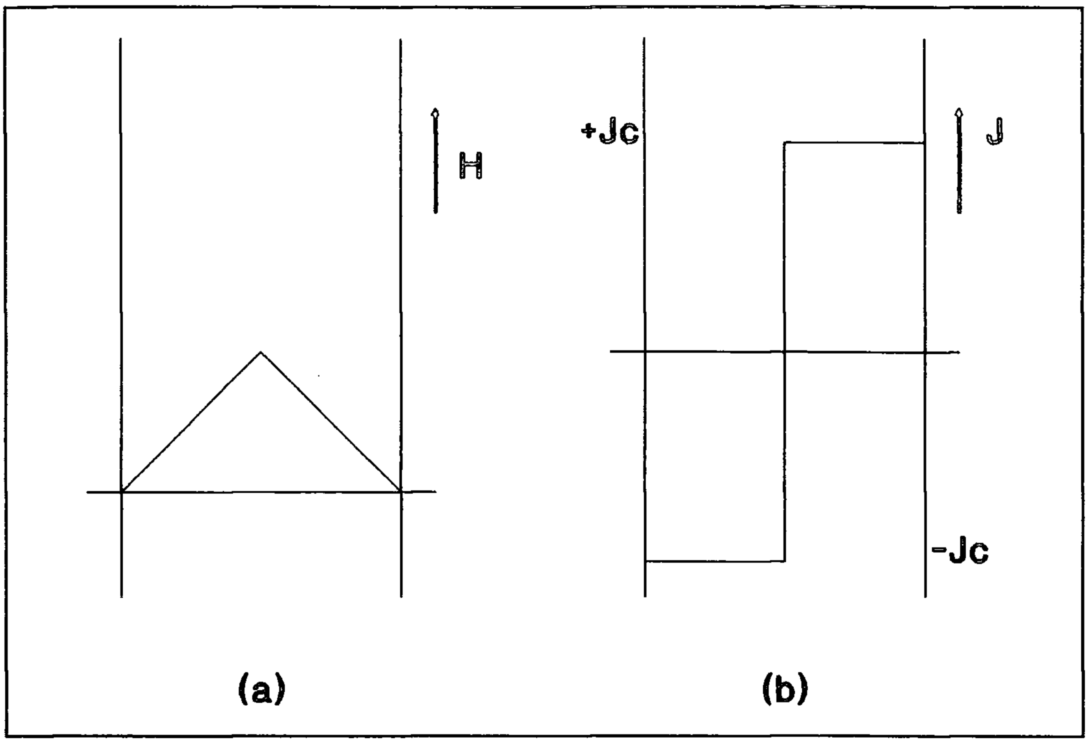

Figure 3.6 (a) Magnetic field and, (b) current density distributions in a slab shaped type-ii superconductor when the applied magnetic field has been reduced to zero.

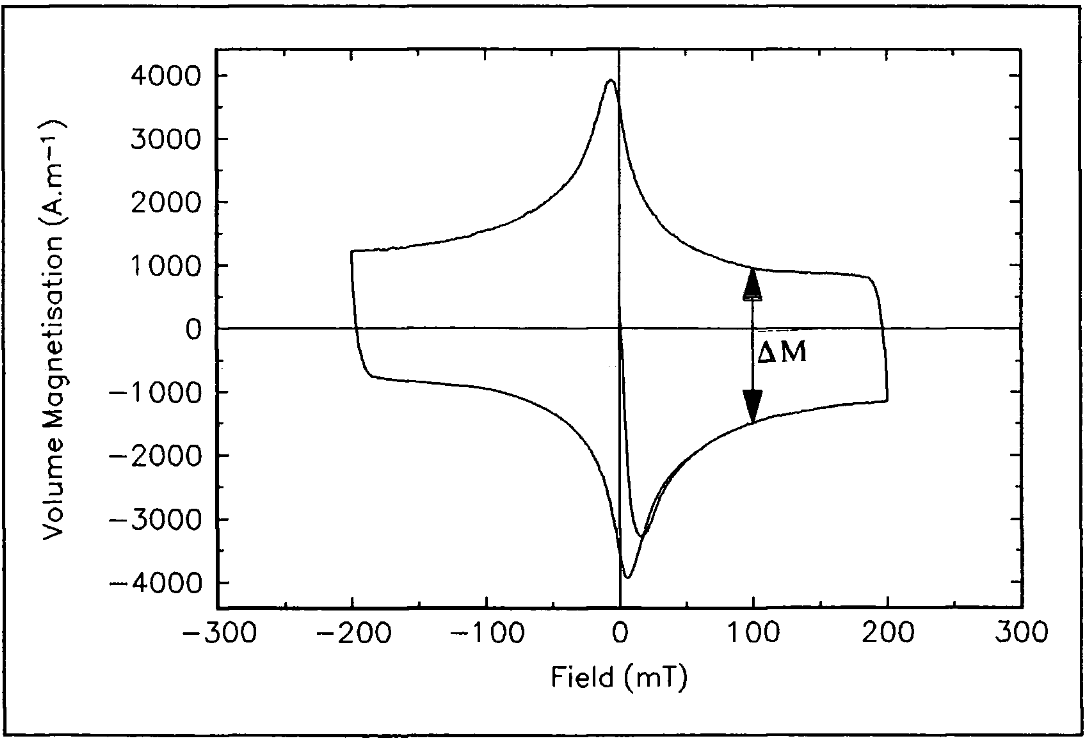

Figure 3.7 Magnetisation loop for a single crystal of $YBa_2Cu_3O_{7-\delta}$ at 77K. ΔM is shown by the double-headed arrow.

Figure 3.5 represents the situation if the applied field is reversed by a small amount from an applied field less than the upper critical field. At the surface of the sample the current density, while being the same magnitude, reverses direction. This is in response to the changing magnetic field. The inner section of the sample is not affected by the change. In figure 3.6 the applied field has been reduced to zero. As can be seen there is still flux in the sample and current flowing throughout. This is hysteretic behaviour.

There are two slight adjustments that need to be made to this model. Firstly the current density in the sample does not change instantaneously, but decays over the London penetration depth, λ_L. This is not usually a problem, unless the sample is approximately the same thickness as the penetration depth as is the case in ultrafine ($d < 1\mu m$) filaments of niobium-titanium [13].

The second correction is if the sample is not homogeneous. Campbell [14] used an A.C. technique to measure directly the flux profile within a type-II superconductor. This work showed that Bean's prediction that the current density and hence field gradient, are constant is correct within the bulk of the sample. However enhanced screening was observed in some superconductors in a thin layer at the surface. This is not a surprising result if it is recalled that stronger pinning leads to higher J_c and at the surface the number density of defects and hence potential pinning sites may be higher.

3.4.1 Calculation of Magnetisation Critical Current Density.

The model can be used to calculate, J_{cM}, the magnetisation critical current density. Recall that:

$$J_c = \frac{2M}{a}$$

Defining M as:

$$M = \frac{\Delta M}{2}$$

because this will eliminate any magnetic signal such as that from the paramagnetic moment of the dysprosium in $DyBa_2Cu_3O_{7-\delta}$. This means only the magnetisation caused by the macroscopic currents in the sample is being considered. Figure 3.7 shows how ΔM at a fixed value of the applied field is taken from a hysteresis curve. Using this the general equation may be formulated:

$$J_{cM} = \frac{\Delta M}{a}$$

Where:		
	J_{cM}	is the magnetisation critical current density,
	ΔM	is the width of the hysteresis loop, and
	a	is a characteristic scaling length.

The characteristic scaling lengths are dependent upon the sample geometry. These are calculated by approximating the sample to be either an ellipsoid [10, 11] or a disk [12].

This method of calculating a critical current density is very useful as it is contactless which is ideal for working on small samples such as single crystals. It also does not require the use of any D.C. transport currents.

This model of hysteresis effects in superconductors agrees well with observed behaviour in low-T_c materials, except where the dimensions are small [13]. Granular effects in the high-T_c superconductors are important as they violate the homogeneity assumptions. For example Zhukov [15] measured J_{cM} and J_{cT} (the transport critical current density) for a $Bi_2Sr_2Ca_2Cu_3O_x$ tape and reported excellent agreement between the two at 10K, but not at 70K.

3.4.2 Effects of Magnetic Field Sweep Rate.

Due to flux creep, a phenomena by which the magnetisation of a superconductor decays with time, magnetic hysteresis measurements are made on superconductors with a constantly sweeping field to allow for this effect. If one of Maxwell's equations is considered:

$$\vec{\nabla} \times \vec{E} = -\frac{\partial \vec{B}}{\partial t}$$

which may be interpreted at the surface of the sample as [16]:

$$E_p = \frac{a}{2} \cdot \frac{dB}{dt}$$

where a is the sample radius. This says that the sweep rate of the applied field may be related to a specific voltage criteria as measured in transport measurements. This information may be used to construct a "V-I" trace [17] or an E-J-B surface [16]. The voltages that can be explored are between 10^{-5} and 10^{-11} $V.m^{-1}$ compared to a typical 10^{-3} $V.m^{-1}$ for transport measurements of critical current density.

3.4.3 Granularity Measurements.

Magnetisation measurements can be used to probe granularity effects in superconductors [18]. If one assumes the Critical State Model to be correct it is easily seen that the observed magnetic moment of a material must scale with its size. If it does not then the material is not homogeneous.

3.6 Summary.

In this chapter it has been seen how magnetic flux enters a type II superconductor and the ways in which it interacts with the material. The critical state model, which explains hysteresis in superconductors has been explained in some detail. This model allows calculations to be made of magnetisation critical current density, and investigations of the effect of electric field on the current density. Granular effects may also be studied using the analysis provided by the model.

3.7 References.

[1] A.A. Abrikosov "On the magnetic properties of superconductors of the second group" *Soviet.Phys.JEPT.* 5 (1957) 1174.

[2] I.V. Grigorieva "Magnetic flux decoration of type-II superconductors" *Supercond.Sci.Technol.* 7 (1994) 161.

[3] J.E. Bonevich, K. Harada, T. Matsuda and A. Tonomura "Observation of Vortices in Superconductors" *MRS.Bull.* **June 1994** 47.

[4] W.H. Kleiner, L.M. Roth and S.H. Autler "Bulk Solution of Ginzburg-Landau Equations for Type II Superconductors: Upper Critical Field Region" *Phys.Rev.* **133** (1964) A1226.

[5] M.N. Wilson "Superconducting Magnets" *Clarendon Press, Oxford, U.K.* (1983).

[6] W.A. Fietz and W.W. Webb "Hysteresis in Superconducting Alloys - Temperature and Field Dependence of Dislocation Pinning in Niobium Alloys" *Phys.Rev.* **178** (1969) 657.

[7] E.J. Kramer "Scaling laws for flux pinning in hard superconductors" *J.Appl.Phys.* **44** (1973) 1360.

[8] D. Dew-Hughes "Flux pinning mechanisms in type II superconductors" *Philos.Mag.* **30** (1974) 293.

[9] C.P. Bean "Magnetization of High-Field Superconductors" *Rev.Mod.Phys.* **36** (1964) 31.

[10] J.A. Osborn "Demagnetizing Factors of the General Ellipsoid" *Phys.Rev.* **67** (1945) 351.

[11] E.C. Stoner "The Demagnetizing Factors for Ellipsoids" *Philos.Mag.* **36** (1945) 803.

[12] D.J. Frankel "Critical-state model for the determination of critical currents in disk-shaped superconductors" *J.Appl.Phys.* **50** (1979) 5402.

[13] F. Sumiyoshi, M. Matsuyama, M. Noda, T. Matsushita, K.Funaki, M. Iwakuma and K. Yamafuji "Anomalous Magnetic Behaviour due to Reversible Fluxoid Motion in Superconducting Multifilamentary Wires with Very Fine Filaments" *Jap.Jour.Appl.Phys.* **25** (1986) L148.

[14] A.M. Campbell "The response of pinned flux vortices to low-frequency fields" *J.Phys.C.* **2** (1969) 1492.

[15] A.A. Zhukov, W. Jahn, B. Runtsch, H. Küpfer, Y. Yamada and R Flükiger "Transport currents and magnetic properties of textured Bi(2223) tape" *Supercond.Sci.Technol.* **5** (1992) 262.

[16] A.D. Caplin, L.F. Cohen, G.K. Perkins and A.A. Zhukov "The electric field within high-temperature superconductors: mapping the E-J-B surface" *Supercond.Sci.Technol.* **7** (1994) 412.

[17] M. Oussena, S. Porter, A.V. Volkozub, P.A.J. de Groot, P.C. Lanchester, D. Ogbourne, M.T. Weller, G. Balakrishnan and D.McK. Paul "Comparative study of pinning and creep in $Tl_2Ba_2CaCu_2O_8$ and $Bi_2Sr_2CaCu_2O_8$ single crystals" *Phys.Rev.B.* **48** (1993) 10575.

[18] L. Le Lay, T.C. Willis and D.C. Larbalestier "Fully connected bulk $Pb_{1-x}Sn_xMo_6S_{7.6}$ samples made by hot isostatic pressing" *Appl.Phys.Lett.* **60** (1992) 775.

[19] C. Kittel "Introduction to Solid State Physics. 6th ed." *J.Wiley* (1985)

4. The Durham Superconductivity Group Vibrating Sample Magnetometer

4.1 Introduction.

The Vibrating Sample Magnetometer (VSM) is a commonly used instrument for the study of magnetic moments in many materials as a function of applied magnetic field and/or temperature. Its use in studies of superconducting materials arises from the ability to perform a contactless determination of the critical current density, by measuring the magnetic moment, and hence magnetisation of the sample. This is possible through the explanation of the critical state model (chapter 3). Most VSM's at present are restricted to applied fields of only 13T. A system to work up to 17T with temperature range of 2K to 150K is attempted. The system designed here has been used to measure single crystals of the high temperature superconductor $YBa_2Cu_3O_{7-\delta}$ at low fields (chapter 6) and for a limited range of high field measurements (chapter 7) on both low and high temperature superconductors.

In this chapter the theory of the operation of a vibrating sample magnetometer is discussed, followed by details of the constituent components of the system. The detailed design of the probe which has been constructed in Durham for these measurements is described. The technicalities of the temperature measurement and control are extensive and, therefore, are contained in chapter 5. The construction and commissioning of a low field superconducting magnet is presented. Some issues of the system design are investigated. There have been major problems with the high field magnet system, in the context of VSM measurements. Investigations of these and their solutions are presented. The system has been accurately calibrated against a nickel standard. Finally a brief summary is given of the performance that has been achieved.

4.2 Principle of the Vibrating Sample Magnetometer

The VSM was first described in detail by Foner [1] in 1959 and many variants to this basic design have been made since (for example [2, 3, 4]). All VSM's work by vibrating a sample between some suitably arranged detection coils. If a single detection coil is considered, the voltage induced (V) in the detection coil due to a local change in net flux follows from Faraday's law:

$$\oint E.ds = -\frac{\partial \phi}{\partial t}$$

i.e.

$$V = -\frac{d\phi}{dt} = -\frac{d\phi}{dx}.\frac{dx}{dt} \tag{1}$$

Using the analysis of Zieba and Foner [5] to equate the flux (ϕ) produced by the magnetic dipole moment (m) of the sample to that produced by a current (I) in the detection coils (i.e. the Biot-Savart law):

$$\vec{B}.\vec{m} = I\phi \tag{2}$$

and assuming that the sample is undergoing simple harmonic motion with amplitude A and frequency ω:

$$\frac{dx}{dt} = A.\omega.\cos(\omega.t) \tag{3}$$

combining (1), (2) and (3) gives:

$$V = G.m.A.\omega.\cos(\omega.t)$$

where G is a geometrical factor. Therefore if the amplitude and frequency of the vibration are known, along with the geometric constant, the voltage induced in the detection coils is proportional to the magnetic moment and hence the magnetisation of the sample.

The detection coil geometry is extremely important. There are two aspects to be considered, signal (S) and noise, these have been detailed by Foner [6]. Consider a detection coil with turns (N), radius (r) at temperature (T) then;

$$S \propto \frac{N}{r^3}$$

so for high signal a detection coil should have many turns and a small radius. Considering noise;

$$\mathit{Field\ Noise} \propto N.r^2$$

$$\mathit{Johnson\ Noise} \propto \sqrt{RT}$$

for a low noise detection coil a small radius and low temperature are desirable.

The conclusion that may be drawn from this analysis is that VSM detection coils should:
- -have as many turns as possible,
- -have as small radius as practical,
- -be cooled to as low temperature as possible.

In an analysis by Springford et.al. [3] the voltage induced in detection coils with the sample vibrating along the detection coil axis is calculated. The relationship between the voltage induced in a detection coil (E) to the position of the centre of vibration along the axis (Z) and the radius of the detection coil (r) is;

$$E \propto \frac{r^2.Z}{(Z^2+r^2)^{2.5}}$$

this is shown for a single detection coil in figure 4.1. Note that a sample vibrating about the centre of the detection coil will generate no voltage.

In a practical VSM, the signal due to the magnetic moment of the sample is generated in two detection coils which are wound in opposite senses symmetrically about the sample. If the voltage in one detection coil is equal to V_A then the voltage

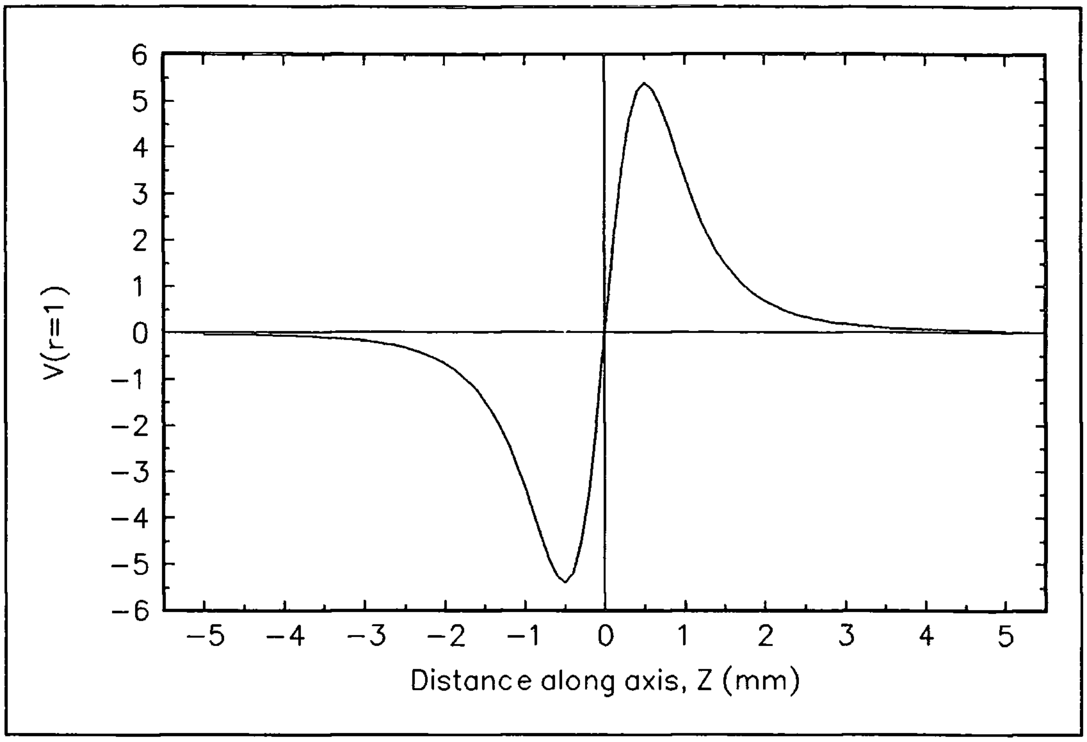

Figure 4.1 Voltage induced in one coil as a function of the position of the centre of vibration along the coil axis.

in the other, $V_B=-V_A$. With the signal being read by a lock-in amplifier operating in (A-B) mode the signal read is $V_A-(-V_A)=2V_A$. This arrangement also has the advantage of suppressing any noise due to the applied field as any induced voltages will be equal in magnitude but have opposite sense.

The Springford analysis may be used to design the optimum spacing along the vibration axis of two detection coils connected in the opposite sense. Ideally the total induced voltage should be independent of Z over the greatest possible range. This reduces the maximum magnitude of the signal, but allows for accurate measurements to be made on large samples. The optimum centre-centre separation along the axis is:

$$2Z = \sqrt{3}r$$

4.3 Operation of the Durham VSM system.

The VSM described here is an axial type, where the vibration is parallel to the applied field. The description is split into four sections, measurement of magnetic moment, the magnetic fields, computer control and data acquisition, and thermometry. Figure 4.2 shows the components of the VSM built within the Superconductivity Group in Durham.

4.3.1 Measurement of Magnetic Moment.

This section covers the part of the VSM that is necessary to measure magnetic moment of the sample as a function of applied magnetic field, at fixed temperature. The oscillatory motion for the sample is provided by an EG&G PARC model 4500 **Head Driver**. This has a dedicated **Head Controller**, that uses feedback from the head driver to keep the vibration at a constant 85Hz with amplitude of approximately 100μm through the drive. This unit also provides a TTL reference voltage for an EG&G 5210 **Lock-in Amplifier**, which uses the reference for phase sensitive detection of the 85Hz component from the signal produced in the **detection coils**. This signal is due to the magnetic moment of the **sample** that is mounted on the **sample rod**.

As seen in section 4.2 the signal generated by the detection coils is proportional to the amplitude of the vibration. Therefore the amplitude of the vibration drive voltage is measured by **DVM1**.

To ensure that the detection coils are correctly centred in the magnet an A.C. method is used. The detection coils are placed axially in the centre of the magnet to which an A.C. field is applied. The objective is to find a position where the (A-B) voltage is a minimum. Balancing of better than 0.5% of the voltage from one detection coil alone can be obtained.

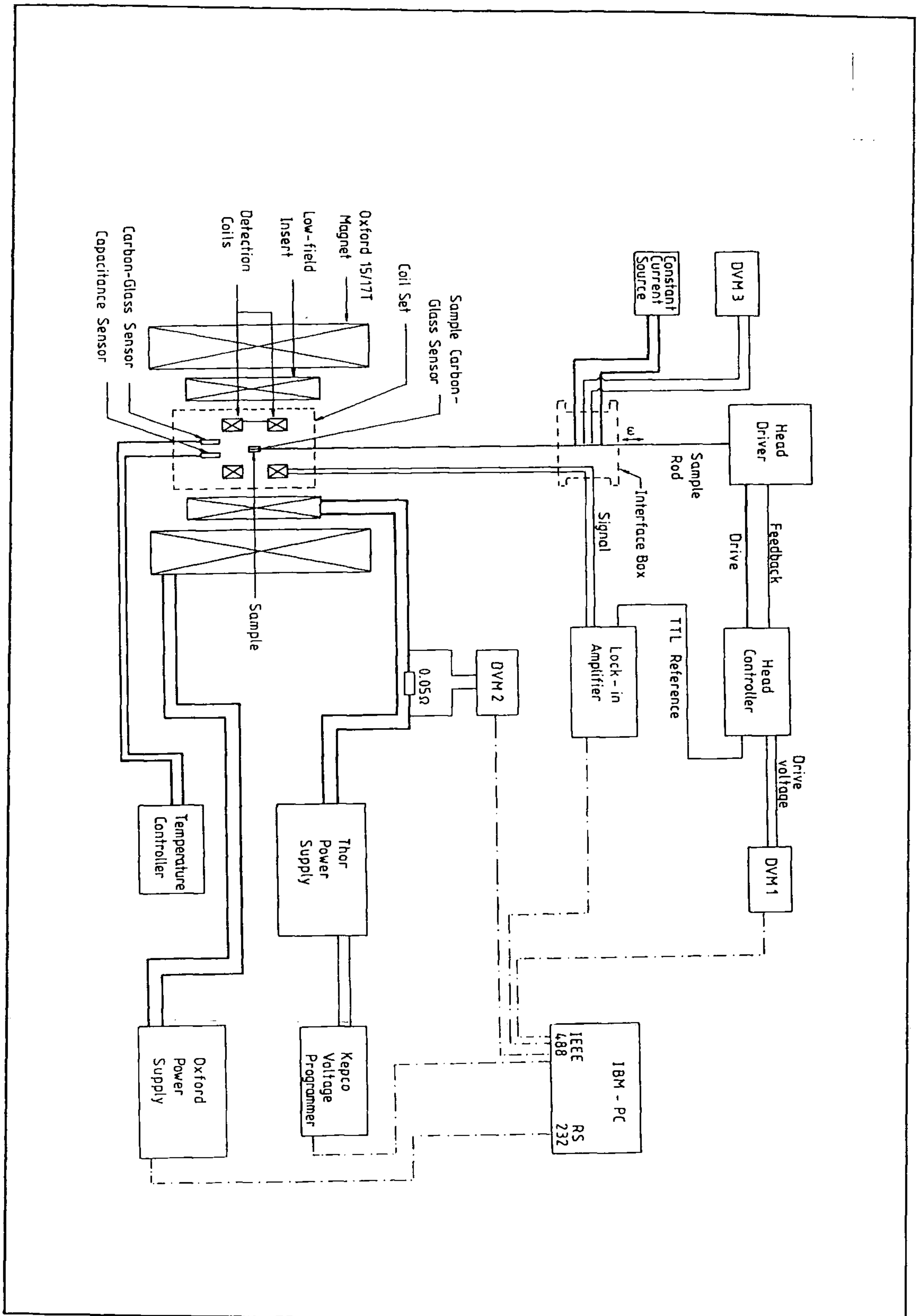

Figure 4.2 Circuit diagram of the Durham Superconductivity Group Vibrating Sample Magnetometer.

4.3.2 Magnetic Fields.

The magnetic field system is provided by two magnets. The **Oxford 15/17T Magnet** is a NbTi/Nb_3Sn superconducting magnet, which has a 40mm bore and is powered by the dedicated **Oxford Power Supply** (120A, 10V). The NbTi **Low Field Insert** sits inside the bore of the Oxford 15/17T magnet and provides fields up to 2T in a 20mm bore. The low field insert is powered by the **Thor Power Supply** (100A, 5V), programmed by a voltage from the **Kepco Voltage Programmer**. Current in the low field insert is monitored by **DVM2** reading the voltage across a 0.05Ω standard resistor.

When the system is used as a low field VSM in liquid nitrogen the Oxford power supply is used to provide current to a copper magnet which replaces the low field insert, and there is no Thor power supply, Kepco voltage programmer or DVM2.

4.3.3 Computer Control and Data Acquisition.

The output and control of all the instruments is through the IEEE-488 interface to an **IBM PC** (model 35 SX), except for the Oxford Power Supply which uses the RS-232C data bus.

The whole system is controlled by dedicated code written in ASYST. The aims of the program are to:-

a) Control the fields in the magnets and prevent damage by providing safe escape routes in case of emergencies.

b) Read the output of the experiment in the format (field, voltage) at given intervals.

c) Provide real time data plotting that allows the user to check the quality of the data whilst the experiment is in progress.

d) Save the data in a format suitable for manipulation in standard analysis packages.

A flow diagram of the basic data acquisition loop is shown in figure 4.3. In an initial stage the user has to input information about the destination file for the data, along with details of the required maximum fields and sweep rates. The program prevents the user exceeding the recommended sweep rates for the Oxford 15/17T magnet. From these a frequency of data acquisition is calculated, such that there are approximately 1500 points over a full loop. There is a facility in the program for the user to abort the run. If this happens the data acquired is saved and the field reduced to zero at the maximum recommended rate to prevent damage to the Oxford 15/17T magnet.

As was shown in chapter 3 it is necessary for the magnetic field to have a well defined sweep rate. While this is straightforward when using the Oxford Power Supply (by one simple command) it is complicated with the Thor Power Supply as not only does each step need to be individually programmed, but the time taken to read DVM2 (or any device in fact) is not constant. To overcome these problems the program was made to consider how long it should have taken to do the total of steps executed, compared to how long it has actually taken. It then introduces an appropriate delay to make the overall time correct. Over a one minute period with approximately 800 steps it was found to be accurate to better than 0.1%.

Once the experiment has been started the field value is monitored to see if the maximum field has been reached, and if it is appropriate to take a data point. On taking a data point the computer records the field and the signal as measured by the lock-in amplifier, normalised to the amplitude of the vibration. This information is plotted on the computer screen. When the loop has been completed the data is saved as a Lotus 1-2-3 compatible file.

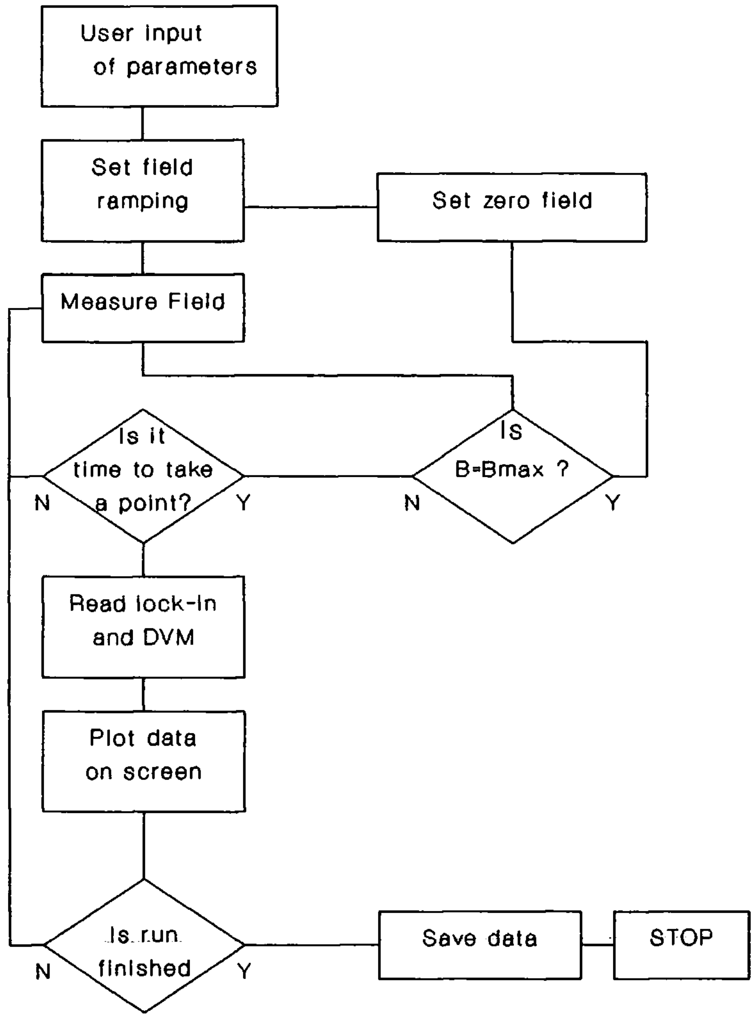

Figure 4.3 Computer Control of Vibrating Sample Magnetometer.

4.3.4 Thermometry.

There are two thermometers in the probe, a carbon-glass sensor and a ceramic capacitance sensor for control purposes, and these are shown in figure 4.5. They are read by a Lakeshore Temperature Controller. There is also a sample carbon-glass sensor (figure 4.2) on the sample rod close to the sample. This is read by DVM3 and the constant current source.

The technicalities of the thermometry are complicated and have been the subject of much work. Therefore a detailed discussion is carried out in chapter 5.

4.4 VSM Probe Design.

This section details the VSM probe designed and built in Durham. It is divided into three sections, general features of the probe design, details of the detection coil design and sample mounting.

4.4.1 General Design Features.

The probe provides support and protection for the detection coils and thermometry. An overview of the probe and head driver is given in figure 4.4. The head driver provides the oscillatory motion to the sample that is free to move within the probe and is mounted on a free standing frame, to decouple it mechanically from the magnet system.

The **bellows** are used to allow the vertical position of the sample to be easily adjusted whilst leaving the probe in fixed position. It is believed that the bellows' resilience helps to damp stray vibrations from the head driver.

Electrical connections for the detection coils and thermometry are through vacuum tight leadthroughs which have been hard soldered into the brass **interface box**. Firmly secured PTFE coated wires running down the inner support tube connect the interface box to the coils and thermometry.

The **outer vacuum jacket** of thin walled stainless steel provides protection for the delicate instrumentation and allows control over the gas pressure within the probe through a **pumping valve** in the interface box, which will also release any build up of pressure within the probe.

In order to reduce electrical noise the coil set is prevented from moving in the magnetic field. Above the coil set are several **copper disks** on resilient mountings ensuring that the **stainless steel support tube** is held centrally in the outer vacuum jacket. Below the detection coils is a stabilising spike on the coil set that mates in to a centrally located recess in the outer vacuum jacket. A firm fit is ensured by using vacuum grease which will solidify under cryogenic conditions.

The detection coils are wound on the coil set shown in figure 4.5. It is made from tufnol which is an insulating, non-magnetic composite material. The carbon-glass sensor and capacitance sensor are held in a protective tufnol thermometry plug in the base of the coil set. The coil set is mounted on the stainless steel inner support tube with G.E. varnish.

4.4.2 Design of the Detection Coils.

The physical constraints of the system limit the scope for design. In order to have detection coils with the maximum number of turns, and the optimum separation of Springford (see section 4.2), each detection coil has the following dimensions:

Inner Radius = 12.92mm
Outer Radius = 15.00mm
Length = 11.02mm

and the initial detection coil centre-centre separation was set to be 12.1mm.

To check the validity of Springford's model the response of the detection coils was measured, by moving a small piece of vibrating permanent magnet material through the detection coils, and measuring the signal generated. The results of an experimental response profile for the 12.1mm centre-centre separation are presented in figure 4.6. As can be clearly seen the induced voltage is strongly dependent on Z over the whole range.

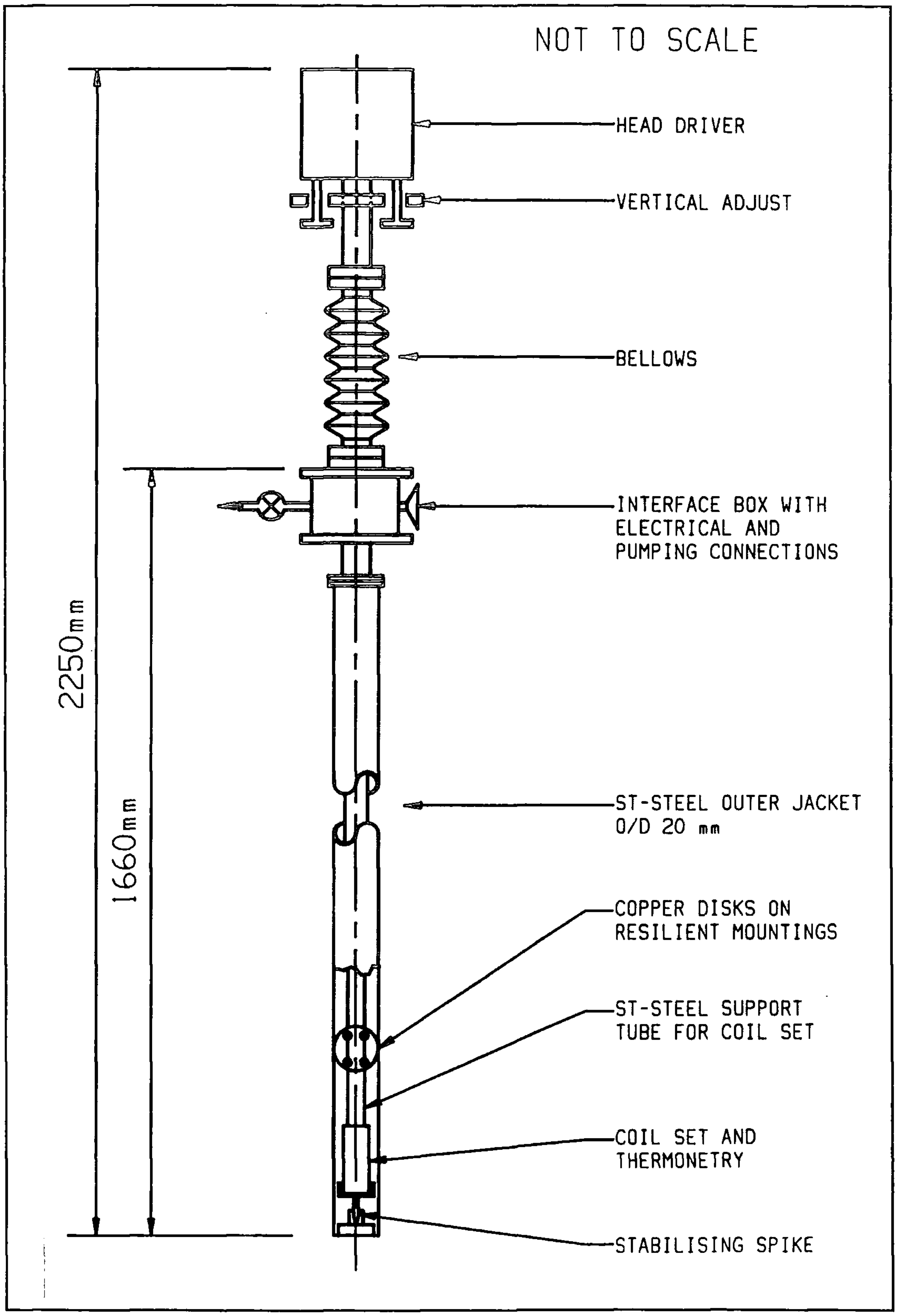

Figure 4.4 Overall view of the Vibrating Sample Magnetometer Probe.

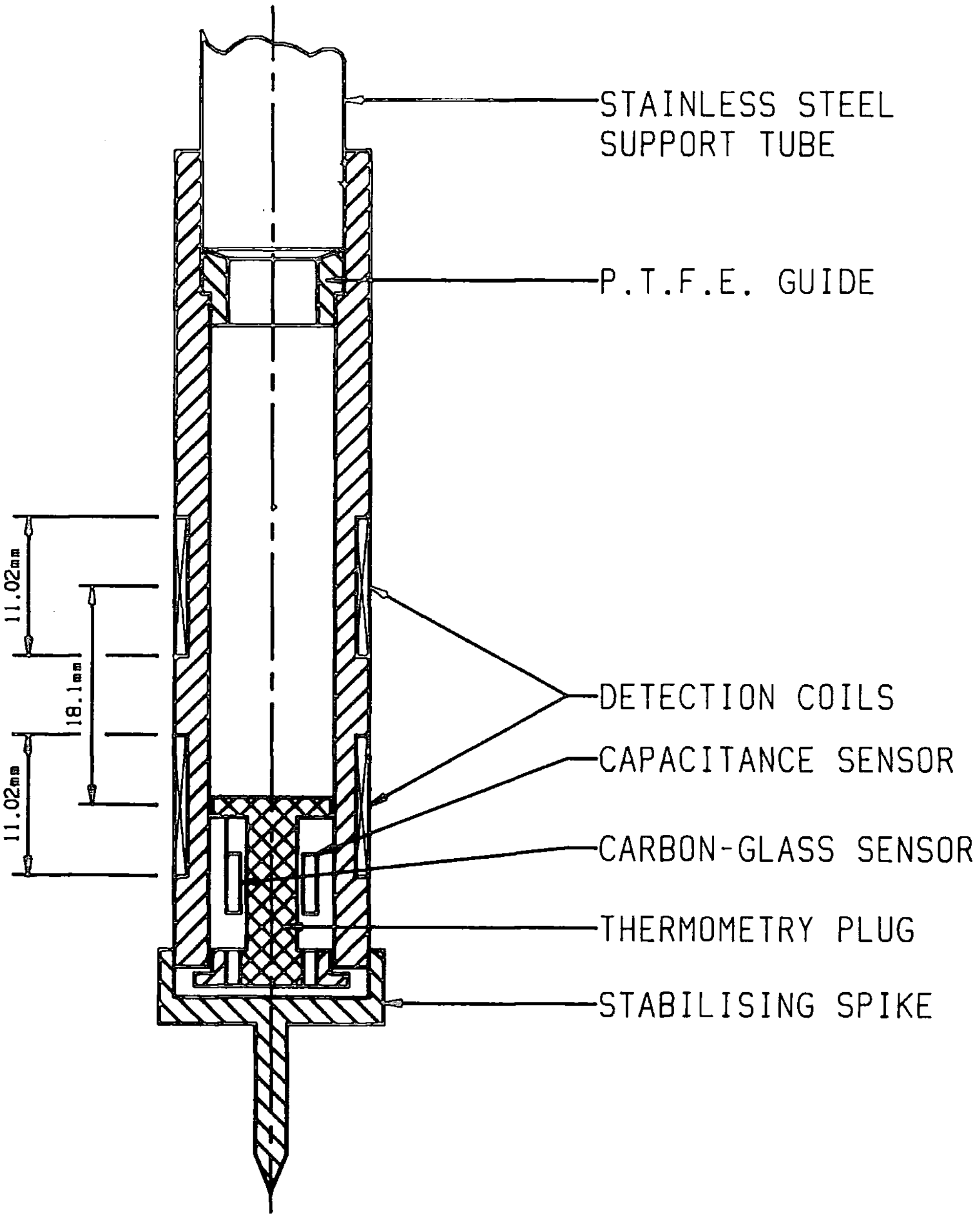

NOT TO SCALE

Figure 4.5 Detailed View of the coil set of the Vibrating Sample Magnetometer probe. Positions of the two thermometers and the stabilising spike are also shown.

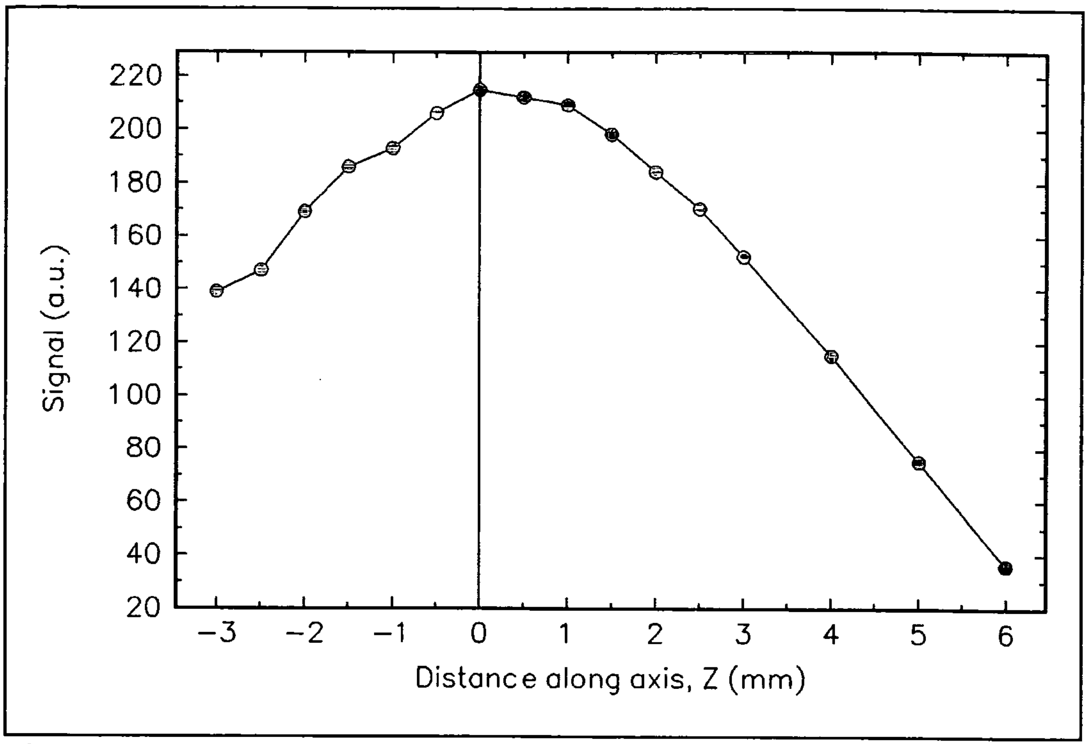

Figure 4.6 Experimental coil pick-up profile for the 12.1mm centre-centre separation.

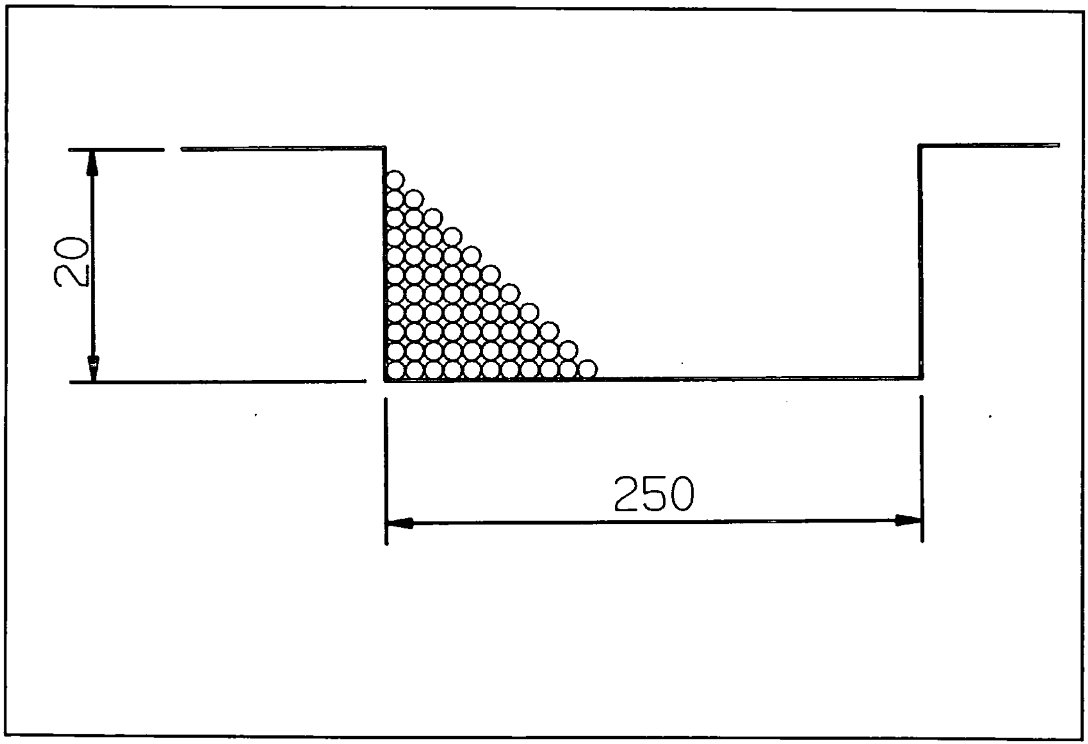

Figure 4.7 Basis of the model used to calculate the induced voltage in the coils.

In order to understand this some computer modelling work was carried out. The model generalised Springford's work on a single coil to each turn of the detection coil. The detection coils here each consist of 5000 turns of 48SWG (0.041mmø) copper wire, in 20 layers, each having an average of 250 turns as in figure 4.7. The computer model of the detection coil simply summed the contribution from each turn to the total induced voltage of the detection coil. Two of these were then added in opposition to simulate detection coil behaviour in a practical VSM.

Figure 4.8 shows the results of this simulation for a 12.1mm centre-centre detection coil separation compared to the data taken. There is reasonable agreement between the data and the calculation consistent with the model.

The simulation process was repeated for various values of the centre-centre detection coil separation. For values below 12.1mm the induced voltage showed a stronger dependence on Z. An optimum was found when the centre-centre detection coil separation was 18.1mm. This gave a region 4mm long where induced voltage was independent of Z. The calculation and subsequent experimental verification are presented in figure 4.9. When the centre-centre separation was further increased it resulted in a dip in the centre of the profile.

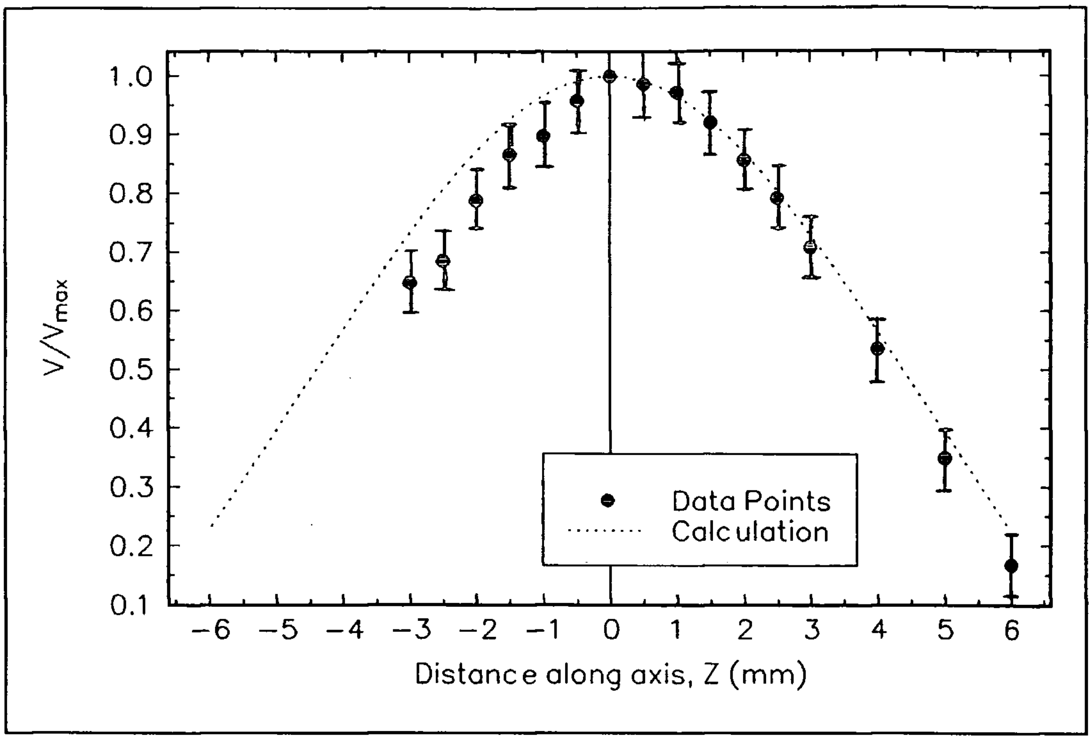

Figure 4.8 Comparison of Experimental and Calculated induced voltages for the 12.1mm centre-centre separation.

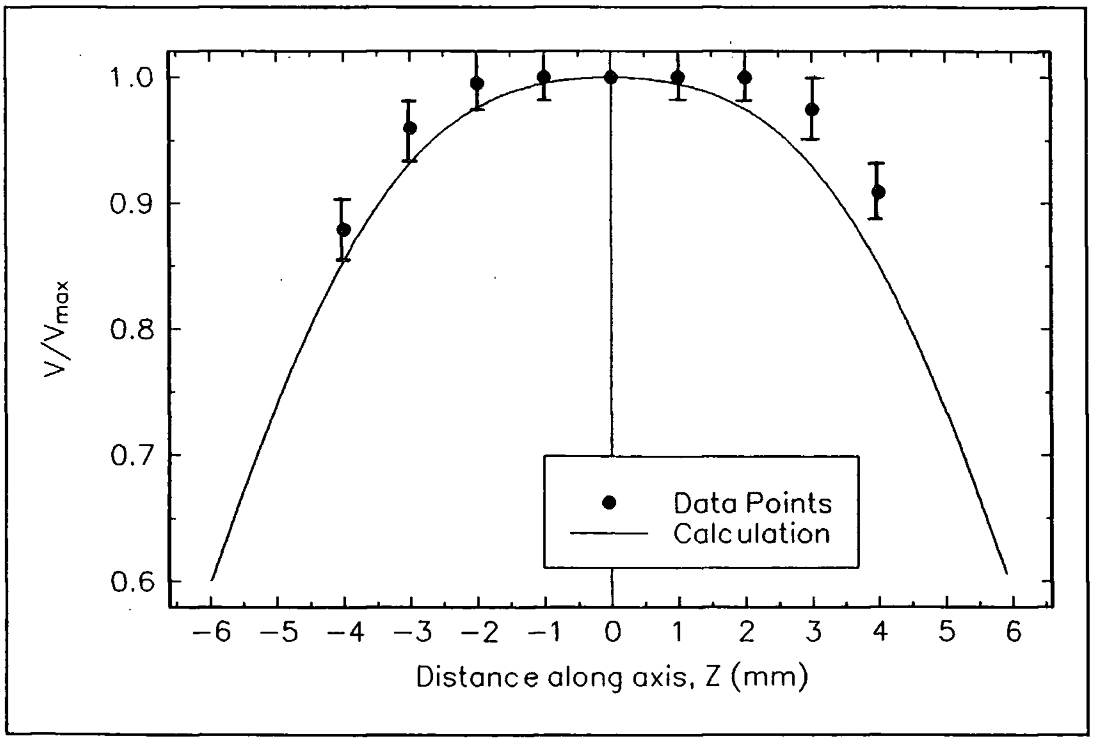

Figure 4.9 Calculated and Experimental induced voltages for the 18.1mm centre-centre separation.

4.4.3 Sample Mounting.

In order to vibrate in synchronisation with the head driver the sample has to be mounted on a holder attached to a rod that couples to the oscillations of the head driver. Coupling is provided by a purpose made brass rod provided by EG&G with the head driver. Extensions to this have been made from brass tube as it is lightweight, fairly strong and non-magnetic. Glass was not used as in other VSM's [4], due to its brittle nature. Tufnol rod was also considered, but it is too flexible. Carbon-Fibre is a possibility [7] that has not been explored and could be used in the future.

The sample holder is made from a short piece of tufnol and is represented in figure 4.10. This has a flat area machined at one end to allow the sample to be mounted.

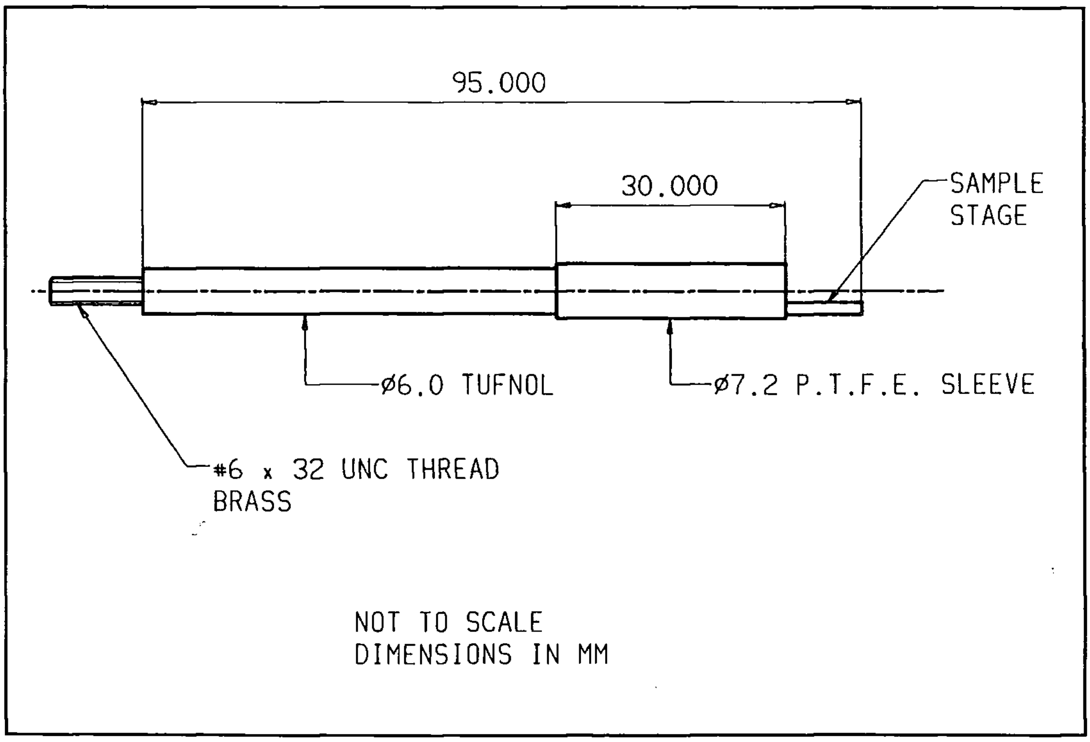

Figure 4.10 Tufnol/PTFE Sample Holder.

The PTFE sleeve is to ensure that the vibration is in a vertical manner by interacting with the PTFE guide (see figure 4.5). The thin sleeve was chosen from several designs due to:

a) No positioning problems- as the sleeve is 30mm long it will always sit within the guide, unlike short rings.

b) Ease of manufacture- thin walled PTFE is difficult to machine, and reliable thin wall sizes would be difficult to obtain.

c) Vibrational Heating- caused by the sleeve rubbing the coil set. This dictates that the sleeve be thin. A 9.8mm sleeve was observed to cause a 3K temperature rise from a base temperature of 4.2K (measured by a RhFe temperature sensor mounted as if it were a sample). The current 7.6mm sleeve causes a 200mK rise from 4.2K. Removing the PTFE does not eradicate the problem. At higher temperatures the effect is far less severe due to the rapidly rising specific heat capacities.

In order to mount securely the samples on the sample holder there is a choice of glues:

a) G.E. Varnish- is very strong, but can take up to a few hours to dry. It is also quite difficult to wash off, even with acetone, and therefore may damage delicate samples (e.g. high temperature superconducting ceramics).

b) Polystyrene Cement- (the type used with plastic model kits) is not as strong as G.E. varnish, but does dry faster (~ half hour). It dissolves readily in acetone and may be used with delicate samples.

4.5 Design and Construction of the Low-Field Insert.

It was decided to construct a separate low field insert coil to fit in the 40mm bore of the 17T magnet. This was wound on a tufnol former from ultra-fine NbTi wire, which allows the field to be increased beyond the 1.8T/min limit of the Oxford 15/17T magnet. The turns of this insert are packed with Apiezon N grease to protect against quenching. The dimensions of the windings are:

Inner diameter = 23mm
Outer diameter = 38mm
Length = 87mm.

The insert was calibrated using a Hall Probe and the result is presented in figure 4.11, data having been taken up to just below the quench point of the magnet.

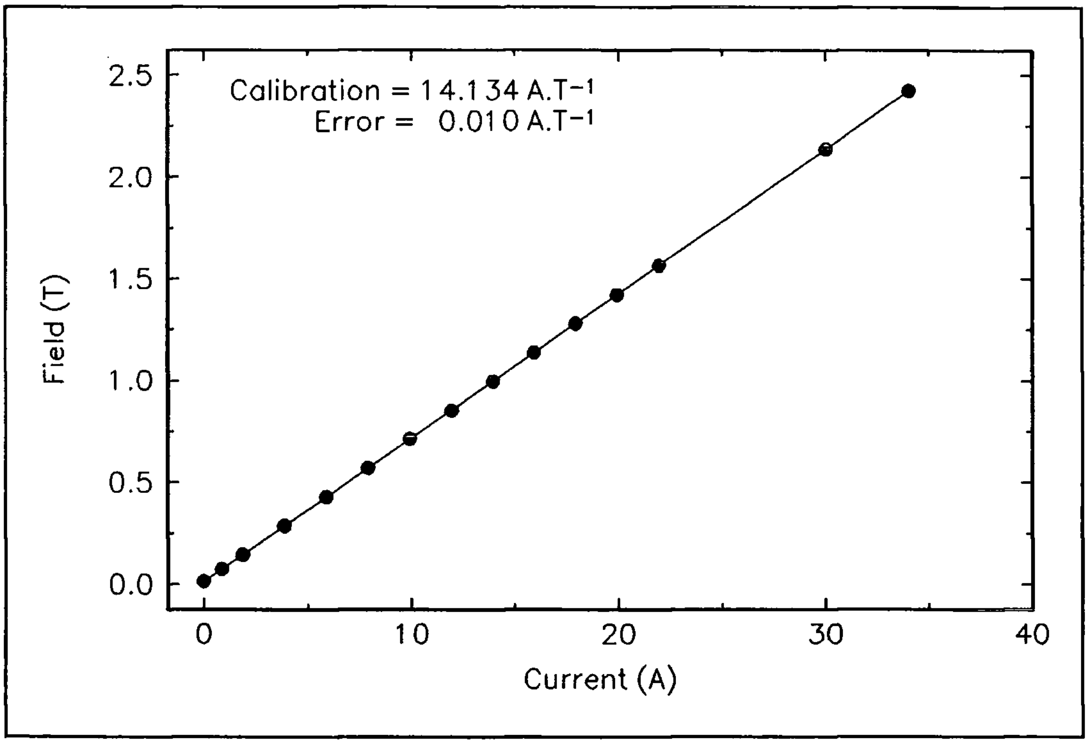

Figure 4.11 Field/Current relationship of the low field superconducting insert.

4.6 Flux Jumping in the Nb_3Sn Section of the Oxford 15/17T Magnet.

When the VSM was first used in the Oxford 15/17T magnet extreme noise below 1.6T was observed. An example of this can be seen in figure 4.12. This noise makes all data below 1.6T useless, and so it had to be eliminated. In order to discover the cause of the noise the various components in the system were replaced in a systematic way. The first targets for investigation were the solder joints in the probe, the thin wire of the detection coils and the thermometers. All these causes were eliminated. External components such as the Oxford power supply and the lock-in amplifier were also eliminated. After noticing that voltage kicks on the analogue display of the Oxford power supply happened momentarily before large noise spikes, the Oxford 15/17T magnet was found to be the cause.

Upon consultation with the manufacturer[1] it was discovered that the inner sections of the Oxford 15/17T magnet were made from a particular type of Nb_3Sn known as "Jelly Roll". In this type of material the superconducting filaments are not continuous in the wire (as in NbTi) but are in the form of many short overlapping strands. This is done as a method of making Nb_3Sn of high critical current density at minimal cost. Unfortunately this material is unstable at low fields and is prone to flux jumping[2].

To overcome this it was decided to take data for a sample in two loops;

a) Low Field Data- take this in the first loop which is $0T \rightarrow 2T \rightarrow 0T$.

b) High Field Data- second loop of $0T \rightarrow B_{max.} \rightarrow 0T$ taken immediately afterwards with the low field section ignored.

---

[1] Oxford Instruments Limited, Eynsham, Witney, Oxon. OX8 1TL. U.K.

[2] For a detailed discussion of flux jumping see Appendix A.

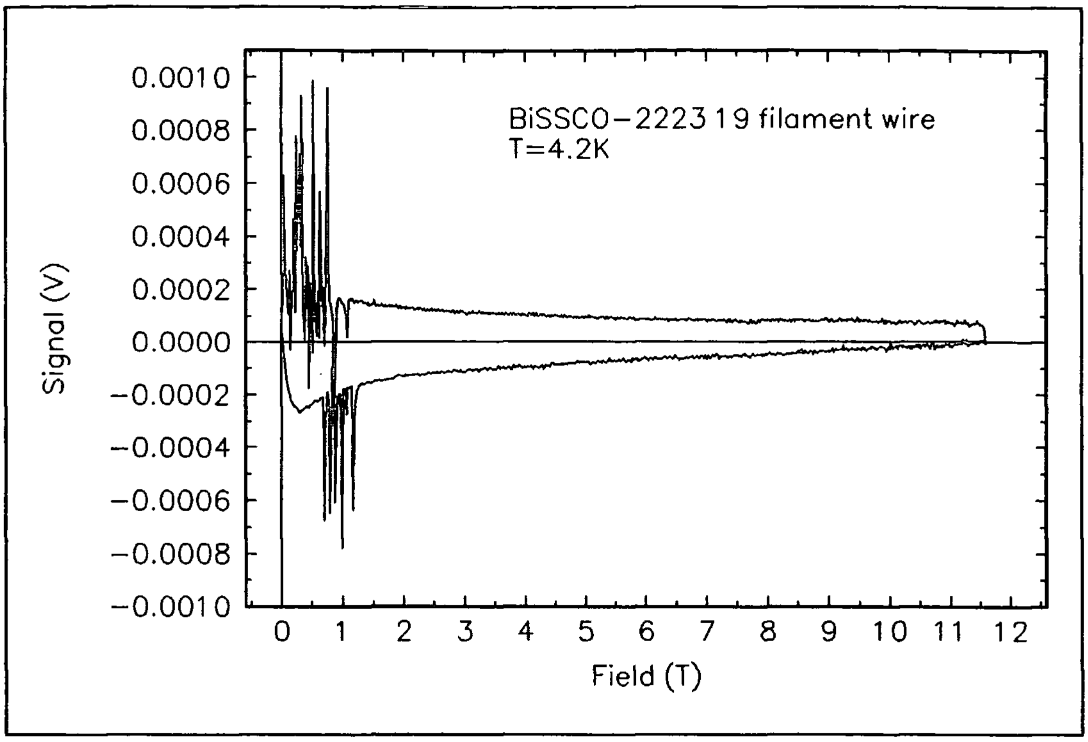

Figure 4.12 Effects of flux jumping in high field magnet sections on a typical sample.

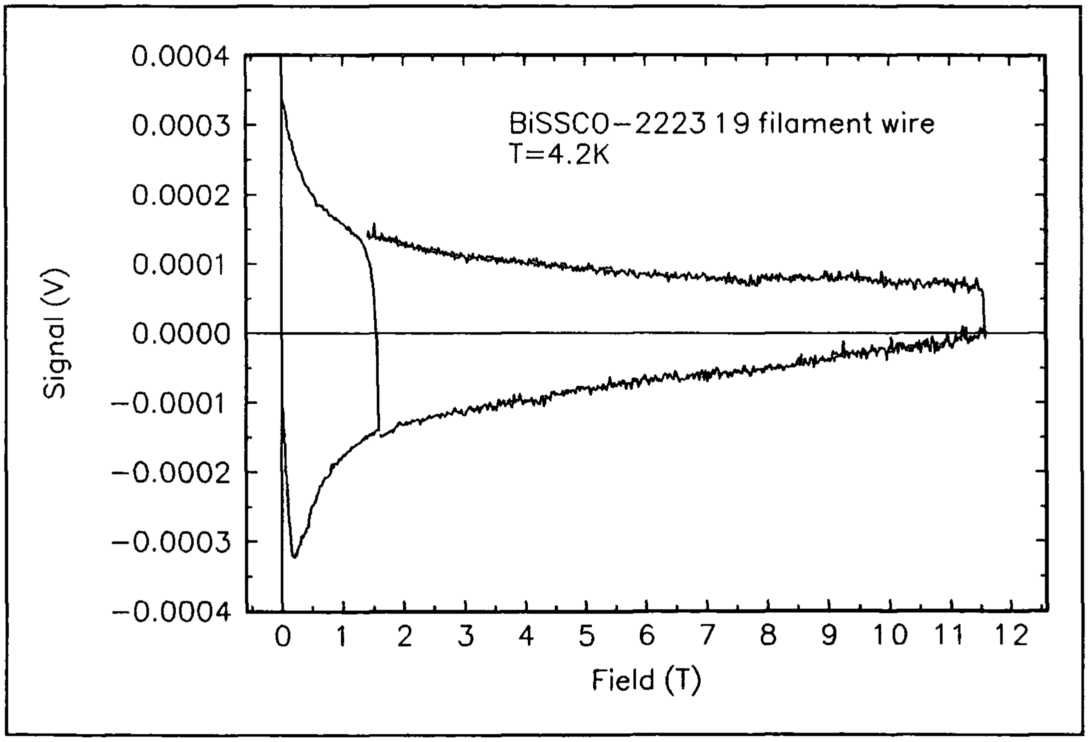

Figure 4.13 Hysteresis trace when effects of flux jumping in the high field system are removed. Compare to previous figure to see improvement.

In the first instance it was proposed to use the stable NbTi section of the Oxford 15/17T magnet for the low field data, and both sections of the Oxford 15/17T magnet to run the high field data. This could easily be achieved by taking an extra current lead from the join between the sections of the magnet and employing a separate power supply for the low field loop (in this case the Thor power supply). This did not work as it was impossible to ensure that current did not flow through short circuits provided by the power supplies and sections of the magnet. Therefore the separate low field insert was used to provide the low field loop.

The improvement in data quality using the low field insert is demonstrated by comparing figure 4.12 and figure 4.13. Note how the major and minor loops are consistent in figure 4.13, showing the quality of the data.

4.7 Calibration of the System.

The output from the VSM is in volts. However, the aim is to measure the magnetic moment of the sample. By measuring the magnetic moment of a well known sample then a calibration between volts and A.m^2 can be calculated. To do this the saturation magnetisation of nickel [9] was measured in high fields at 4.2K for several samples of different masses. A typical trace is shown in figure 4.14, the saturation voltage being that on the flat section of the trace.

Several of these give a plot of saturation magnetic moment against the saturation voltage. This plot is shown in figure 4.15. As can be seen it is a straight line and gives the result:

$$\textit{Calibration Constant} = 0.240 \pm 0.001\ A.m^2.V^{-1}$$

The sensitivity of the system is determined not only by the calibration constant, but also by the noise levels. In the high field magnet system the noise level is 20μV, giving a sensitivity of approximately 5×10^{-6}A.m^2 for fields above 2T. Below 2T this noise is reduced by a factor of five, and so the sensitivity is 10^{-6}A.m^2. When the low field, liquid nitrogen system is used the noise level is reduced to 1μV, giving a sensitivity of 2.5×10^{-7}A.m^2.

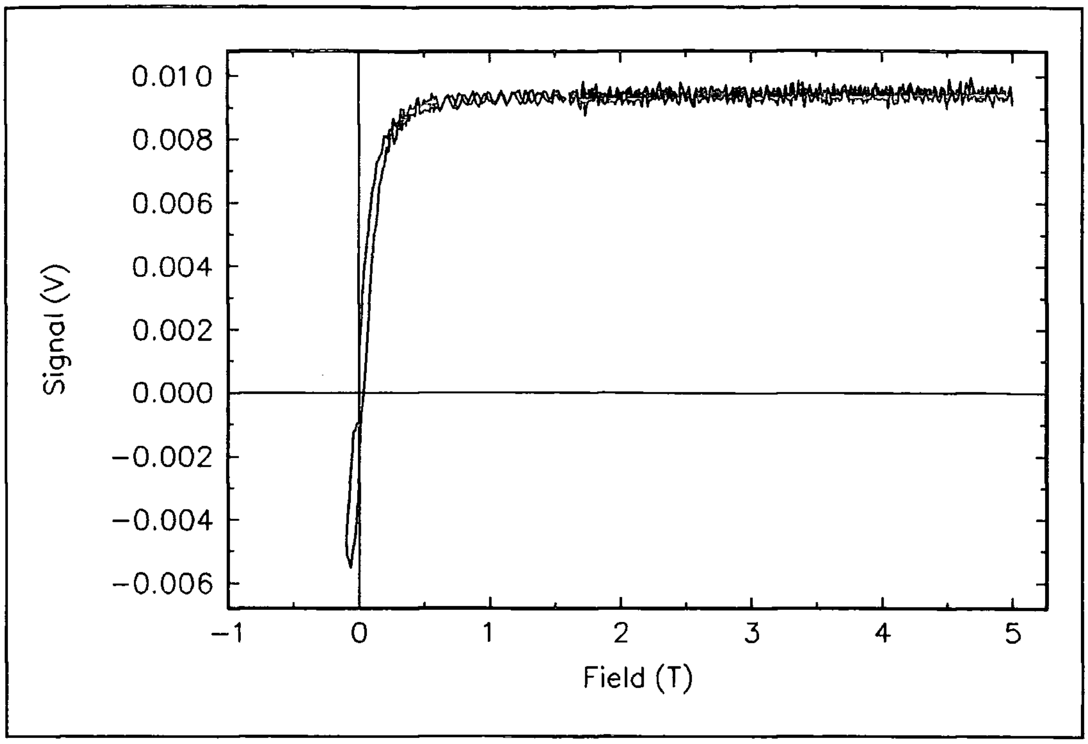

Figure 4.14 Typical hysteresis loop for nickel.

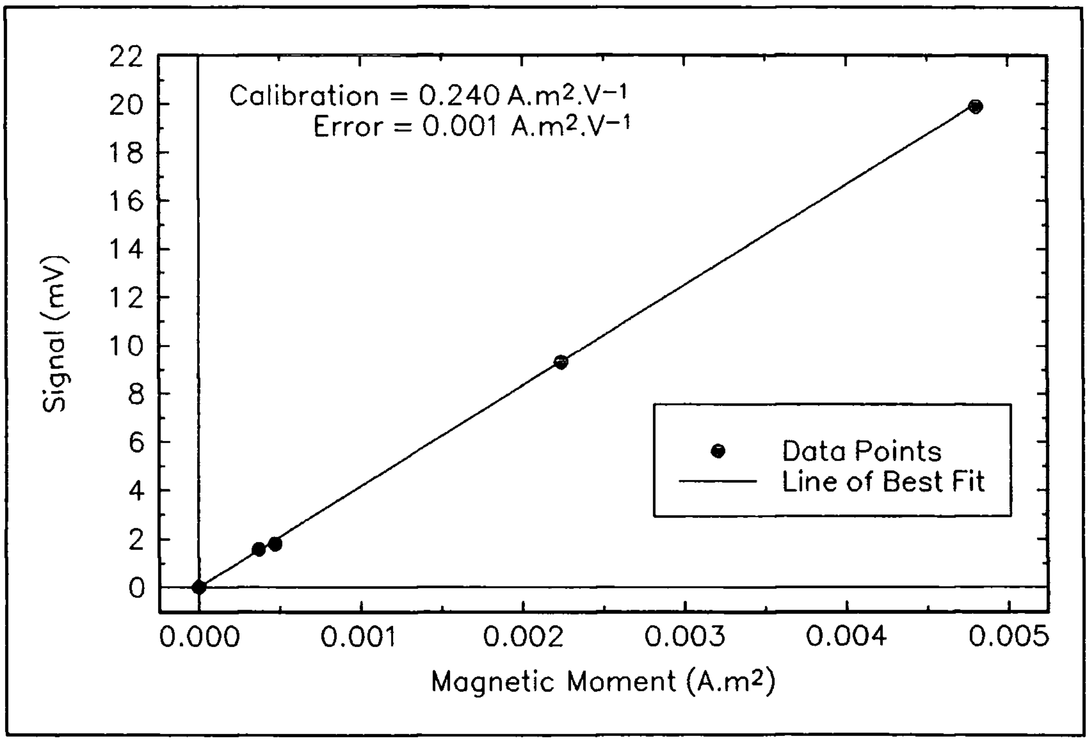

Figure 4.15 Calibration of VSM signal using the saturation magnetic moment of several nickel samples.

4.8 Summary.

A vibrating sample magnetometer system has been assembled to allow contactless determinations of critical current densities of superconducting materials. While most of the constituent components of the system have been bought from external manufacturers, a probe with detection coils has been designed, built and commissioned at Durham.

Major successes with the work have been the advancement of detection coil design, and adaptation of the system to take high quality data in a flux jumping Nb_3Sn magnet.

The system has been calibrated against the saturation magnetic moment of nickel giving $(0.240 \pm 0.001)A.m^2.V^{-1}$. The sensitivity at high magnetic fields $(B > 2T)$ is $5 \times 10^{-6}A.m^2$, and at low magnetic fields $(B < 2T)$ the sensitivity increases to $10^{-7}A.m^2$. This is not very good compared to $10^{-8}A.m^2$ commonly quoted [7] for an Oxford Instruments 12T VSM in magnetic fields up to 13T.

4.9 References.

[1] S. Foner "Versatile and Sensitive Vibrating-Sample Magnetometer" *Rev.Sci.Instrum.* **30** (1959) 548.

[2] S. Foner and E.J. McNiff "Very Low Frequency Integrating Vibrating Sample Magnetometer (VLFVSM) with High Differential Sensitivity in High dc Fields" *Rev.Sci.Instrum.* **39** (1968) 171.

[3] M. Springford, J.R. Stockton, and W.R. Wampler "A Vibrating Sample Magnetometer for use with a Superconducting Magnet" *J.Phys.E* **4** (1971) 1036.

[4] S.R. Hoon and S.N.M. Willcock "The design and operation of an automated double-crank vibrating sample magnetometer" *J.Phys.E* 21 (1988) 772.

[5] A. Zieba and S.Foner "Detection coil,sensitivity function, and sample geometry effects for vibrating sample magnetometers" *Rev.Sci.Instrum.* **53** (1982) 1344.

[6] S.Foner "Further improvements in vibrating sample magnetometer sensitivity" *Rev.Sci.Instrum.* **46** (1975) 1425.

[7] D-N. Zheng "An experimental study of flux pinning in high temperature superconductors" *PhD. Thesis* University of Cambridge, (UK) 1994.

[9] "CRC Handbook of Chemistry and Physics" 56th ed. *CRC Press.*

5. Thermometry

5.1 Introduction.

This chapter details a major investigation of closed gas thermometry for use in magnetic fields up to 17T from 4.2K to 130K within a 20mm bore. Many VSM's (e.g. [1]) use a gas flow cryostat. This works by drawing cryogen from the bath through a needle valve in the bottom of the cryostat, which is then passed through a heat exchanger made of copper that has been heated to the appropriate temperature. The sample in the gas is assumed to be at that temperature. However this is not an ideal system as needle valves at 4.2K can be unreliable. Due to the nature of the measurement the sample under test is several centimetres away from the well defined temperature of the heat exchanger, which raises questions about accuracy of temperature measurement, and in this respect the flow rate of the gas is crucial [2]. Finally a gas flow cryostat would have taken all 40mm bore of the 17T magnet.

The advantages of the small bore closed system are that the thermometer is closer to the sample, and additional inserts within the magnet bore may be used. The aim is to achieve a stable and uniform temperature within the VSM probe. Using the ideas developed, variable temperature measurements have been made on single crystals of $YBa_2Cu_3O_{7-\delta}$ from 77K to 95K (chapter 6) and from 4.2K to 10K on NbTi multifilamentary wire (chapter 7).

The chapter begins with details of the components of the thermometry system, such as temperature sensors, temperature and pressure controllers, heaters and thermal insulation. This is followed by the major part of the work, the investigation of temperature differences between the temperature sensor and the sample, along with how these problems have been dealt with. The use of a thermocouple and carbon-glass temperature sensor to measure directly sample temperature is investigated. Finally there is a summary of what has been achieved.

5.2 Temperature Control and Measurement in the VSM.

This section details the hardware of the variable temperature system in the VSM probe. It is split into two parts, the first covering aspects of cryogenic design of the probe and the second dealing with temperature measurement and electronic systems. An overview of the system is shown in figure 5.1.

5.2.1 Design of Thermal Environment.

There are two heaters that are connected in parallel within the probe as shown in figure 5.1. The **foil heater** is around the inside of the coil set and has a resistance of 45Ω. A 27Ω **wire heater** is wound around the outside of the stainless steel support tube, electrically insulated from it by cigarette paper and G.E. varnish.

The purpose of this arrangement is to provide uniform temperature profile across the whole area at the bottom of the probe. The external **variable resistor** is used to alter the currents (and hence power dissipated) in each heater. The need for this is highlighted in section 5.3. The currents in each heater are measured using **DVM4** and **DVM5**.

The end of the probe where the sample sits has been thermally isolated. This was done as it is believed that the less heat flows in or out of the probe, the easier will be the control of the system's temperature, and to reduce the consumption of liquid helium. Radiation shielding has been provided by several layers of **superinsulation** (aluminised mylar film) around the outside of the coil set and the support tube beyond. Conduction heat leaks down the probe have been reduced by replacing 75mm of the brass sample rod approximately 100mm from the sample with **tufnol rod**. This acts as a thermal "resistor" due to its lower thermal conductivity. **Tufnol tubing** has replaced a 100mm stainless steel support tube section in a similar fashion.

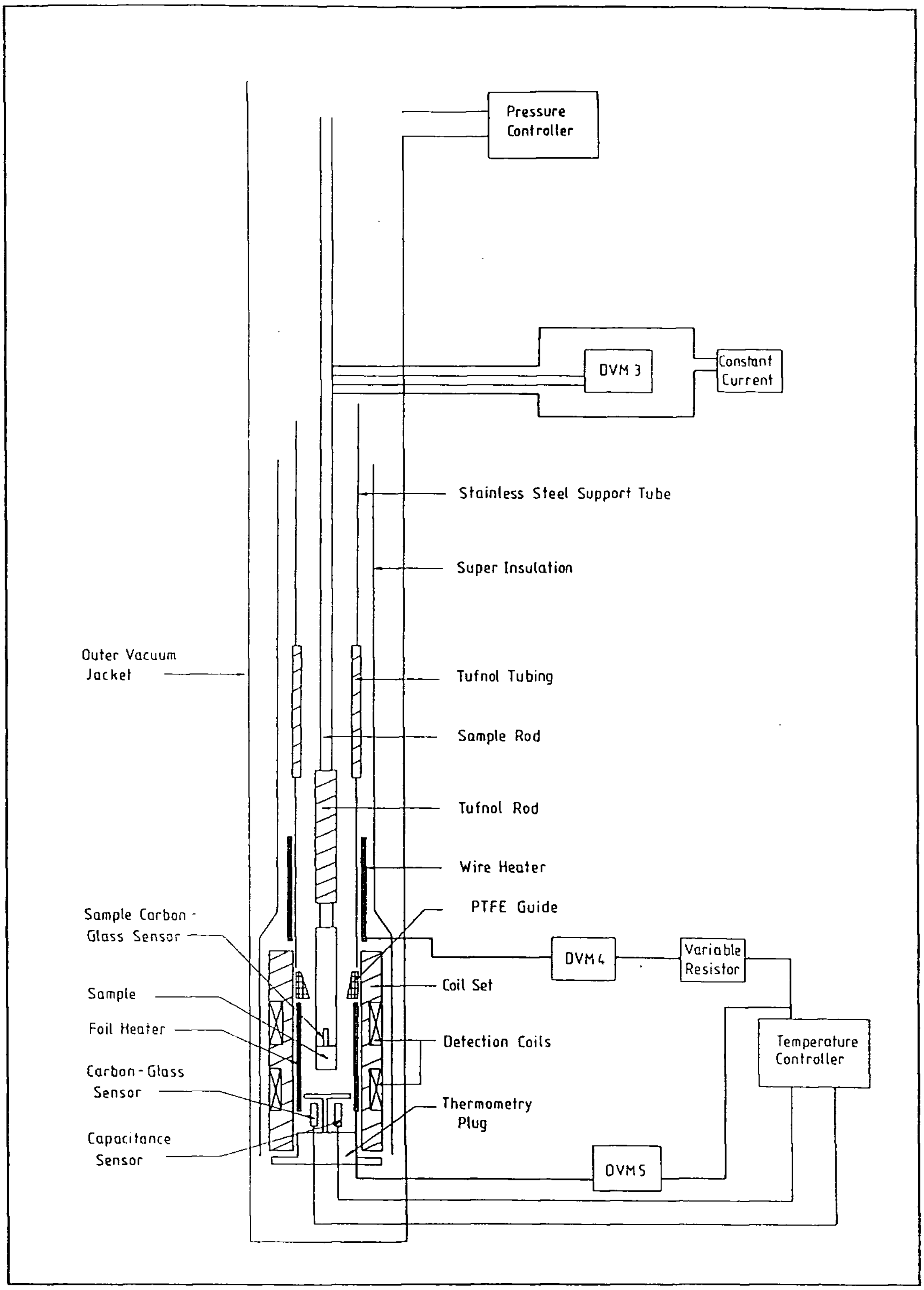

Figure 5.1 Thermometry in the Durham Superconductivity Group Vibrating Sample Magnetometer.

5.2.2 Temperature measurement and Control.

There are two thermometers in the probe. The **carbon-glass sensor** is used to measure accurately the temperature of the sample space in zero applied field. This is very reproducible [3], and good at low temperatures ($T < 100K$) where its high negative differential resistance makes it very sensitive. The carbon-glass senor is dependent upon magnetic field and so the **capacitance sensor** is used as the control sensor of the system. Ceramic capacitance sensors have virtually no magnetic field dependence [4], but the value of capacitance at a particular temperature is not reproducible upon thermal cycling. Both sensors are mounted in the tufnol **thermometry plug** within the coil set and thermally connected to the heater by silicone vacuum grease.

The Lakeshore **temperature controller** maintains the temperature within the probe. This reads both the temperature sensors and powers the heater for the probe. Care must be taken with this instrument as it does not measure the resistance of the carbon-glass sensor correctly. The systematic error is presented in figure 5.2. The user has control on the proportional (P), integral (I) and differential (D) parameters of the feedback in the controller, ensuring that the controller goes to the correct set-point and eliminating problems with long term drift. These parameters change with temperature, namely when temperature increases the proportional parameter has to be reduced and the integral time increased. Rate is not used in this system as it is a safeguard against overshoot.

The pressure of helium gas within the probe is important, as it provides the main method of heat transfer between the heaters and the sample, as well as having an impact on the time response of the system. The helium gas used is passed through a liquid nitrogen trap to remove any water vapour or oxygen from it that may affect the system. Pressure of helium transfer gas is controlled within the probe by the use of an MKS self-tuning valve **pressure controller**, which by the use of separate sensing units has two ranges 1-1000Torr (±1Torr) and 1-1000mTorr (±1mTorr).

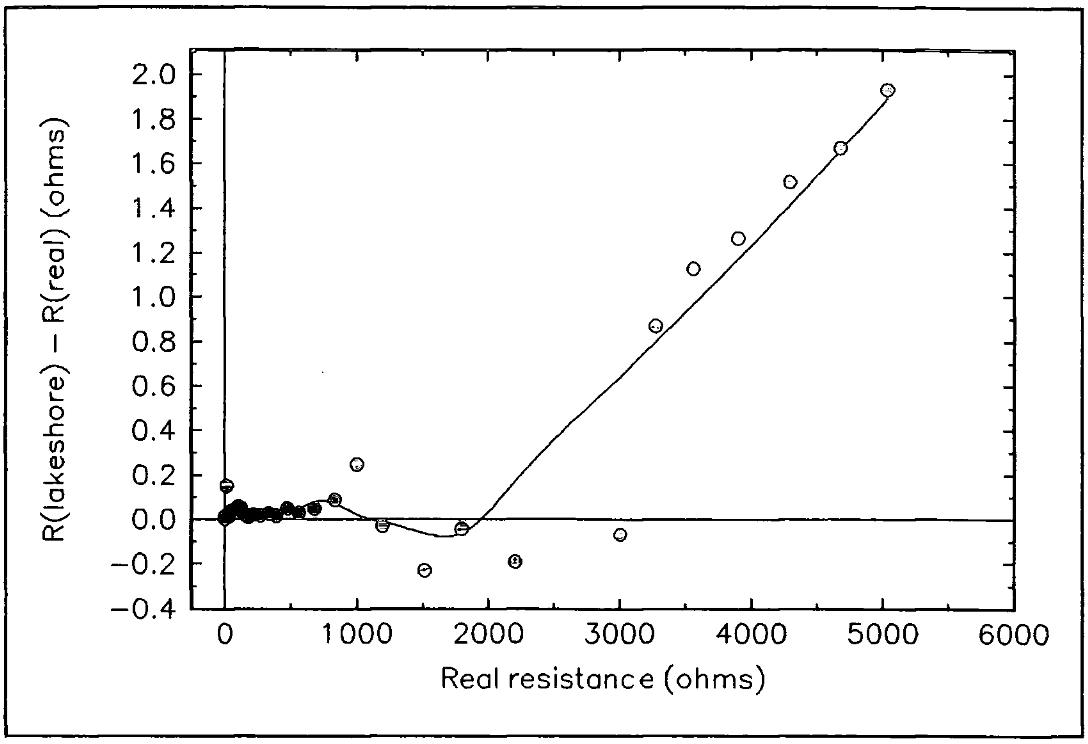

Figure 5.2 Systematic error in resistance measurement of the Lakeshore temperature controller. Line is a guide to the eye.

5.3 Temperature Differences.

Even in the closed gas, 20mm bore system described above the sample and the sensor are not in exactly the same place, and therefore may not be at the same temperature. This can be allowed for if a thermometer is placed on or near the sample. However this is not desirable in a VSM as extra signal due to this thermometer will be detected. In order to measure this difference a calibrated rhodium-iron (RhFe) temperature sensor was mounted as if it were a sample. The temperature difference, ΔT, is defined as:

$$\Delta T = T(RhFe) - T(CG)$$

therefore if $\Delta T > 0$ the sample is too hot,
$\Delta T < 0$ the sample is too cold.

This section is split into three parts that formed essentially separate investigations of the temperature differences in different conditions. The first is temperature differences at temperatures between 77K and 130K. Temperature differences at 4.2K and above are dealt with in two parts, those between 4.2K and 30K, and those from 4.2K to 120K.

5.3.1 Temperature Differences from 77K to 130K.

Initially it was thought that the temperature difference could be controlled using just the foil heater and by varying the pressure of helium gas within the probe. The results of this exercise are presented in figure 5.3. From this it is obvious that there is no single pressure that is useful. The probable reason for the offset on the 1 Torr and "0" Torr (below the 4×10^{-2}mbar limit of the Pirani gauge) data is that the heat leak down the probe is significant at low pressures.

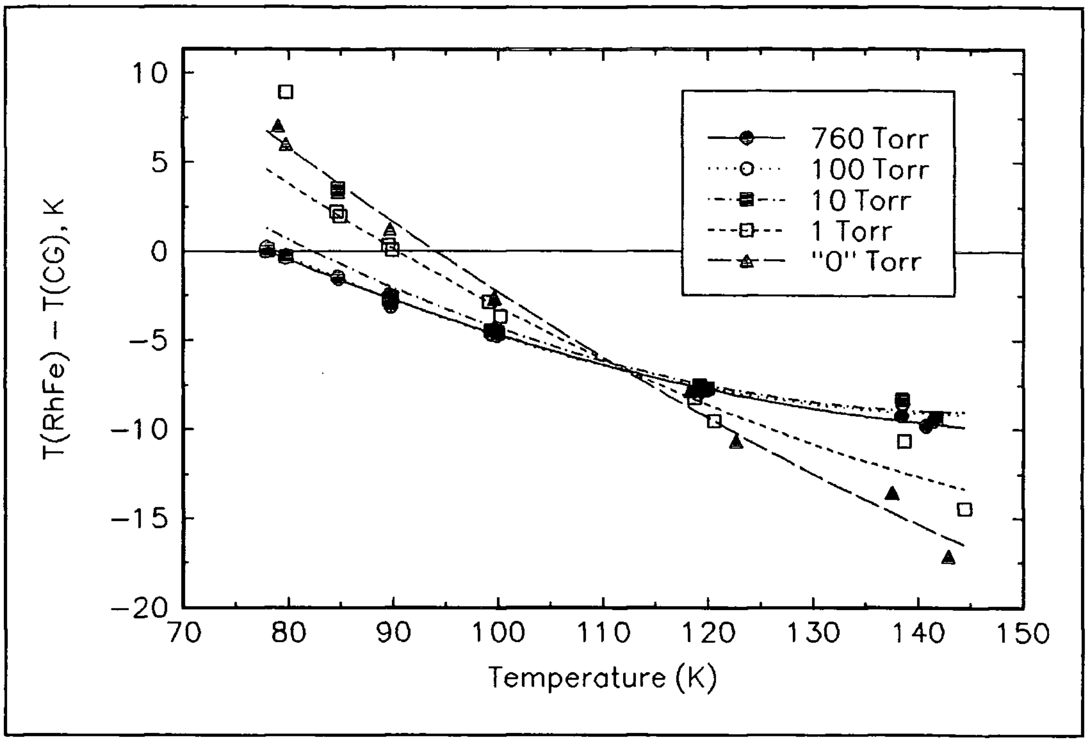

Figure 5.3 Temperature differences as a function of the pressure of helium transfer gas in the probe.

The next stage of the development was to add a second heater (see figure 5.1), wound non-inductively with constantan resistance wire. Figure 5.4 presents the results of this exercise for various heaters in series with the foil heater. The conclusion to be drawn from this is that no single heater will be suitable over the full range of temperatures.

To allow for this in use a 27Ω wire heater is placed in parallel with the foil heater. The relative power dissipated through each heater is changed in-situ by an external variable resistor which may be put in series with either heater. To discuss results gained this way, the term *ratio* (of heater current) has to be defined:

$$Ratio = \frac{I_{foil}}{I_{wire}}$$

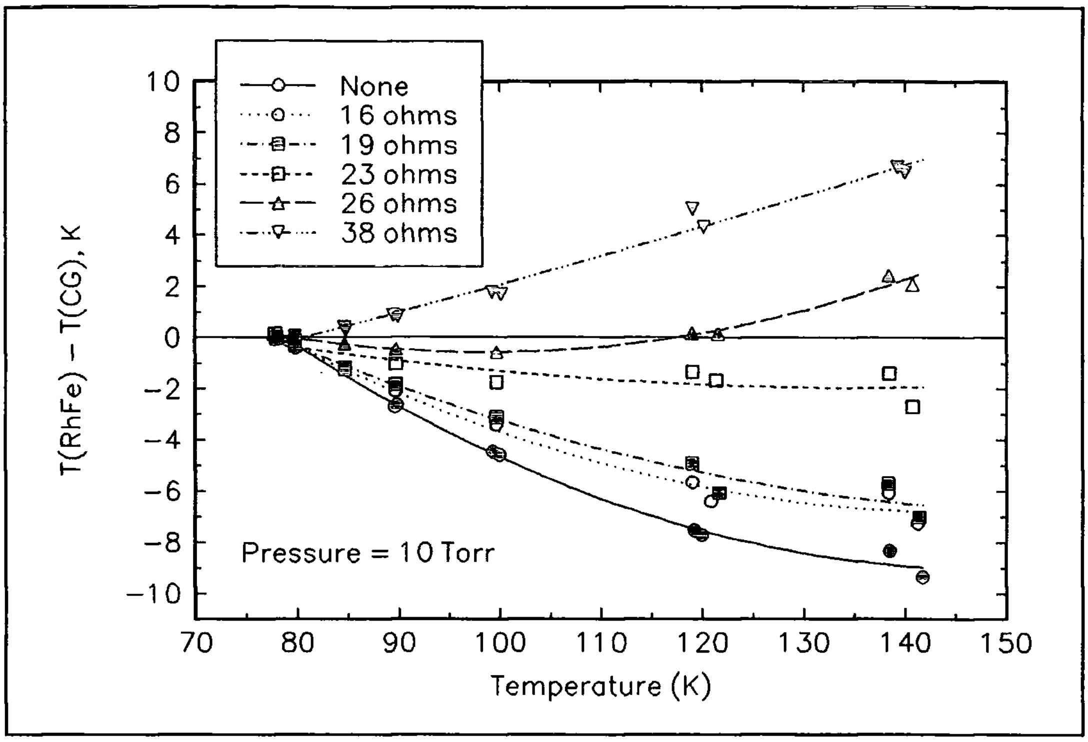

Figure 5.4 Temperature differences when different fixed value second heaters are used in the VSM probe.

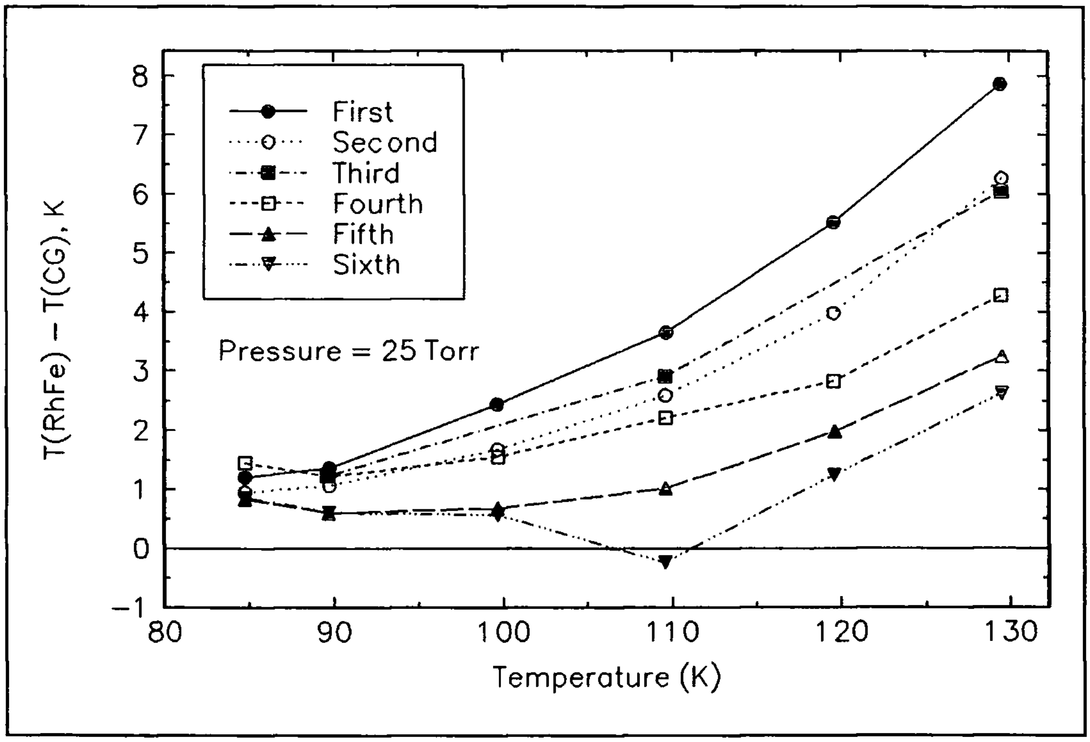

Figure 5.5 Several measurements of temperature difference with a heater current ratio of 0.5.

Figure 5.5 shows six different experiments at 25 Torr with a ratio of 0.5, these were done to check how reproducible was the system. As can be seen from the figure it is not reproducible. It was noted that the power delivered from the Lakeshore temperature controller was not reproducible either. Therefore in order to characterise the system properly *power* had to be measured, and it is defined as:

$$Power\ (W) = (I_{foil})^2 \times 45 + (I_{wire})^2 \times 27$$

Graphs of ΔT against power as a function of ratio at fixed temperature and pressure were produced.

Six experiments were performed at 5 Torr for the ratios 0.750, 0.925, 0.970 and 1.050 at 85, 90, 100, 110, 120, 130K. The plots of ΔT against power are presented in figures 5.6-5.11. A criteria for acceptable temperature difference was set to be ±200mK, and this is represented on the graphs with horizontal dotted lines. The lines joining the data in the graphs are polynomial fits as guides to the eye.

The data at 85K is presented in figure 5.6. All measured temperature differences were less than 1K. The graph shows well that if the power is increased at a fixed ratio then the sample temperature increases also. In figure 5.7, at 90K, the magnitudes of the temperature differences are greater, and it can be seen that if the ratio of the heater currents is increased at fixed heater power the sample temperature decreases.

At 100K (figure 5.8) none of the data points fall within the ±200mK acceptable range. However, the data show the same predictable trends as those at 85K and 90K. Therefore it is reasonable to use the data to extrapolate the ratios that have been measured, or suggest ratios that may give the acceptable limit. Figure 5.9, at 110K is similar to the data at 100K. Here the maximum temperature difference is 4K, which follows the pattern of increasing temperature leads to increased temperature differences

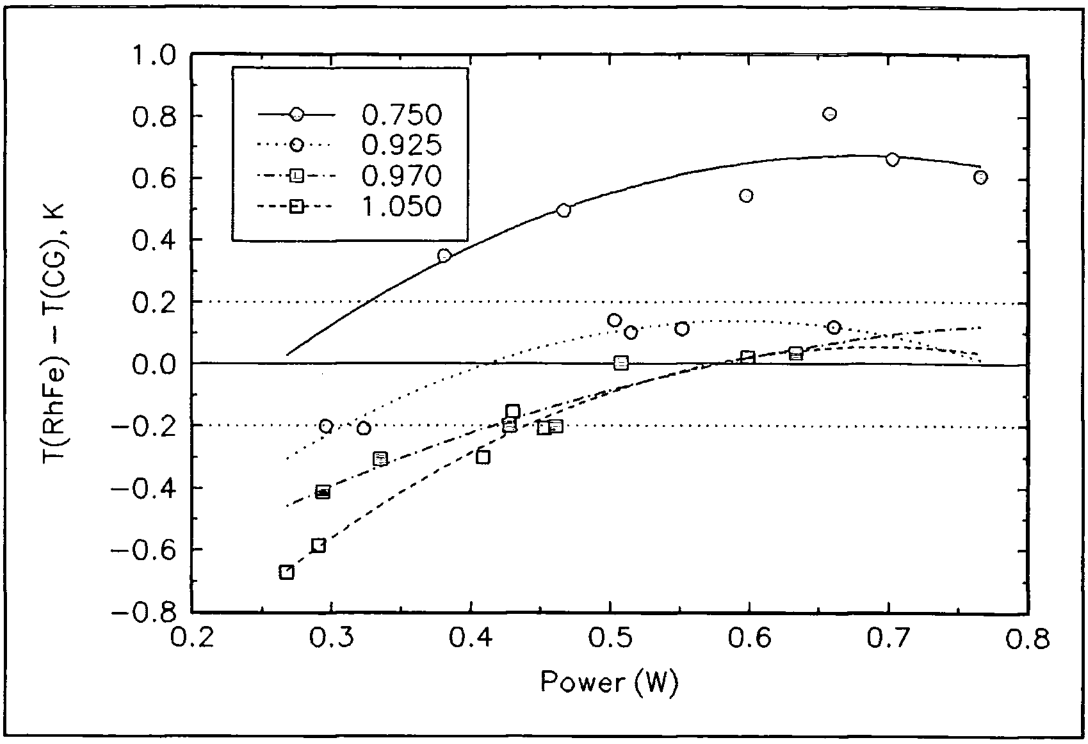

Figure 5.6 Temperature differences at 85K and 5 Torr as a function of power at fixed heater current ratio. Lines are a guide to the eye.

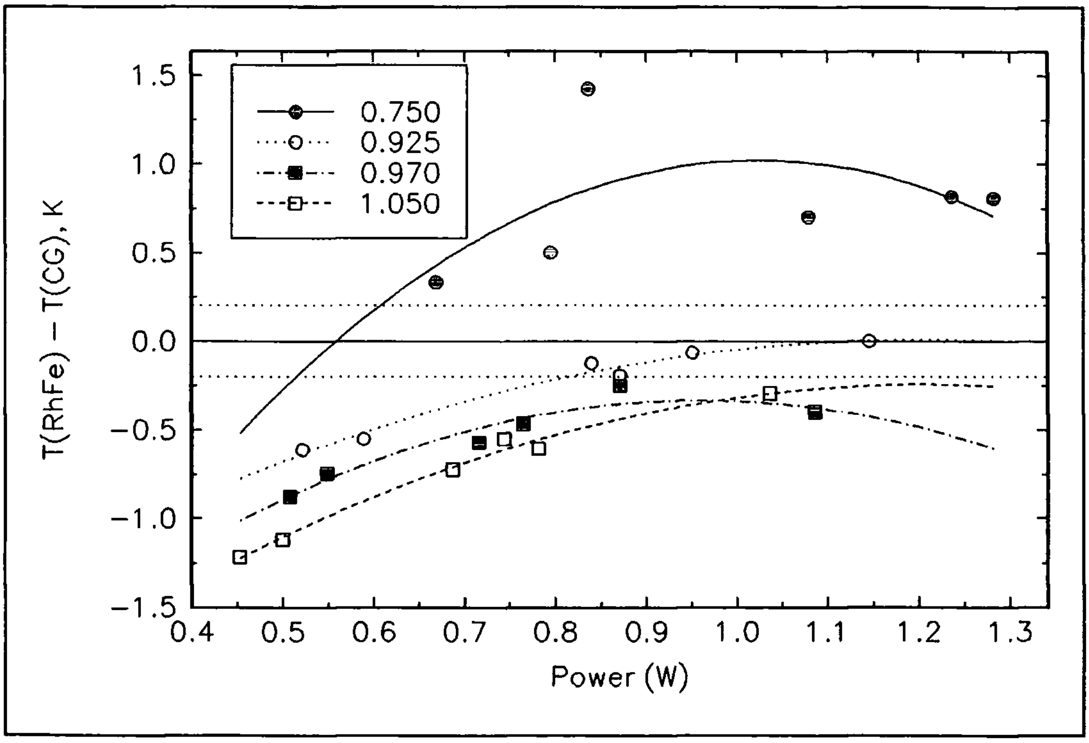

Figure 5.7 Temperature differences at 90K and 5 Torr as a function of heater power at fixed heater current ratio. Lines are a guide to the eye.

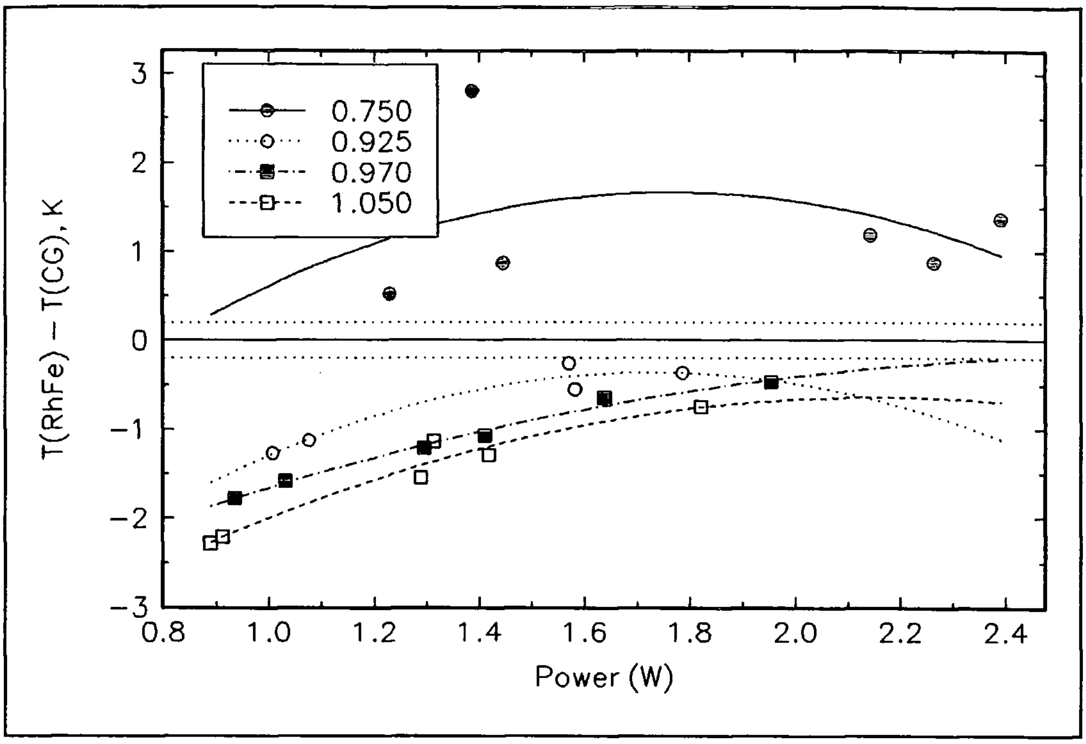

Figure 5.8 Temperature differences at 100K and 5 Torr as a function of heater power at fixed ratios of heater current. The lines are as a guide to the eye.

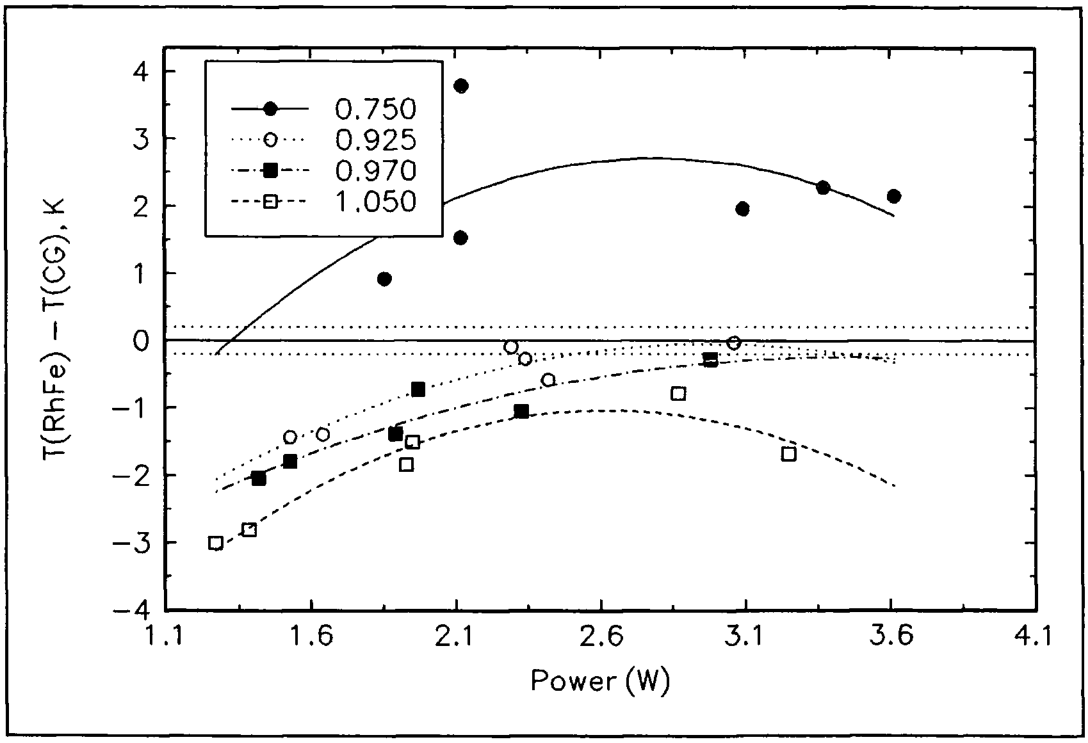

Figure 5.9 Temperature differences at 110K and 5 Torr as a function of heater power at fixed ratios of heater current. The lines are as guides to the eye.

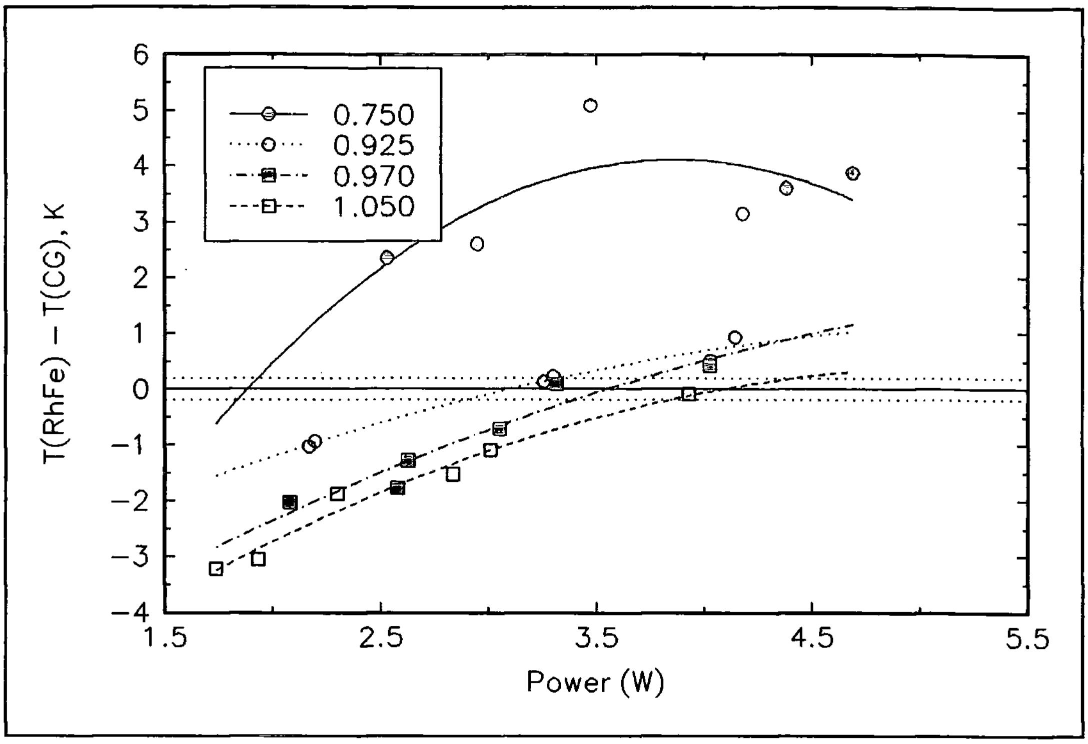

Figure 5.10 Temperature differences at 120K and 5 Torr as a function of heater power at fixed ratios of heater currents. The lines are guides to the eye.

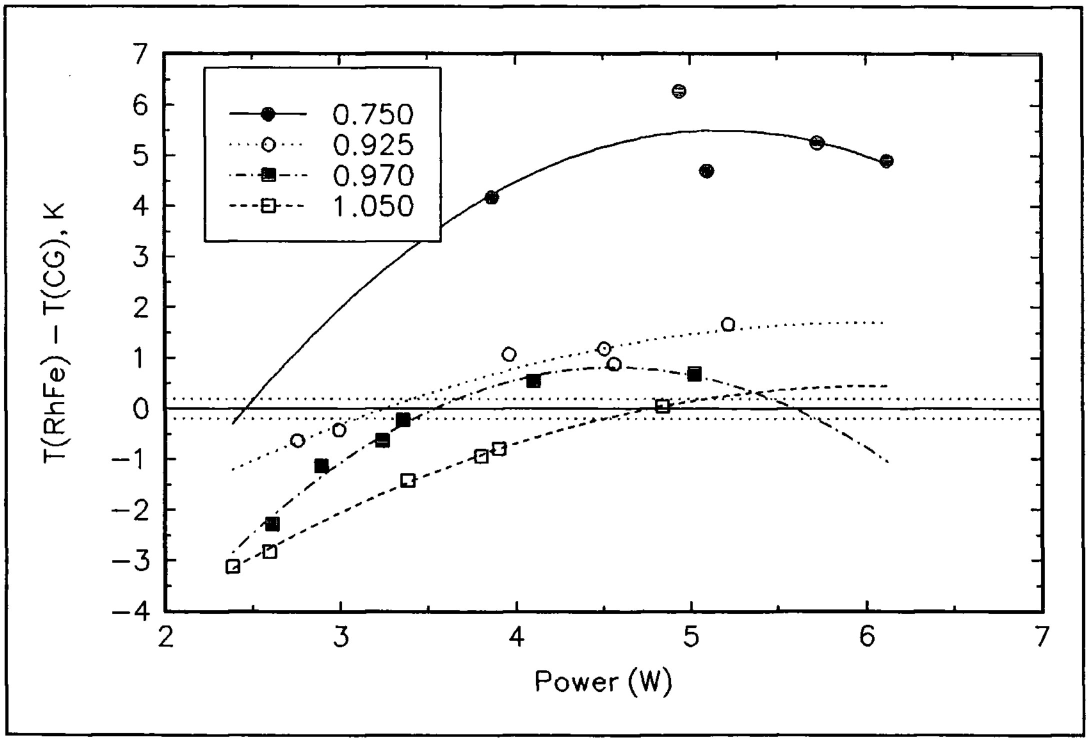

Figure 5.11 Temperature differences at 130K as a function of heater power at fixed ratios of heater currents. The lines are guides to the eye.

Figures 5.10 and 5.11 are graphs of temperature difference at 120K and 130K respectively. These data show the strong trends of those at lower temperatures. Again there is very little data within the ±200mK zone, but interpolations may safely be made.

From all of these graphs combinations of power and ratio can be extracted for each temperature that give the acceptable ±200mK temperature differences, and these are presented in table 5.1. Where "higher?" is indicated the experiments did not explicitly check the maximum allowable power.

Temperature (K)	Ratio	Lower P(W)	Upper P(W)
85	0.925	0.30	0.70
	0.965	0.42	0.62 (higher ?)
	1.050	0.45	0.60 (higher ?)
90	0.925	0.85	1.15 (higher ?)
100	0.925	1.80	2.20 (higher ?)
110	0.925	2.50	3.20 (higher ?)
	0.970	3.00	3.30 (higher ?)
120	0.925	2.70	3.20
	0.970	3.40	3.70
	1.050	3.90	4.50 (higher ?)
130	0.925	3.10	3.40
	0.970	3.30	3.60
	1.050	4.40	5.10

Table 5.1 Values of ratio and power that will give ±200mK temperature differences at 5 Torr in a liquid nitrogen bath.

After the success at 5 Torr in finding combinations of ratio and power in the heaters that will give ±200mK temperature differences, the experiment was repeated at atmospheric pressure. The advantage of this is that use of the pressure controller is unnecessary. Experiments were done with ratios 0.750, 0.775, 0.800, 0.825 and 0.850, at 85, 90, 100, 110, 120 and 130K. Figures 5.12-5.17 show ΔT against power at fixed temperature and ratio. The acceptable criteria of ±200mK is represented by the horizontal dotted lines.

In figure 5.12, which is at 85K, it is seen that the temperature differences are all less than ±1K. Also if the ratio is increased the temperature of the sample decreases, as with the 5 Torr data. At 90K (figure 5.13) similar behaviour is seen. The dependence of the temperature difference with power is somewhat different to that seen at 5 Torr. Here at low powers the temperature difference is high and positive, it dips to be negative, and then at high powers is again high and positive.

The data at 100K (figure 5.14) has less pattern to it. Unlike the 5 Torr work polynomial fitting could not be applied to this more "noisy" data. It would be very difficult to use this data to predict any trends, as the scatter on the data is approximately 400mK. In figure 5.15 (110K) the data is less scattered and this could be confidently used to extract combinations of ratio and power for acceptable thermal gradients.

Both of figures 5.16 and 5.17 (at 120K and 130K respectively) show data with scatters of approximately 1K or 2K. Clearly this data cannot be used to find conditions for acceptable thermal gradients.

In summary the atmospheric pressure data shows that while the system is simpler at atmospheric pressure than at 5 Torr, the temperature differences are not as easy to predict as at 5 Torr. Therefore for thermometry within a liquid nitrogen bath a pressure of 5 Torr is used and heater ratio and power are set using the external variable resistor in accordance with table 5.1.

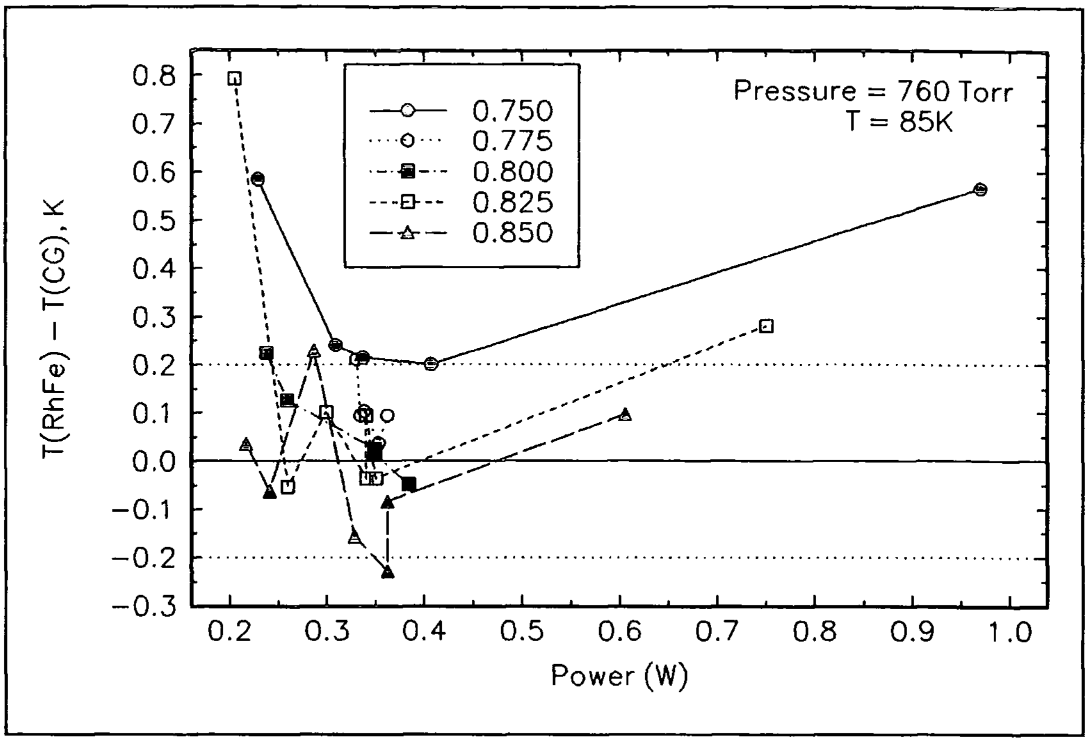

Figure 5.12 Temperature differences as a function of heater power at fixed ratio of heater currents.

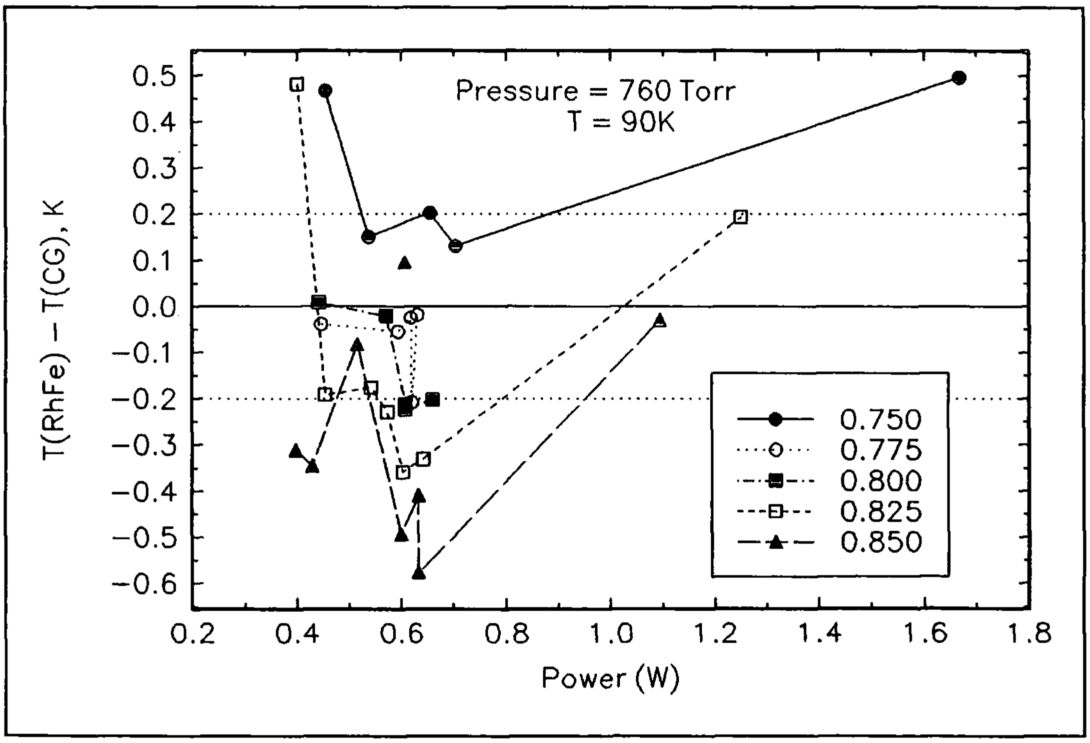

Figure 5.13 Temperature differences as a function of total heater power at fixed ratios of heater currents.

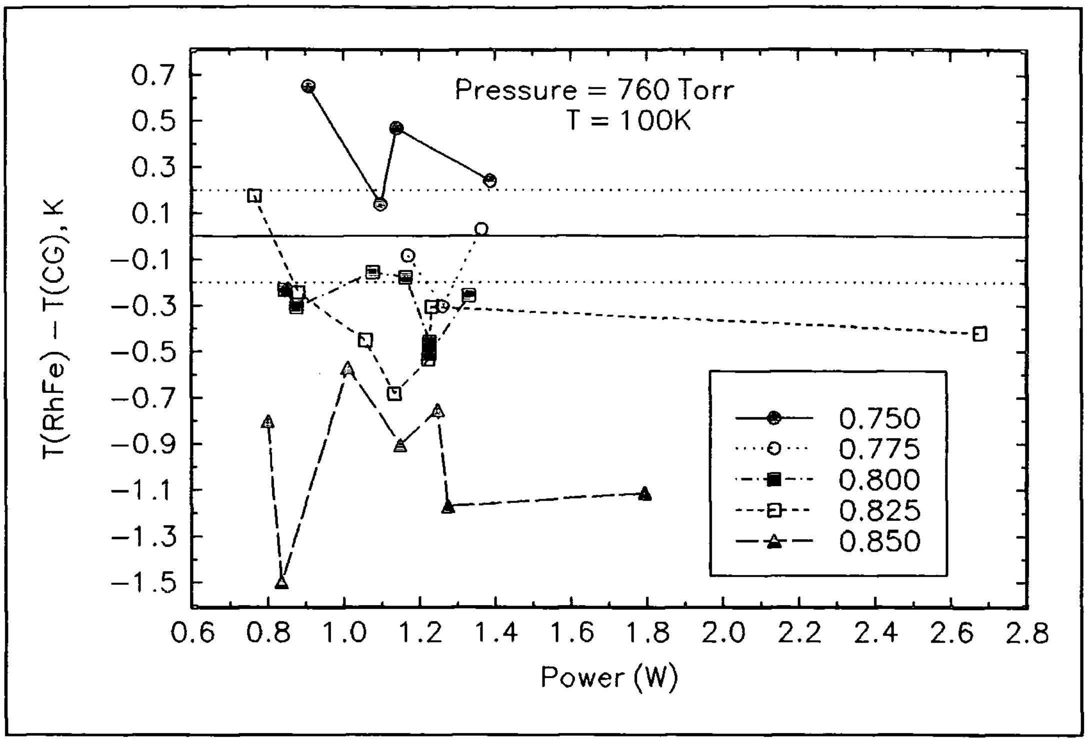

Figure 5.14 Temperature differences as a function of total heater power at fixed ratios of heater currents.

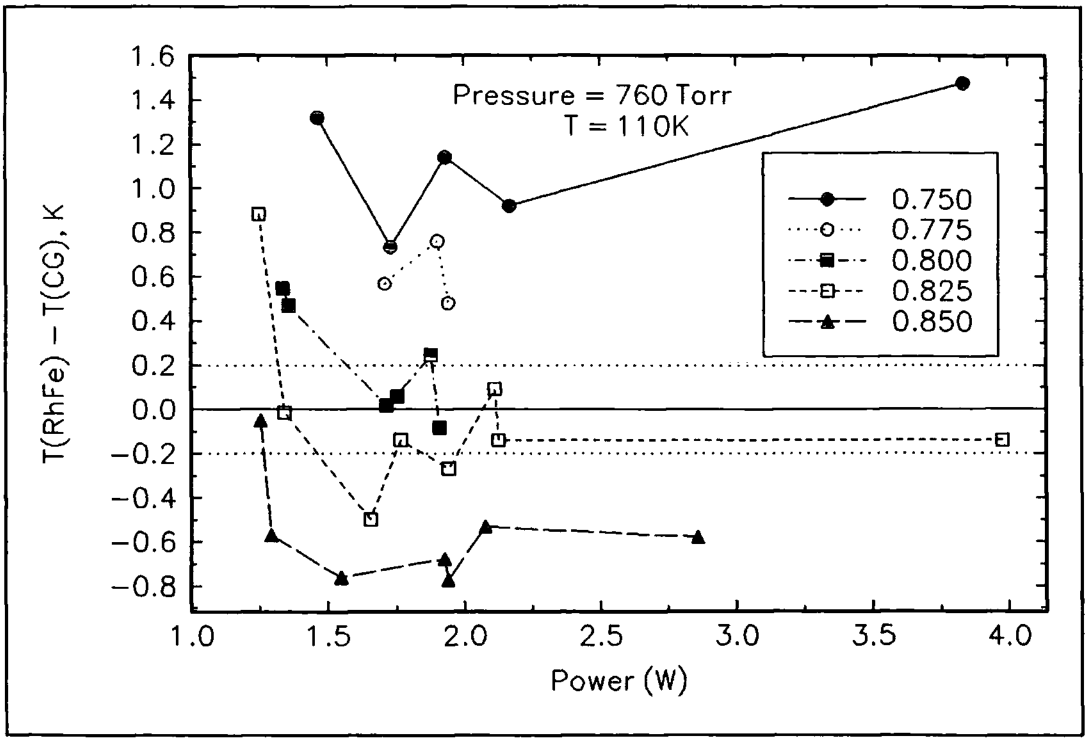

Figure 5.15 Temperature differences as a function of total heater power at fixed ratios of heater currents.

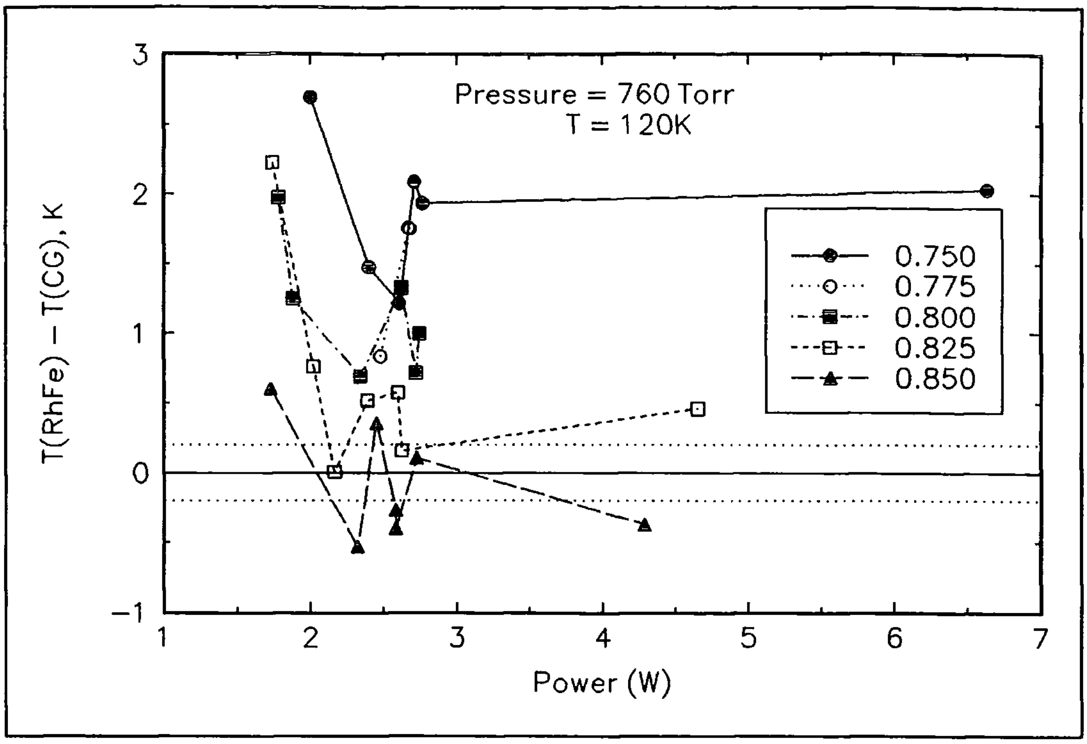

Figure 5.16 Temperature differences as a function of total heater power at fixed ratios of heater current.

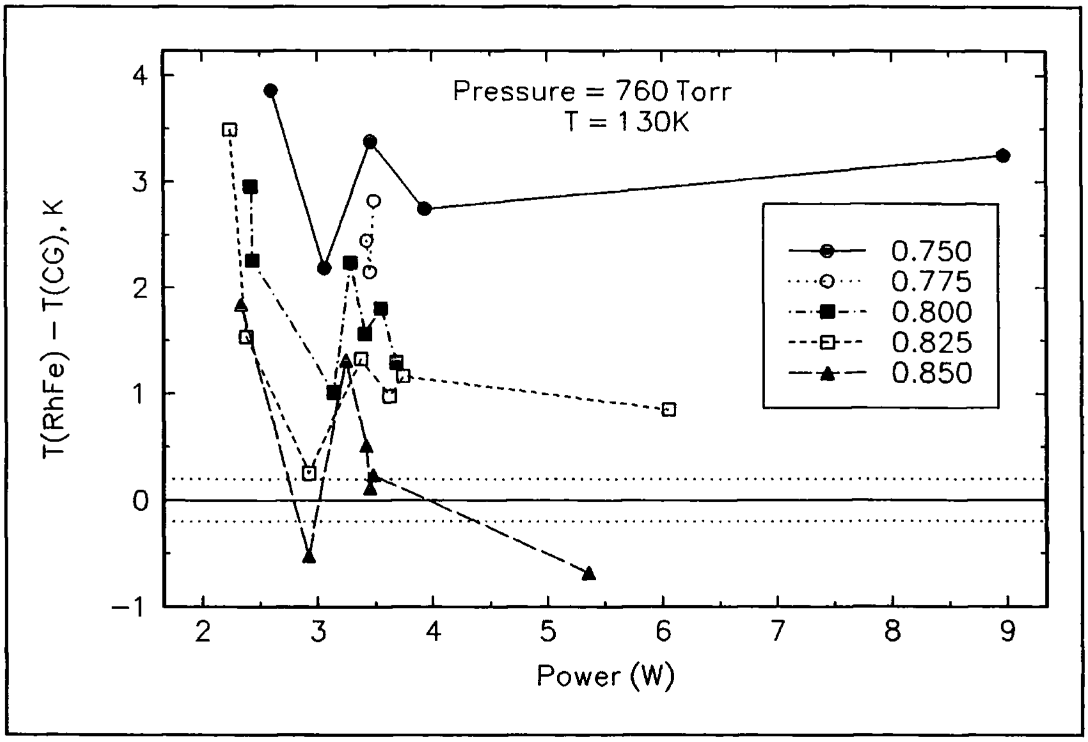

Figure 17 Temperature differences as a function of total heater power at fixed ratios of heater currents.

5.3.2 Temperature Differences from 4.2K to 30K.

The temperature differences were considered separately in this range as it will cover the range of low temperature superconductors, for example NbTi (T_c=9K), Nb_3Sn (T_c=18K) and $PbMo_6S_8$ (T_c=14K). A helium gas pressure of 100Torr was used as it gives faster response in the system, and at these low temperatures does not significantly increase the boil-off rate of the liquid helium. Measurements of ΔT against heater power were made at a helium gas pressure of 100 Torr. Two ratios were measured , 0.700 and 0.770, from 10 to 30K in 5K steps. The results are presented in figures 5.18-5.22. The horizontal dotted lines on the graphs are at ±200mK, which again is the criteria for an acceptable temperature difference.

Figure 5.18 presents the data taken at 10K. The scatter of the data is approximately 100mK. The two ratios are seen to occur in distinct groups. These data were taken over two days, at many different cryogen levels. From this it may be assumed that the system is much more repeatable than that from liquid nitrogen temperatures and above. This is re-inforced by the data at 15K which is shown in figure 5.19.

Similar behaviour is seen in figure 5.20 which is at 20K. Note from this that increasing the ratio causes the sample temperature to decrease, as seen in section 5.3.1. The same is true in figure 5.21 (25K) where one may see that the higher the power, the higher is the sample temperature. Figure 5.22 confirms all the trends that have been seen before at 30K.

The conclusion that may be drawn from this exercise is that these data are very repeatable, despite having been taken over two days and at a range of cryogen levels. This is probably due to the superior nature of the cryostat provided with the Oxford 15/17T magnet. Table 5.2 summarises the combinations of heater power and ratio needed at 100Torr for acceptable temperature differences between 4.2K and 30K.

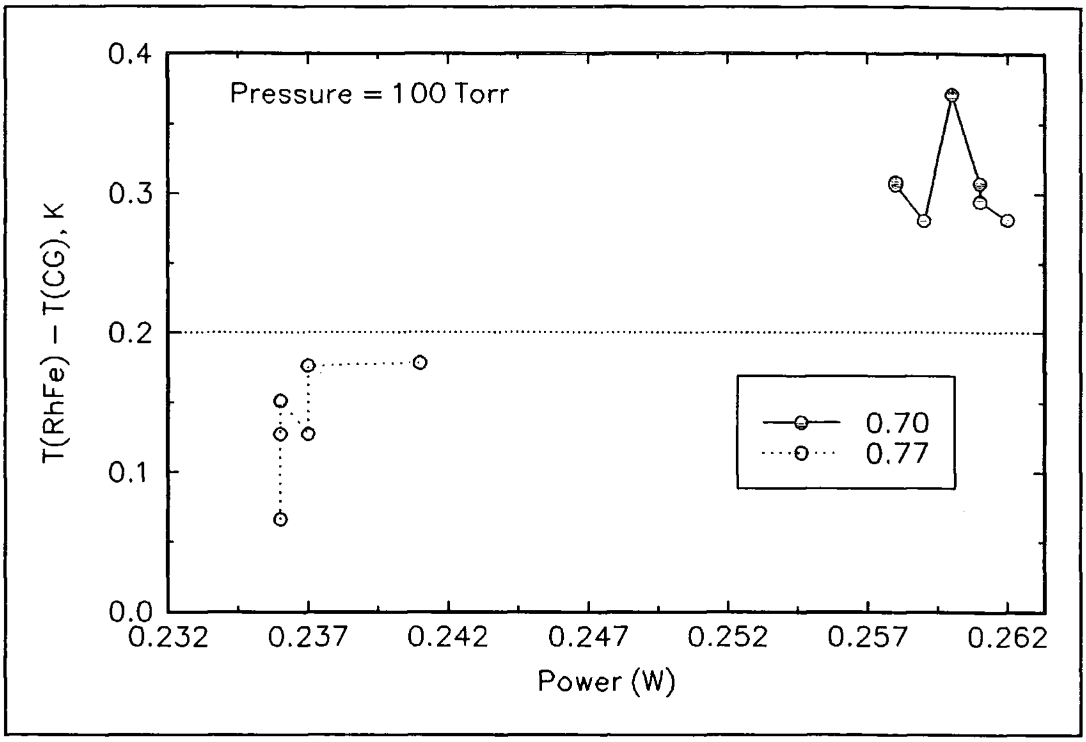

Figure 5.18 Temperature differences at 10K as a function of power at fixed ratios of heater current.

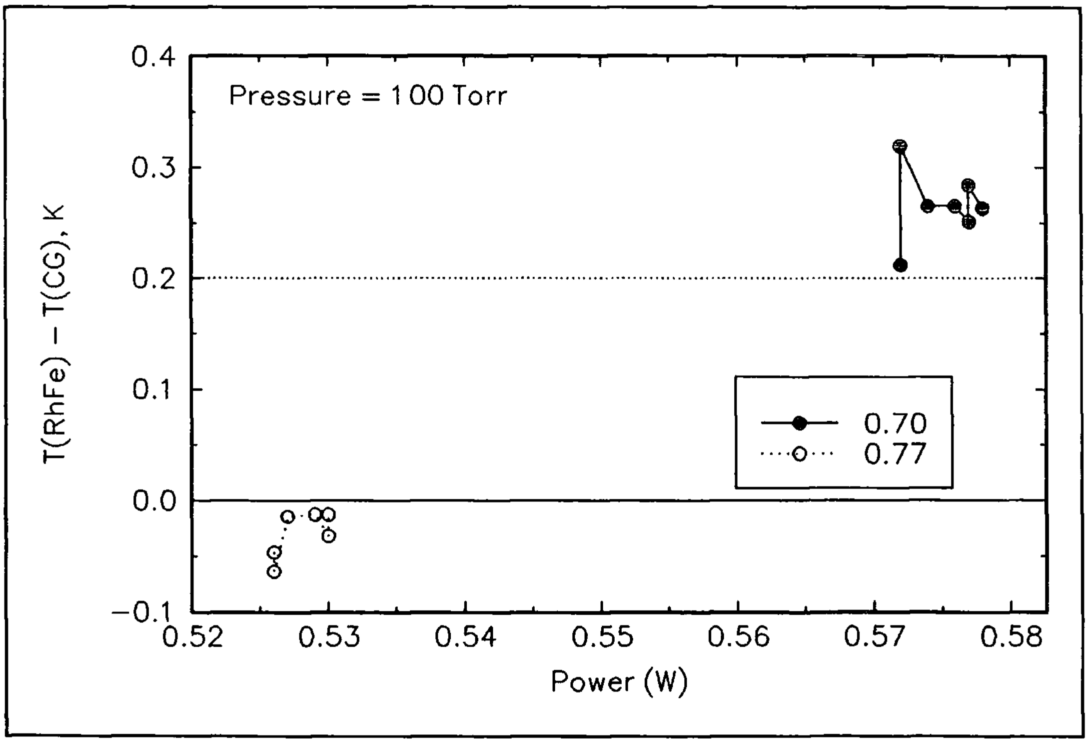

Figure 5.19 Temperature differences at 15K against heater power at fixed ratio of heater current.

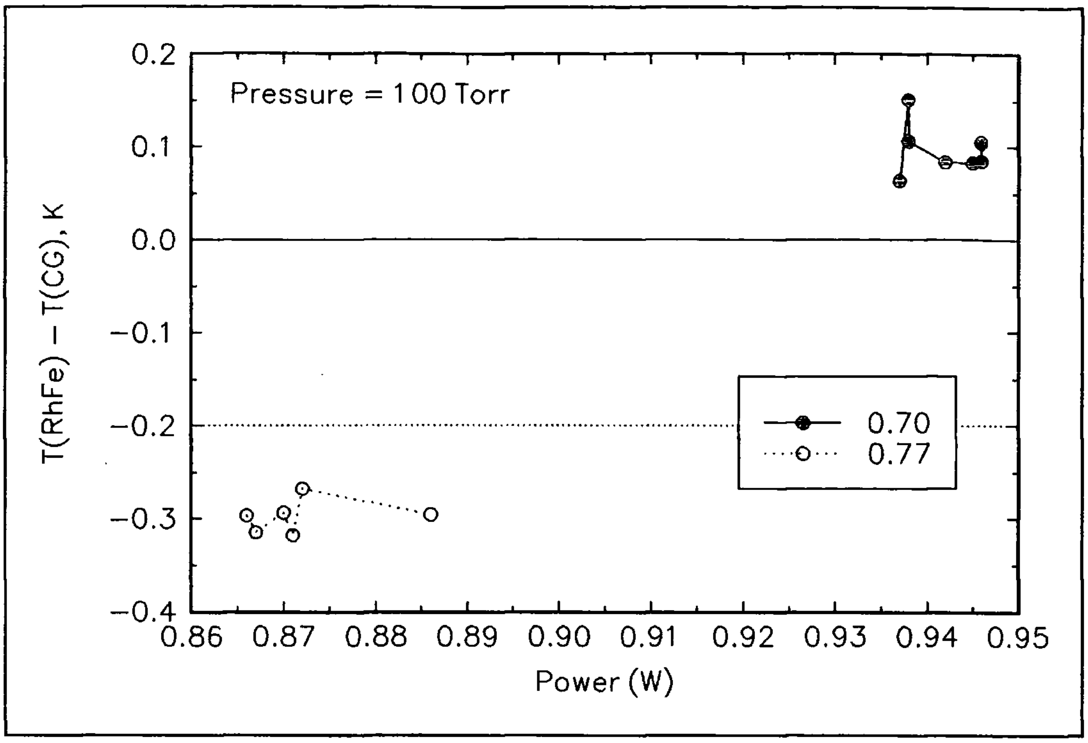

Figure 5.20 Temperature differences at 20K against heater power at fixed ratios of heater current.

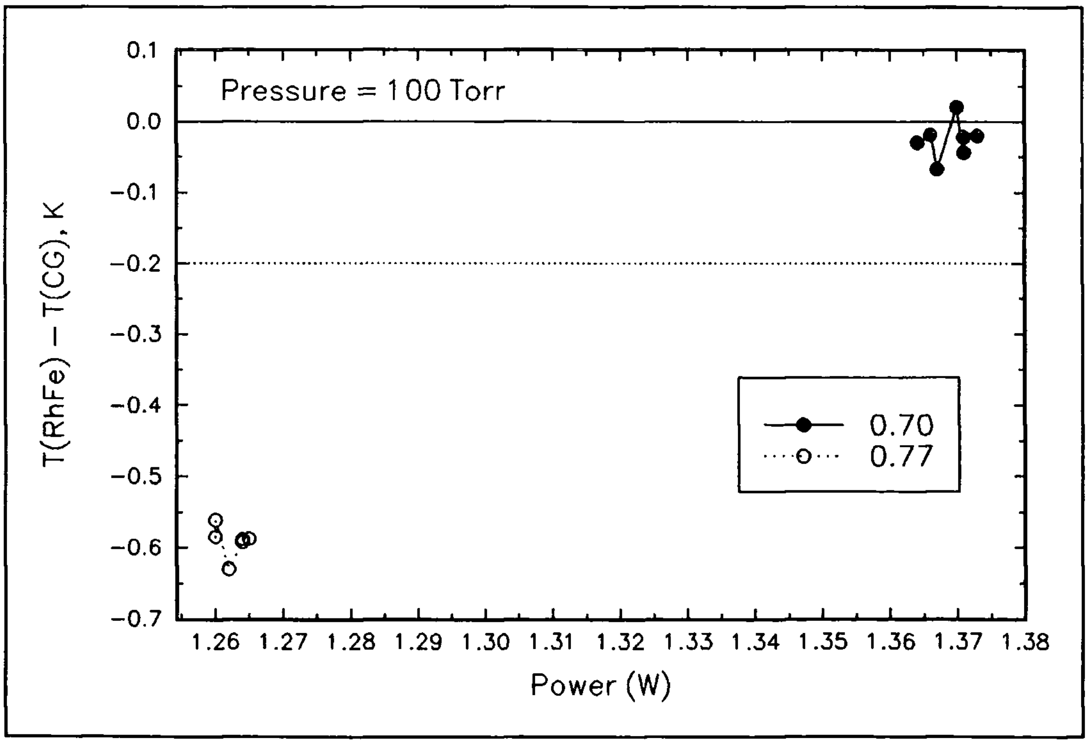

Figure 5.21 Temperature differences at 25K against heater power at fixed ratios of heater current.

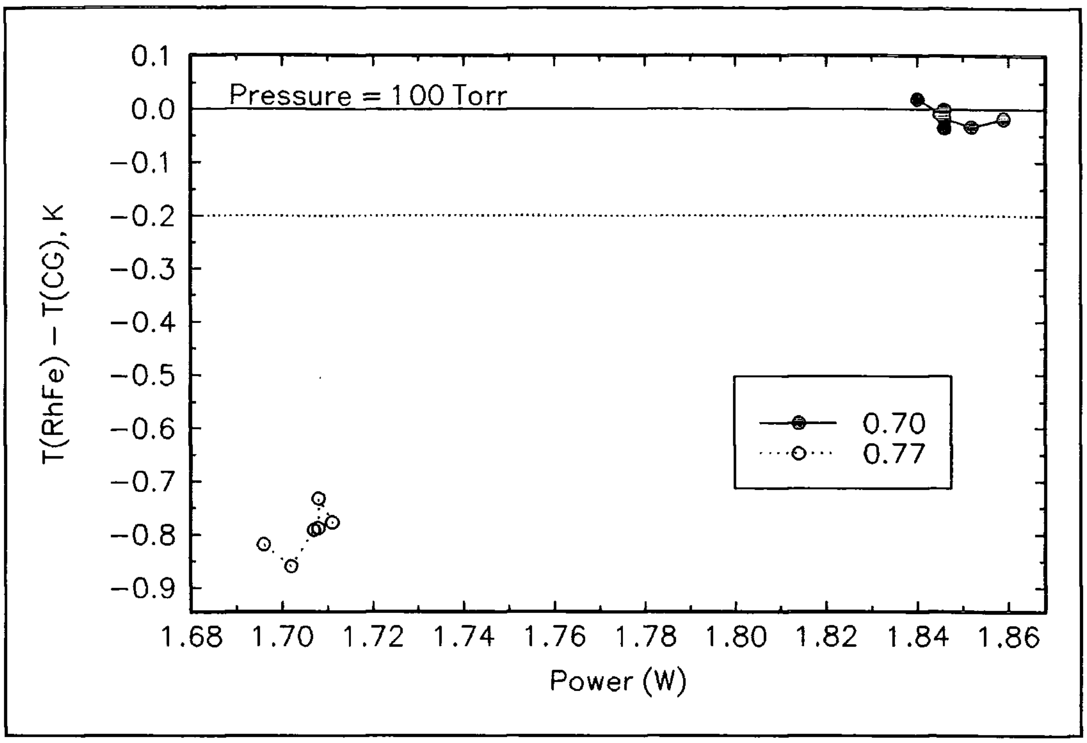

Figure 5.22 Temperature differences at 30K against heater power at fixed ratios of heater current.

Temperature Range (K)	Ratio	Power Range (W)
4.2 → 17	0.770	0.0 → 0.6
17 → 30	0.700	0.8 → 2.0

Table 5.2 Criteria for acceptable (±200mK) thermal gradients below 30K in a 100 Torr helium gas atmosphere.

5.3.3 Temperature Differences from 4.2K to 120K.

This range of temperature is considered separately to the 4.2K to 30K range, because it is impractical to use pressures of 1 Torr and above at temperatures of 60K and greater due to the excessive boil-off rate of the liquid helium.

Initially the helium gas within the probe was not pressure controlled, but was continuously pumped by an Edwards $12m^3hr^{-1}$ rotary pump. The use of a diffusion pump was unnecessary as the boil-off of liquid helium at high temperatures was not excessive. Use of the very low pressures increases the response time of the system, leading to temperature control problems which in this case prevented any data being taken at 100K and 120K. Measurements were taken of ΔT against power with fixed ratios at 20K intervals from 20K-80K. The results of this series of experiments are presented in figures 5.23-5.26.

At 20K (figure 5.23) and 40K (figure 5.24) if the ratio is increased then the sample temperature increases. Both of these data sets show well defined lines for each different ratio and this may be used for interpolation purposes to find a combination of ratio and power that would give an acceptable (±200mK) temperature difference.

The data in figure 5.25 (60K) and figure 5.26 (80K) are somewhat different. The trends are less smooth, typical scatter being 2K in the worst case in figure 5.25. While combinations of power and ratio may be found they are not of much practical use. This is because at fixed ratio the rate of change of thermal gradient with respect to power is very high. For example if during an experiment at 60K and a ratio of 0.515, the power required for heating changes from 1.2W to 1W then the temperature difference would change by 4K. At 80K the situation is worse.

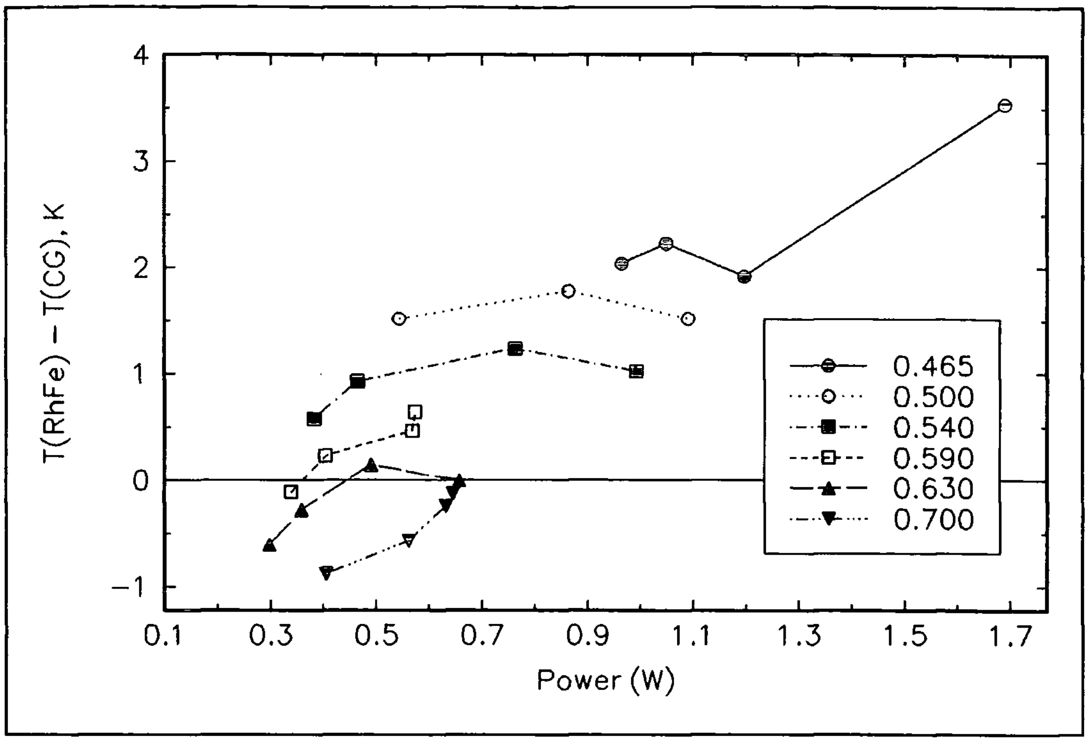

Figure 5.23 Temperature differences at 20K as a function of heater power at fixed ratios of heater current in low pressure helium gas.

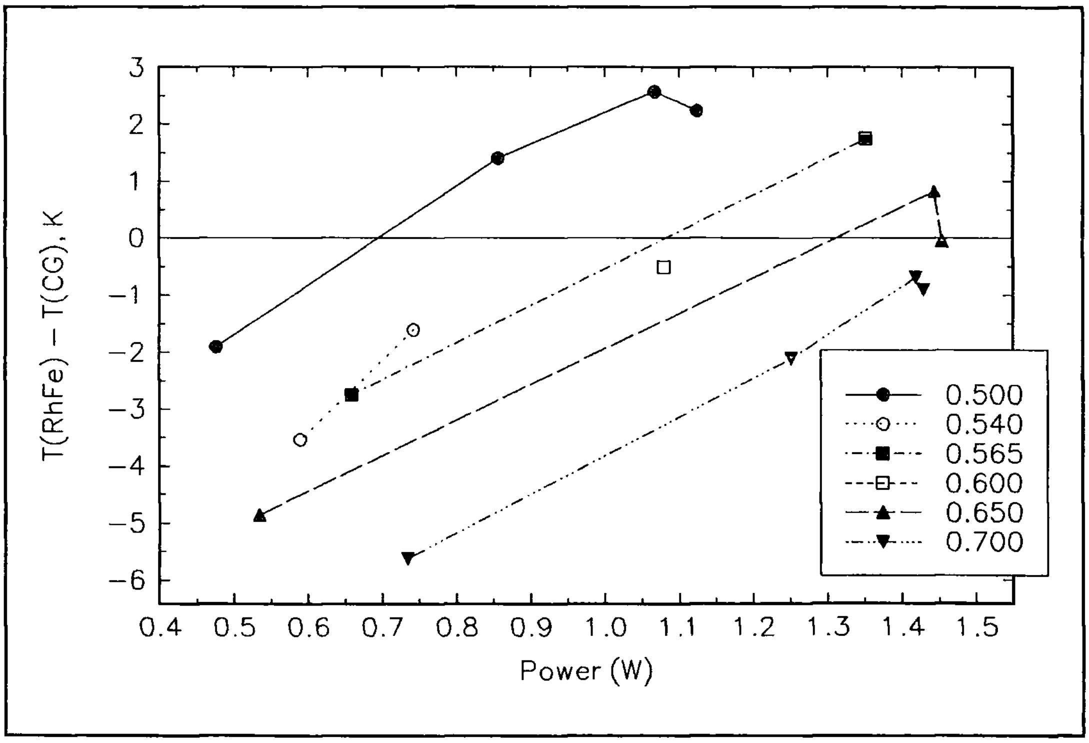

Figure 5.24 Temperature differences at 40K as a function of heater power at fixed ratios of heater current in low pressure helium gas.

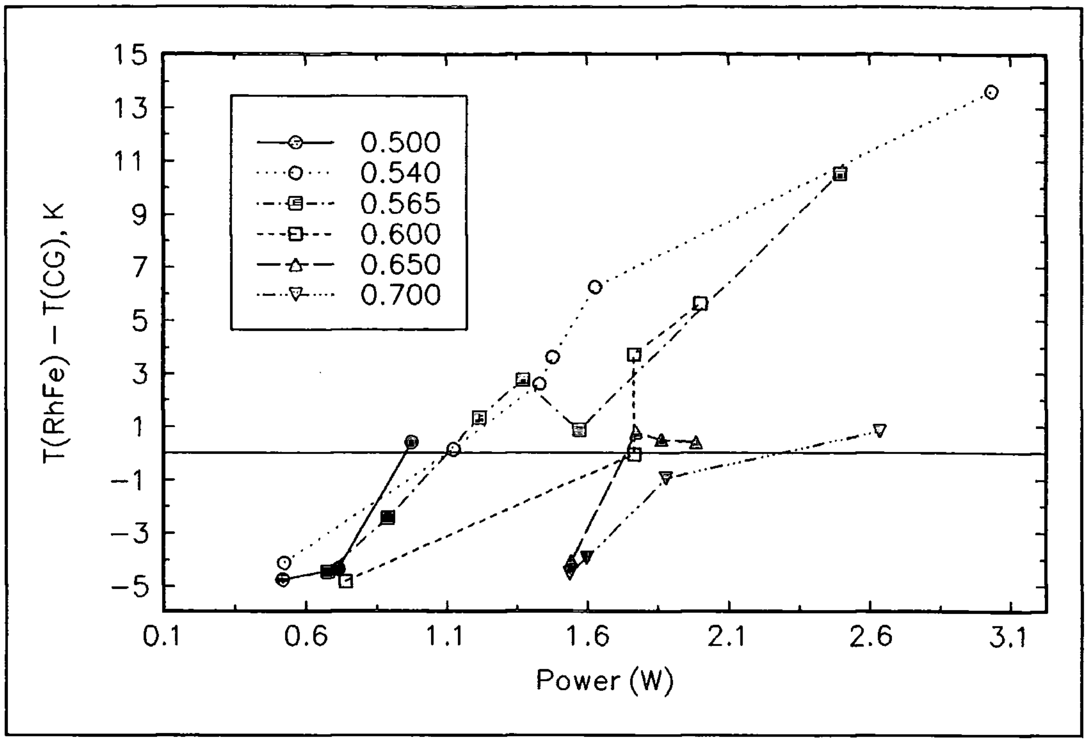

Figure 5.25 Temperature differences at 60K as a function of heater power at fixed ratios of heater current in low pressure helium gas.

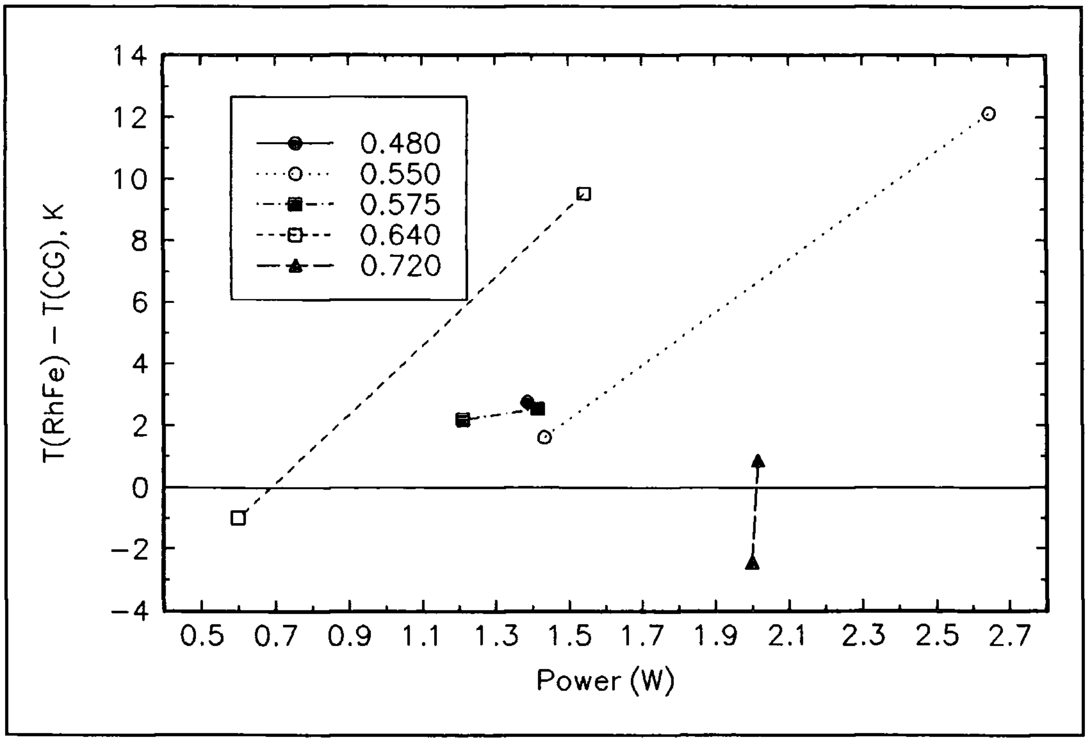

Figure 5.26 Temperature differences at 80K as a function of heater power at fixed ratios of heater current in low pressure helium gas.

Above 40K better control over the conditions in the system is needed. The temperature difference above 40K need not only to be made less dependent upon power, but be as systematic as those below 40K.

A series of experiments have been performed with the helium gas atmosphere within the probe being held at 50mTorr by the Pressure Controller. The choice of pressure was constrained by the need to have the pressure low enough to keep liquid helium boil-off acceptable and enough helium gas present to ensure good thermal contact between heater and sample along with good control of the temperature. Again temperature difference was measured as a function of heater power at fixed ratios of heater current. The results are presented in figures 5.27-5.32.

From figures 5.27 and 5.28 it is seen that the 20K and 40K data are not as systematic as those taken with continuous pumping. At 60K and 80K (figures 5.29 and 5.30), while the temperature differences are much more systematic than in the continuously pumped system, they still have almost the same dependence on power ($\approx 6KW^{-1}$). The 100 and 120K (figures 5.31 and 5.32) data could be said to be random, and no useful trends can be extracted.

In summary, acceptable temperature differences cannot be systematically reproduced in a closed 20mm bore system in a liquid helium cryostat for the temperature range 40 to 120K.

Measuring the sample temperature each time the experiment is run is the only way of eradicating the problem of not having systematic temperature difference behaviour. To do this a temperature sensor has to be mounted on the sample or sample holder. As discussed earlier this has signal implications, but if magnetisation is strongly dependent upon temperature in the range of the measurement any VSM data would not be valid if the temperature is only known to an accuracy of ±2K, or worse.

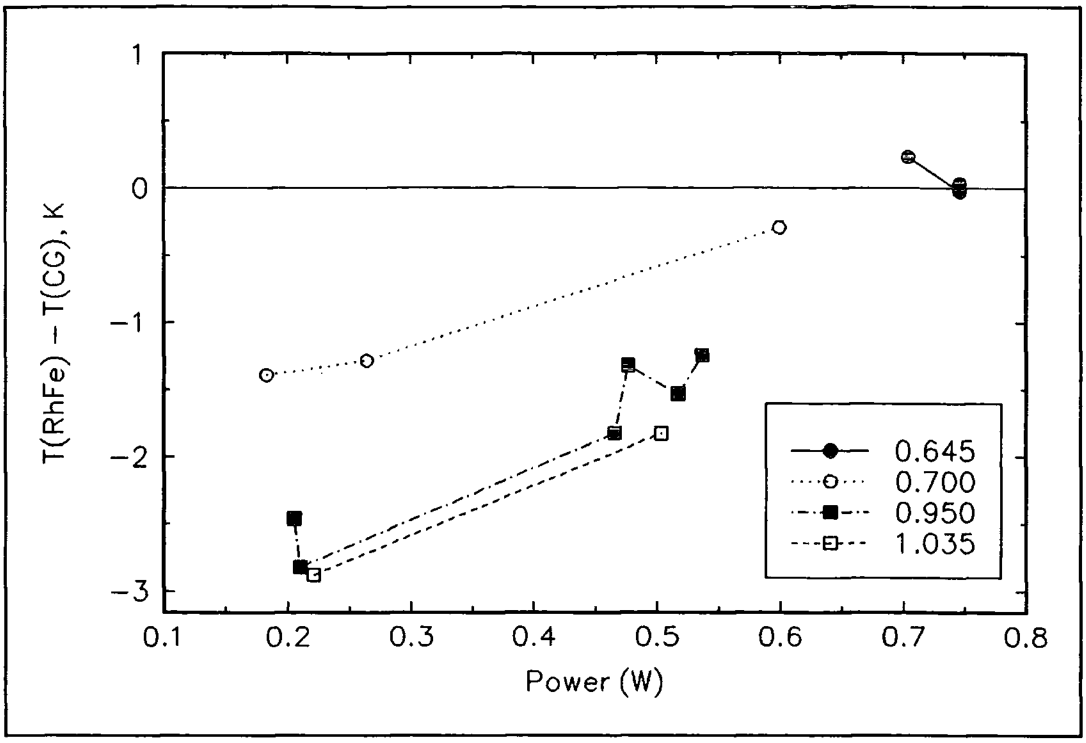

Figure 5.27 Temperature differences at 20K, 50mTorr as a function of heater power at fixed ratios of heater current.

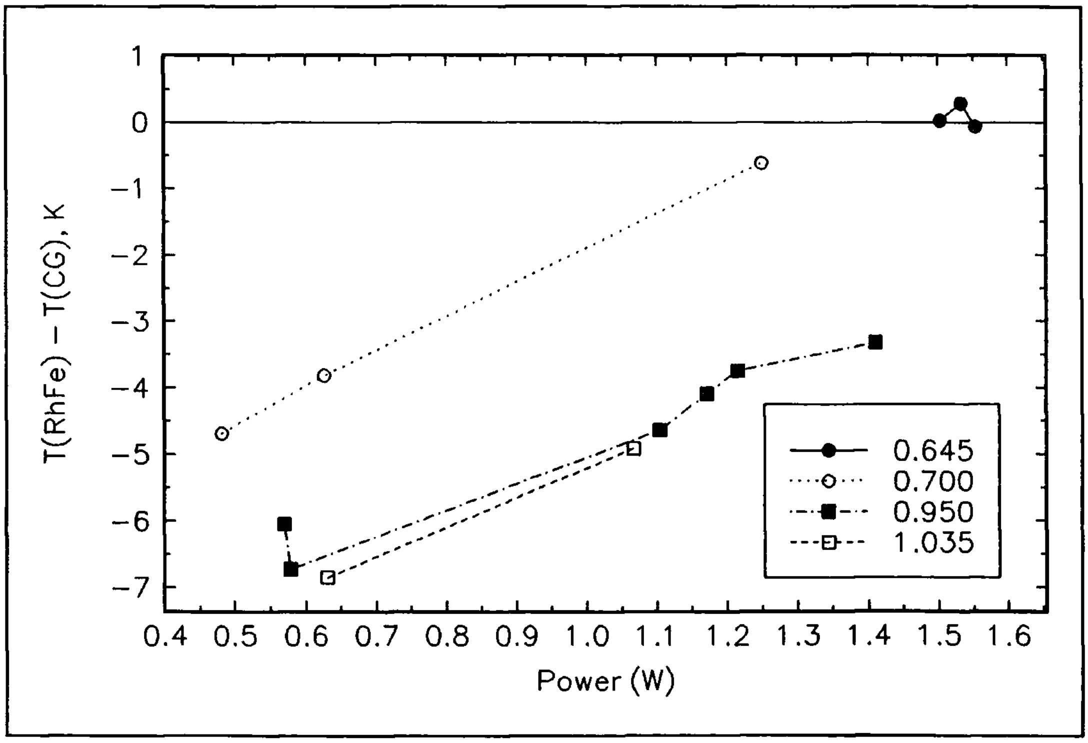

Figure 5.28 Temperature differences at 40K, 50mTorr as a function of heater power at fixed ratios of heater current.

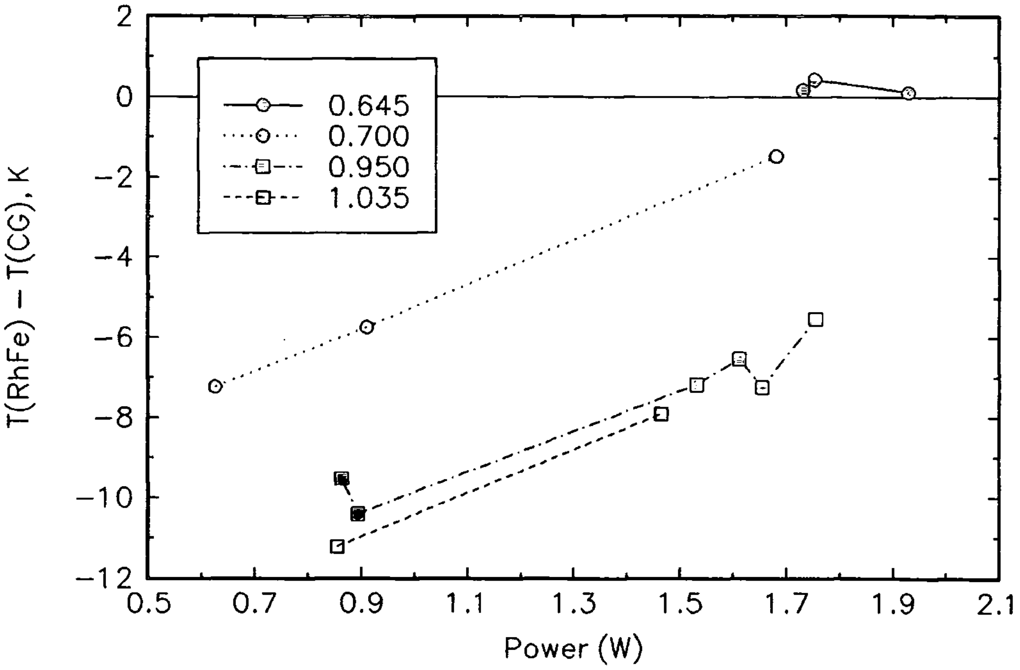

Figure 5.29 Temperature differences at 60K, 50mTorr as a function of heater power at fixed ratios of heater current.

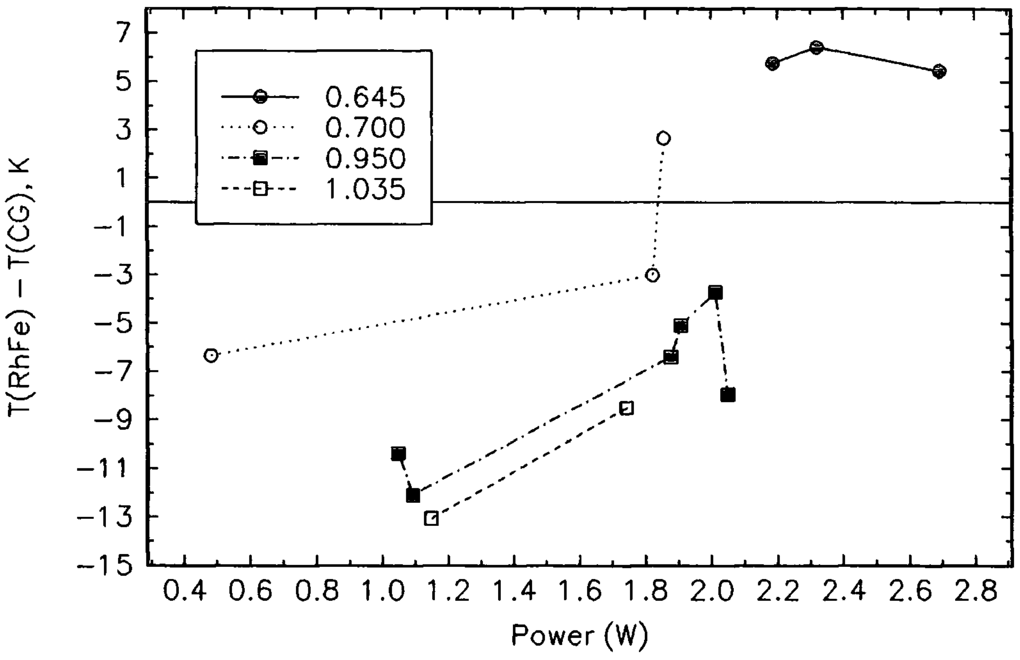

Figure 5.30 Temperature differences at 80K, 50mTorr as a function of heater power at fixed ratios of heater current.

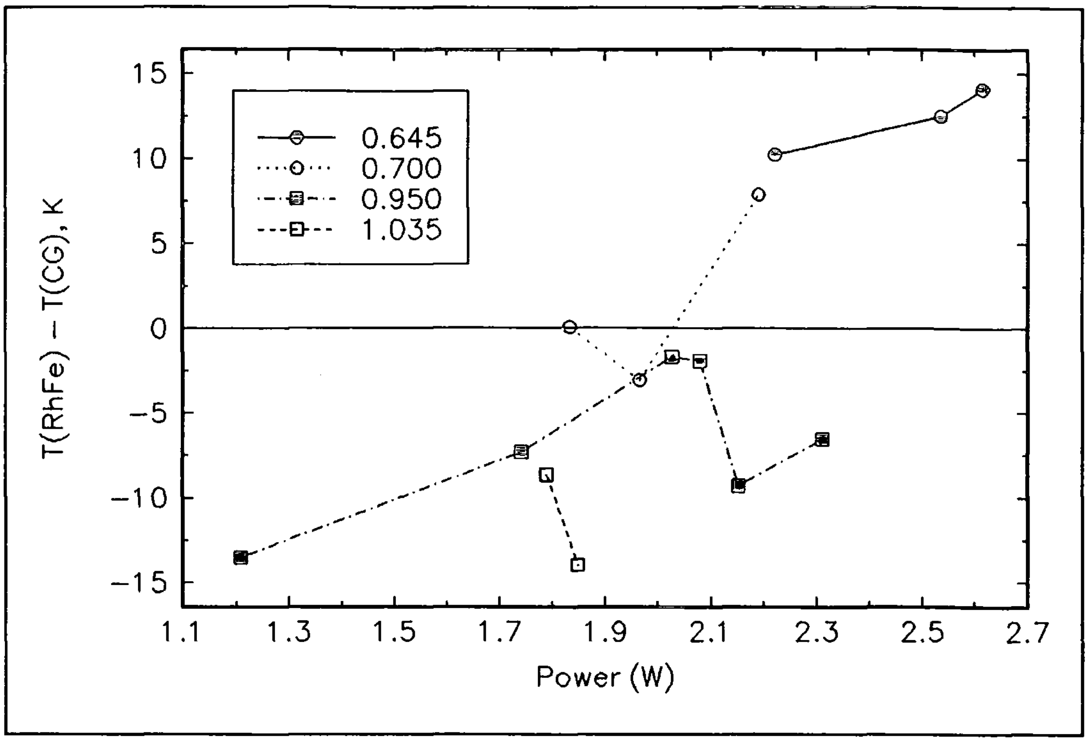

Figure 5.31 Temperature differences at 100K, 50mTorr as a function of heater power at fixed ratios of heater current.

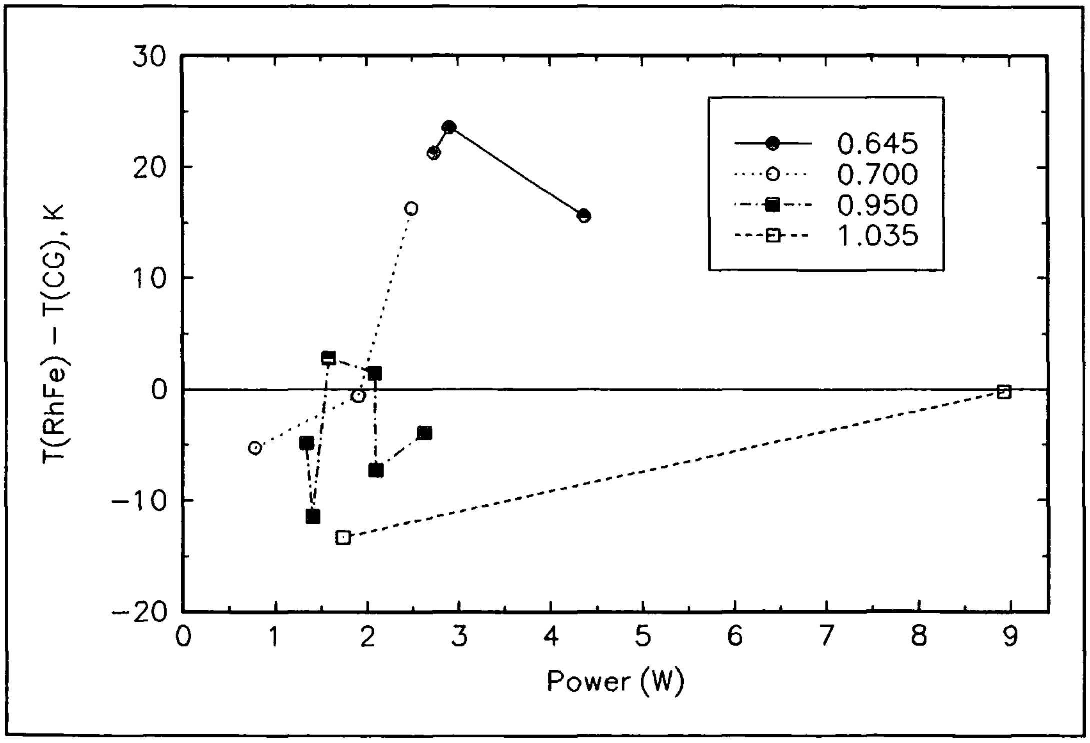

Figure 5.32 Temperature differences at 120K, 50mTorr as a function of heater power at fixed ratios of heater current.

5.4 Possible use of a Thermocouple to measure sample temperature.

It has been demonstrated in section 5.3.3 that it is very difficult to ensure reproducibly that the sample is at the same temperature as the sensor in the probe. Therefore it is necessary to measure directly the sample temperature. This may be done using a thermocouple.

The thermocouple works by generating a potential difference between two junctions at different temperatures. To use it to ensure that in this probe the sample temperature is equal to the temperature of the carbon glass sensor one junction should be placed on the sample, and the other in the silicone vacuum grease next to the carbon-glass sensor. When a voltmeter between the junctions registers zero volts then the two regions must be at the same temperature. This method avoids the need to calibrate the thermocouple.

There are a range of thermocouples on the market [5], and not all are suitable for this purpose. Some have low sensitivity at temperatures below 100K (e.g. chromel-CuFe and chromel-gold/iron). All thermocouples contain iron, chromium or nickel, all of which are ferromagnetic. Type T (copper-constantan) was chosen as it has good sensitivity below 100K and can be economically and easily manufactured.

The thermocouple will not be used in the VSM system, primarily because it would have been awkward to use without any breaks. Breaks would constitute extra junctions, introducing extra signal to the measurement.

5.5 Use of a Carbon-Glass Resistor to measure Sample temperature.

In order to measure the sample temperature directly, the need for which has been detailed in section 5.3.3, a carbon glass resistor has been mounted in a tufnol sample holder so it is in thermal contact with the sample. This has been done as the use of a carbon glass sensor is a simple four terminal resistance measurement. The measurement leads may be connected in sections using micro PCB connectors for ease of use when removing or inserting samples from the probe. The background signal of this has been measured as a function of magnetic field. A typical result is presented in figure 5.33.

Inspection of figure 5.33 shows a problem, i.e. a hysteretic background signal. This is a problem as the Bean model (see chapter 3) uses the hysteresis width to calculate the magnetisation critical current density, J_{cM}. As this background is reproducibly hysteretic it may easily be subtracted from any measurement.

In use the probe temperature is set and stabilised using the Lakeshore temperature controller. The sample sensor resistance (and hence temperature) is monitored using the DVM and current source. Then by use of the external variable resistor the ratio of current in the heaters is adjusted until the temperatures are the same. The DVM and current source are detached and the magnetisation measurement run.

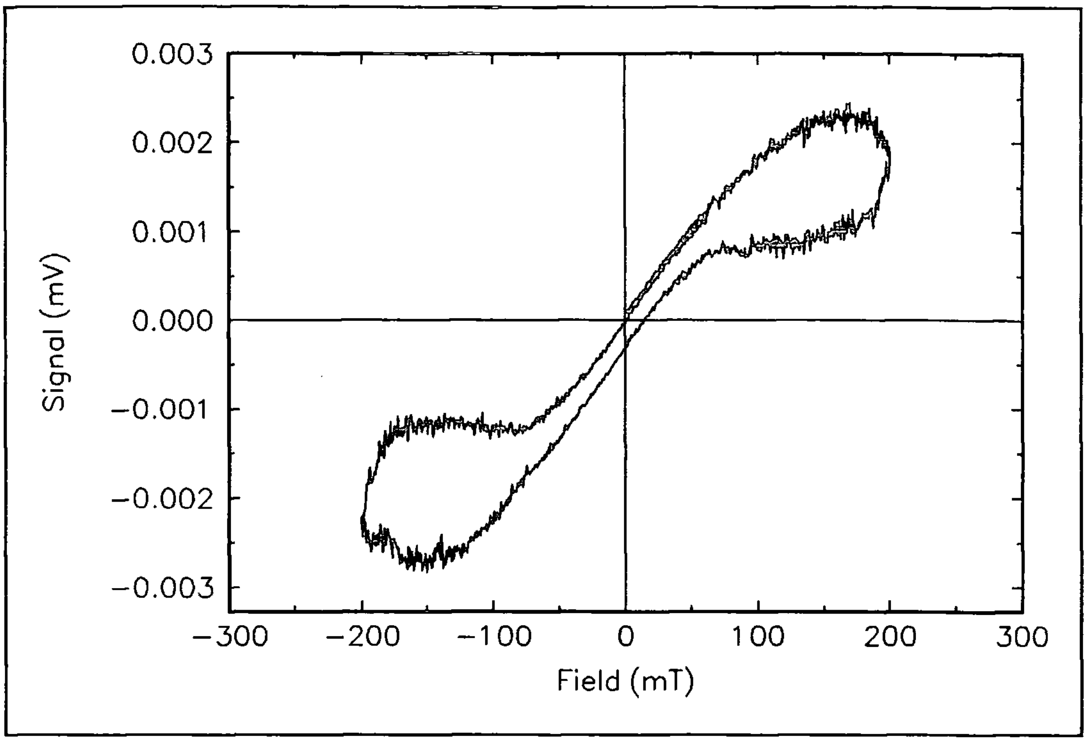

Figure 5.33 Signal of passive carbon-glass sensor at 77K.

5.6 Summary.

A system has been developed to make variable temperature VSM measurements on superconducting samples in a 20mm diameter closed bore. The VSM probe has been designed to keep the heat required to a minimum, saving on boil-off of the expensive liquid helium. Two temperature sensors are used, a carbon-glass sensor for accurate measurements in zero applied field and a capacitance sensor for control of the system in magnetic field. A specialist temperature controller is used for reading the sensors and providing the heating.

The problem of the sample and the sensor not being at the same temperature has been addressed. A method of working has been developed that will give temperature accurate to ±200mK when used from liquid nitrogen temperature (77K) up to 130K. This method has been successfully applied to the range 4.2K to 30K, where the same level of accuracy has been achieved. For experiments that require temperatures in the range 4.2K to 120K there is a problem. The dependence of the temperature difference between sample and sensor on power and ratio is not reliably reproducible. Therefore it has been necessary to develop a method for measuring the sample temperature directly to ensure that it is the same as the probe sensor temperature. This has been done using a second carbon-glass sensor.

5.7 References

[1] S.R. Hoon and S.N.M. Willcock "The design and operation of an automated double-crank vibrating sample magnetometer" *J.Phys.E* 21 (1988) 772.

[2] D-N. Zheng "An experimental study of flux pinning in high temperature superconductors" *PhD. Thesis* University of Cambridge, U.K. (1994).

[3] L.G. Rubin, B.L. Brandt and H.H. Sample "Cryogenic thermometry: a review of recent progress, II" *Cryogenics* (1982) 491.

[4] L.G. Rubin and W.N. Lawless "Studies of a Glass-Ceramic Capacitance Thermometer in an Intense Magnetic Field at Low Temperatures" *Rev.Sci.Instrum.* 42 (1971) 571.

[5] Lakeshore Cryotronics, Inc. "Lakeshore Product Catalogue and Reference Guide"

6. Low Field Magnetic Behaviour of Single Crystals of $YBa_2Cu_3O_{7-\delta}$.

6.1 Introduction.

In March 1987, $YBa_2Cu_3O_{7-\delta}$ was discovered to be the first superconductor with critical temperature, T_c, above the boiling point of liquid nitrogen [1]. The reported critical temperatures were between 80K and 93K and upper critical fields, $B_{c2}(0)$, between 80T and 180T were estimated by resistive extrapolation. These high values compared to those of Nb_3Sn, a commonly used high field superconductor with $T_c=18K$ and $B_{c2}(0)=22T$, should mean that the $YBa_2Cu_3O_{7-\delta}$ system has many possibilities for high field applications. Unfortunately, like the earlier lanthanum based compounds of Bednorz and Müller [2] these compounds are brittle ceramics, making fabrication of useful devices difficult. Granularity in $YBa_2Cu_3O_{7-\delta}$ can limit the current carrying capabilities of the material rendering it unsuitable for many applications.

The unit cell for $YBa_2Cu_3O_{7-\delta}$ has been determined by x-ray diffraction [3], and is shown in figure 6.1. This is an orthorhombic, perovskite type unit cell where some oxygen atoms have been removed from the structure. The lattice parameters are related in the following way:

$$a \simeq b \simeq \frac{c}{3}$$

Studies of the upper critical field in untwined crystals [5] suggest that there is little or no difference between the *a* and *b* directions. However the upper critical field along the *c* direction is very different. This anisotropic behaviour has also been seen in other electro-magnetic properties [6, 7, 8]. It is necessary to study the properties of high quality single crystals to probe the intrinsic behaviour of $YBa_2Cu_3O_{7-\delta}$.

Measurement of the magnetisation critical current density is important for single crystals of $YBa_2Cu_3O_{7-\delta}$ as it is very difficult to make transport measurements of the critical current density on such samples due to problems with making contacts to the sample.

This chapter describes low field magnetic measurements made with the VSM on two single crystals of the ceramic superconductor $YBa_2Cu_3O_{7-\delta}$. Firstly details of the manufacture of the samples at the National Crystal Growth Facility for Superconducting Oxides are presented before explanation of the experiments performed. These were studies of the magnetic hysteresis as a function of the sweep rate of the magnetic field and magnetic hysteresis as a function of temperature at and above 77K in magnetic fields up to 220mT. The data from these experiments is presented. The data has been analyzed using the critical state model and the magnetisation critical current density (J_{cM}) calculated. The implications of these results with reference to other work is discussed. A summary is given of the work that has been carried out.

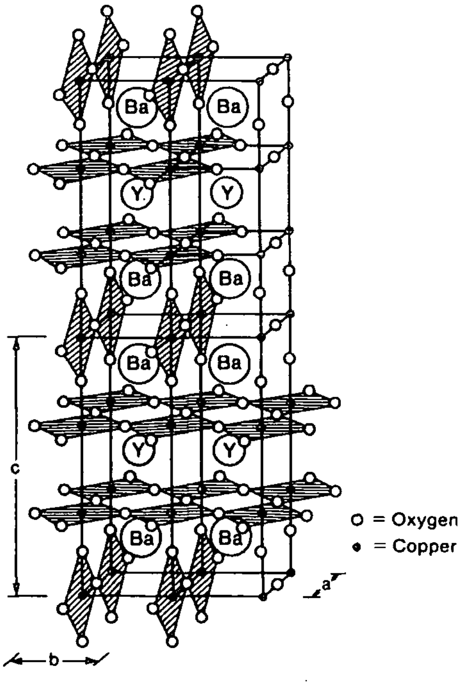

Figure 6.1 Unit cell of $YBa_2Cu_3O_{7-\delta}$ [4].

6.2 The Single Crystals.

The crystals used in this study were grown at the U.K. National Crystal Growth Facility for Superconducting Oxides, at the University of Birmingham. A mixed halide (NaCl/KCl) flux method was used [9], which can be summarised as follows: Powders of yttrium, barium and copper oxides were mixed in the appropriate molar ratios and reacted to make $YBa_2Cu_3O_{7-\delta}$ powder. This was then mixed with an amount of NaCl-KCl (50% by weight of each) flux. The mixture was placed in an alumina crucible and reacted in a muffle furnace to make single crystals which could be extracted from the melt. The samples were given a post growth annealing to ensure high oxygenation which increases T_c. The largest crystals grown to date are $8 \times 7 \times 2mm^3$. Their size depends on the amount of flux used and the heat treatment cycle.

Two crystals have been studied and their dimensions are summarised below in table 6.1. The c-axis is along the shortest dimension of each crystal.

Crystal	**Dimensions (mm^3)**
F21	4.4 x 4.0 x 1.5
F42	3.9 x 3.8 x 0.5

Table 6.1 Single Crystals used in low field measurements.

The samples have been confirmed as single crystals by Laue X-ray diffraction at Birmingham. The two crystals were grown with identical conditions such as heat treatment and amount of flux used, but not necessarily at the same time. Therefore they should have nominally identical electromagnetic properties.

6.3 Experimental Measurements.

The measurements of magnetic hysteresis have been made using the low field vibrating sample magnetometer as described in chapters 4 and 5. Two studies have been carried out, the dependence of magnetic hysteresis on the field sweep rate and the dependence of the magnetic hysteresis on the temperature.

6.3.1 Magnetic Hysteresis as a Function of Field Sweep Rate.

As has been shown in chapter 3 the magnetisation of a superconducting sample depends on the sweep rate of the applied field. Sample F21 has been measured at three sweep rates, 0.25, 0.5 and 0.9 mT.s^{-1}, at 77K with field perpendicular to the c-axis. The upper sweep rate limit was defined by the Oxford power supply, the lower by time constraints. The hysteresis loops are presented in figure 6.2. It can be seen that the faster the sweep rate, the greater is the hysteresis.

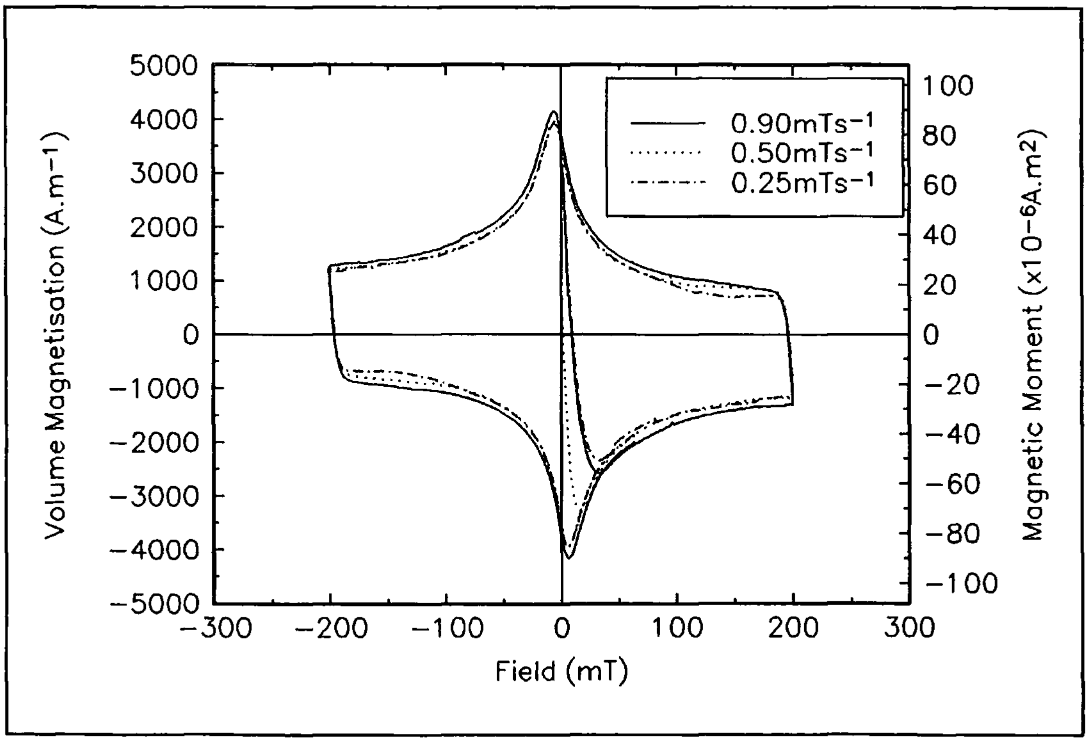

Figure 6.2 Effects of field sweep rate on hysteresis loops at 77K. Sample is YBa$_2$Cu$_3$O$_{7-\delta}$ single crystal F21 with B⊥c.

6.3.2 Magnetic Hysteresis as a Function of Temperature.

Magnetic hysteresis has been measured for both samples at 77, 80, 85, 90 and 95K, in fields up to 220mT. All of these measurements were made with a field sweep rate of $0.5mT.s^{-1}$ so that valid comparisons could be made between the data sets taken. This exercise was performed for both samples in two orientations, namely with the applied magnetic field perpendicular to the c-axis of the crystal, and with the applied magnetic field parallel to the c-axis of the crystal. Following the discussion in section 6.1 different results were expected.

The hysteresis measurements are presented as volume magnetisation and magnetic moment against applied magnetic field in figures 6.3-6.6. Volume magnetisation is the correct way to compare and contrast the data as the samples are not the same size.

Figure 6.3 shows magnetic hysteresis data for sample F21 with applied field parallel to the c-axis. The magnetic hysteresis decreases for increasing temperature at all fields, with no magnetic hysteresis observed at 95K. At 77K the magnetic hysteresis (ΔM) decreases from $\Delta M(0mT)=25000A.m^{-1}$ to $\Delta M(40mT)=20000A.m^{-1}$ after which the value of ΔM is approximately field independent. Similar behaviour at lower values of ΔM is observed at all other temperatures.

The data taken for the orientation of sample F21 where applied field is perpendicular to the c-axis is presented in figure 6.4. As in figure 6.3 the magnetic hysteresis decreases for increasing temperature at all fields and no magnetic hysteresis was observed at 95K. The magnetic hysteresis decreases at all fields and temperatures with no plateau seen. The peak value of the magnetic hysteresis at 77K is $\Delta M(0mT)=8000A.m^{-1}$.

Magnetic hysteresis of sample F42 with the applied field parallel to the c-axis is presented in figure 6.5. Again as temperature is increased at a particular field the magnetic hysteresis decreases. No hysteresis is observed at 90K and above. Magnetic hysteresis decreases from $\Delta M(0mT) = 35000 A.m^{-1}$ to $\Delta M(60mT) = 25000 A.m^{-1}$ at 77K and then remains steady until it increases at fields above 100mT. Similar behaviour at lower values of ΔM is observed at 80K. The 85K data does not show this rise in either quadrant where field magnitude is increasing. In the field magnitude decreasing quadrants at 85K magnetisation increases rapidly from ±180mT to ±120mT, and then remains constant down to ±40mT. Two spikes are observed in each negative field quadrant. These have been attributed to random noise in the system from an unknown source.

Figure 6.6 presents magnetic hysteresis of sample F42 with the applied field perpendicular to the c-axis. No magnetic hysteresis was observed at 90K. Generally, an increase in temperature corresponds to a decrease in magnetic hysteresis, except at fields below ±40mT where the 80K magnetic hysteresis is slightly larger than that at 77K. The values of magnetic hysteresis decrease with increasing field magnitude, although much faster at low field magnitudes. The spikes observed in the 77K and 80K data in the negative field increasing quadrant were accredited to unknown external noise sources.

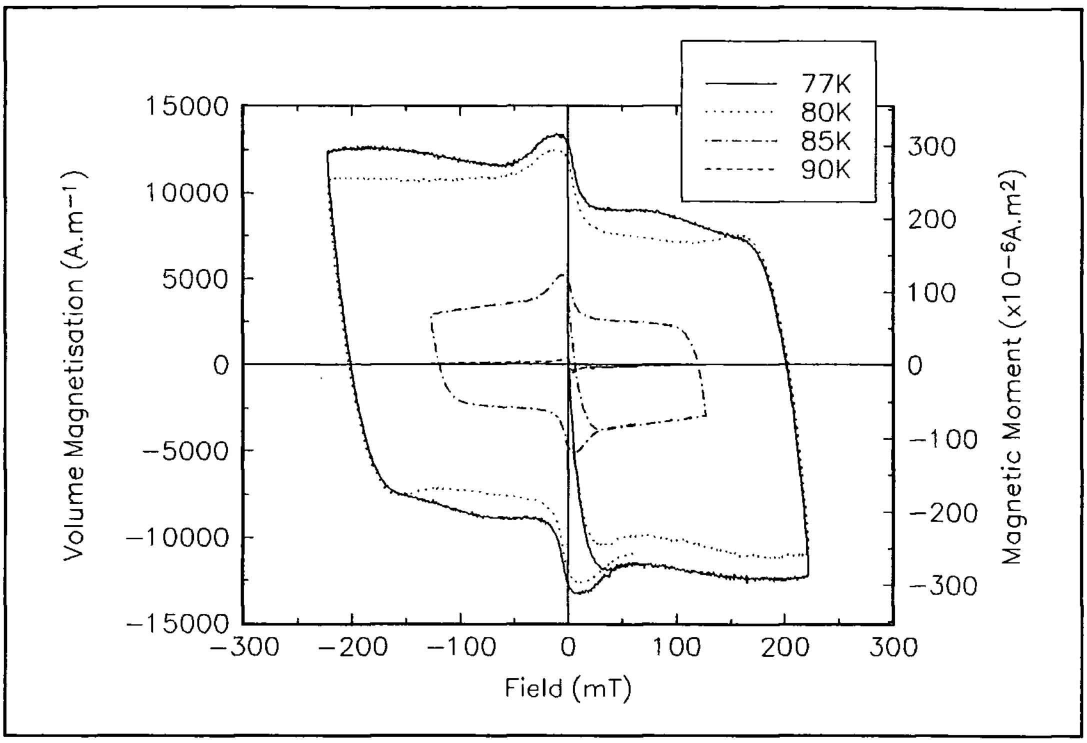

Figure 6.3 M(B) data for sample F21 from 77K to T_c with applied field parallel to the c-axis of the crystal.

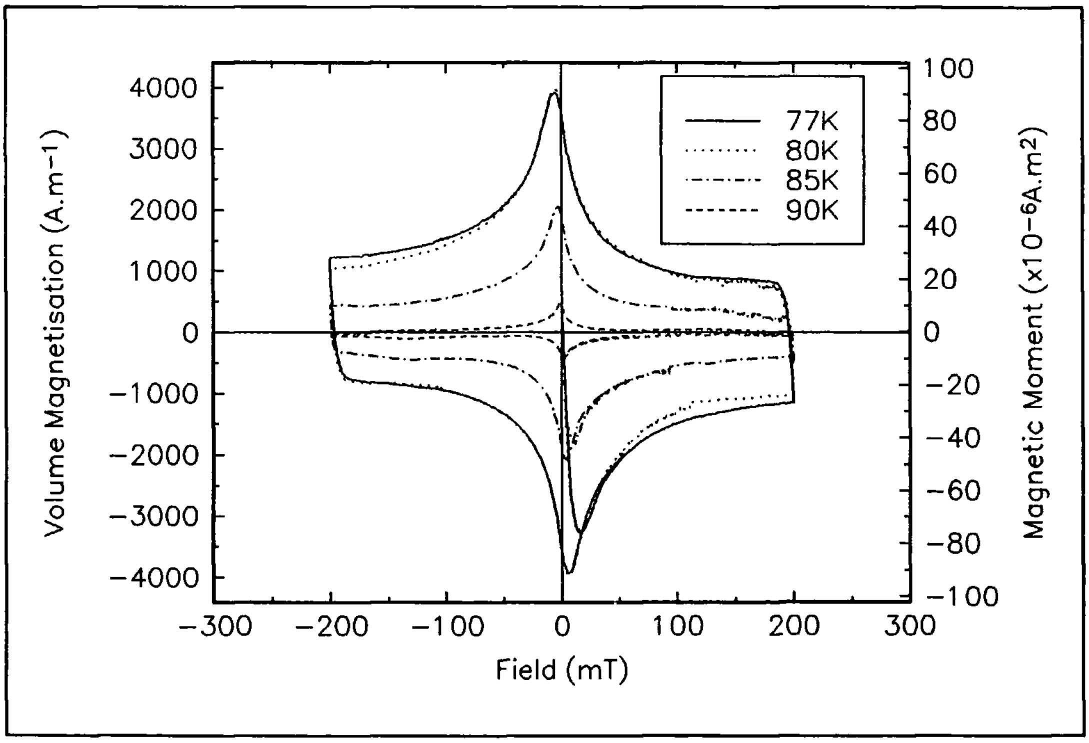

Figure 6.4 M(B) data for sample F21 from 77K to T_c with applied field perpendicular to the c-axis of the crystal.

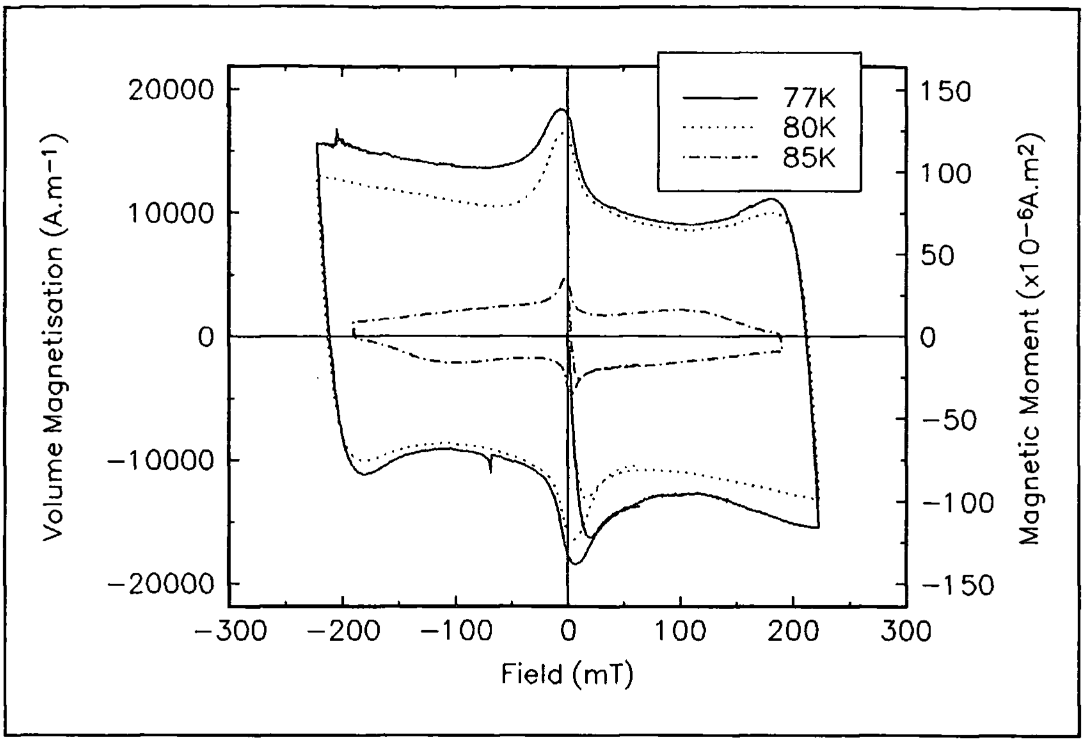

Figure 6.5 M(B) data for sample F42 from 77K to T_c with applied field parallel to the c-axis of the crystal.

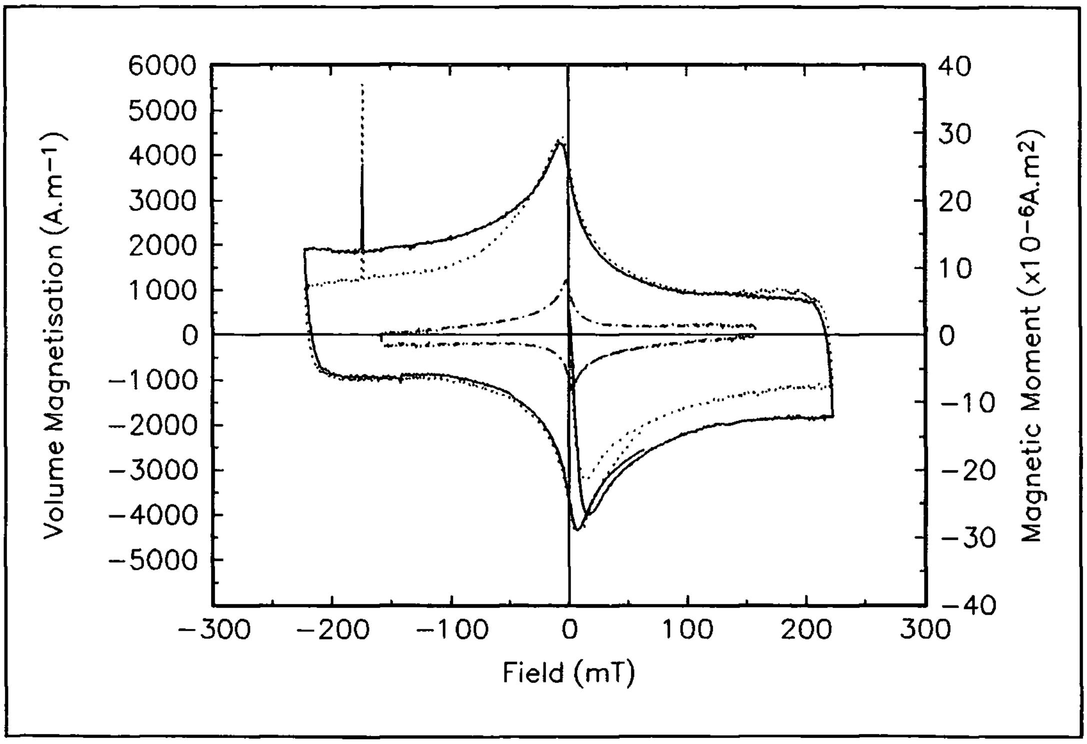

Figure 6.6 M(B) data for sample F42 from 77K to T_c with applied field perpendicular to the c-axis of the crystal.

6.4 Magnetisation Critical Current Density (J_{cM}).

Using the critical state model [10] (see chapter 3) magnetisation critical current densities have been calculated for both samples in both orientations from the magnetic hysteresis curves that were presented in section 6.3. The hysteretic background of the carbon glass thermometer mounted on the sample is accounted for as detailed in section 5.7. Recall from the critical state model:

$$J_{cM} = \frac{\Delta M}{a}$$

A suitable choice has to be made for the value of a, the appropriate length scale for the flow of current.

This will be different in each crystallographic direction. From an analysis by Peterson [11], for applied field perpendicular to the c-axis:

$$a = \frac{1}{2} l_1 \left(1 - \frac{l_1}{3 l_2} \right)$$

where l_1 and l_2 are the dimensions of the sample perpendicular to the applied field and $l_1 > l_2$. If the applied field is parallel to the c-axis of the crystal then [12]:

$$a = \frac{d}{3}$$

where d is a geometric mean of the sample dimensions perpendicular to the applied field. This analysis may only be applied if the applied field is greater than the self field. In this case if B > 20mT then the condition is fulfilled.

6.4.1 Magnetisation Critical Current Density as a Function of Field Sweep Rate.

The results of the analysis of the data taken in section 6.3.1 on sample F21 at 77K are shown in figure 6.5. At all values of applied field the magnetisation critical current density increases linearly for increasing sweep rate. Increasing the sweep rate by 350% causes an approximate increase in the magnetisation critical current density of 8% at all fields. As the applied field is increased at a fixed sweep rate the magnetisation critical current density decreases.

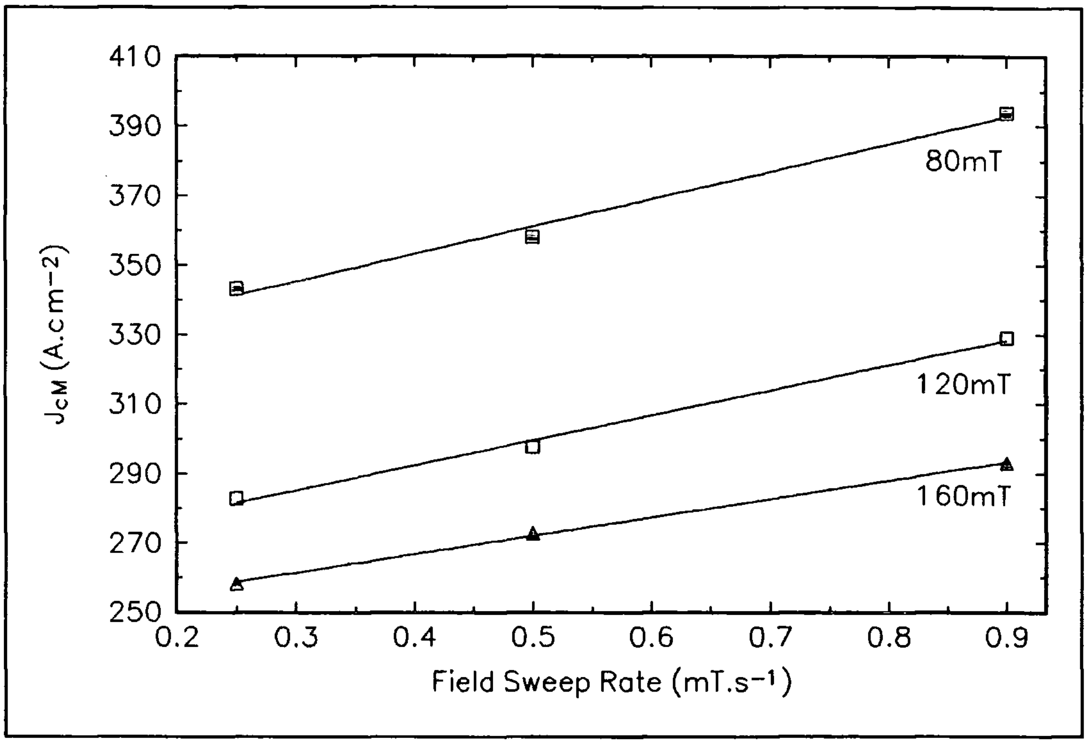

Figure 6.7 Dependence of J_{cM} values on magnetic field sweep rate for $YBa_2Cu_3O_{7-\delta}$ single crystal F21 at 77K with B⊥c.

6.4.2 Magnetisation Critical Current Density as a Function of Temperature.

All the variable temperature data taken in section 6.3.2 has been analysed within the critical state model and the results are presented in figures 6.8-6.11.

The analysis for sample F21 is shown in figure 6.8 for applied field parallel to the c-axis and figure 6.9 for applied field perpendicular to the c-axis. When the field is orientated parallel to the c-axis of the crystal the magnetisation critical current density is almost independent of applied field over the range 40mT to 160mT at all temperatures. The data at 80K may have a small local minimum at 100mT, but this feature is not identifiable at any other temperature, and is not believed significant. As the temperature is increased the magnetisation critical current density decreases at all fields. For applied field perpendicular to the c-axis the magnetisation critical current density is a very strong function of applied field at low fields ($B < 100$mT), but not as strongly at higher fields for all temperatures. The curves all have the same basic shape. No local minima are observed. As with the other orientation if the temperature is increased at fixed applied field the magnetisation critical current density decreases.

Comparing the two orientations of sample F21 the dependencies of magnetisation critical current density are different. At 77K and 80K higher magnetisation critical current densities are observed with the applied field perpendicular to the c-axis orientation below 80mT, whereas above 80mT the applied field parallel to the c-axis orientation has higher magnetisation critical current densities. The values of the magnetisation critical current density are similar for both orientations at 85K and 90K.

Figures 6.10 and 6.11 present the analysis of sample F42 for applied fields parallel and perpendicular to the c-axis respectively. In figure 6.10 it is seen that magnetisation critical current density decreases rapidly at all temperatures for fields up to 80mT. Above this however the data at 77K and 80K start to increase again at higher fields, and are still increasing at the highest field. The 85K data approaches current density decreases. When the applied field is perpendicular to the c-axis at all temperatures there is a sharp decrease in the magnetisation critical current density up to 100mT, but then there is no increase just a slower decrease. Below 40mT the values of magnetisation critical current density are slightly higher at 80K than at 77K. Above 40mT if the temperature is increased the magnetisation critical current density decreases, as has been observed in all other data.

Comparing the two orientations for sample F42, the magnetisation critical current densities are higher for field applied perpendicular to the c-axis than for applied field parallel to the c-axis at all temperatures.

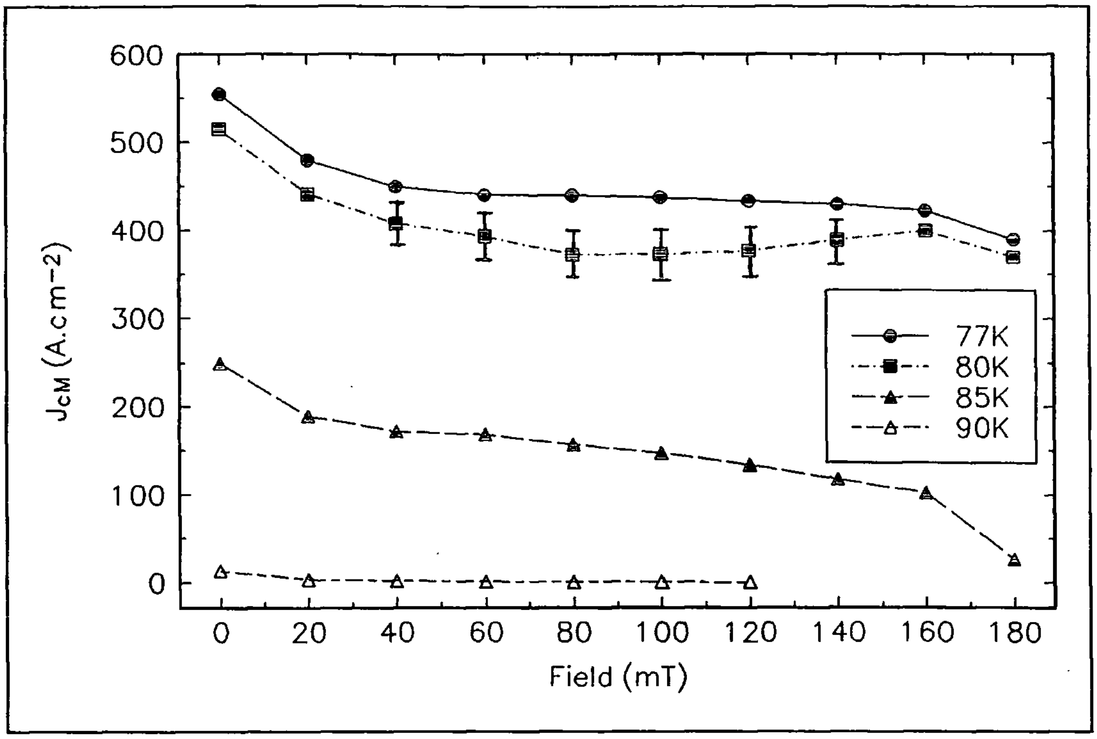

Figure 6.8 J_{cM} data for sample F21 from 77K to T_c with applied field parallel to the c-axis of the crystal.

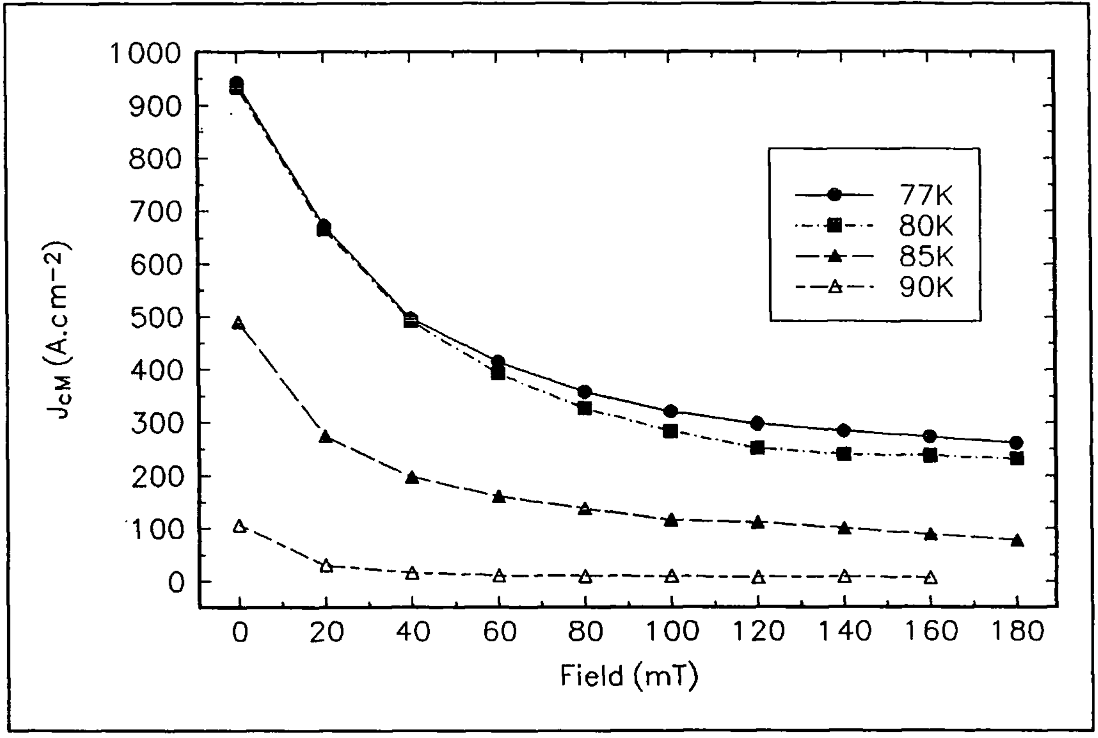

Figure 6.9 J_{cM} for sample F21 from 77K to T_c with applied field perpendicular to the c-axis of the crystal.

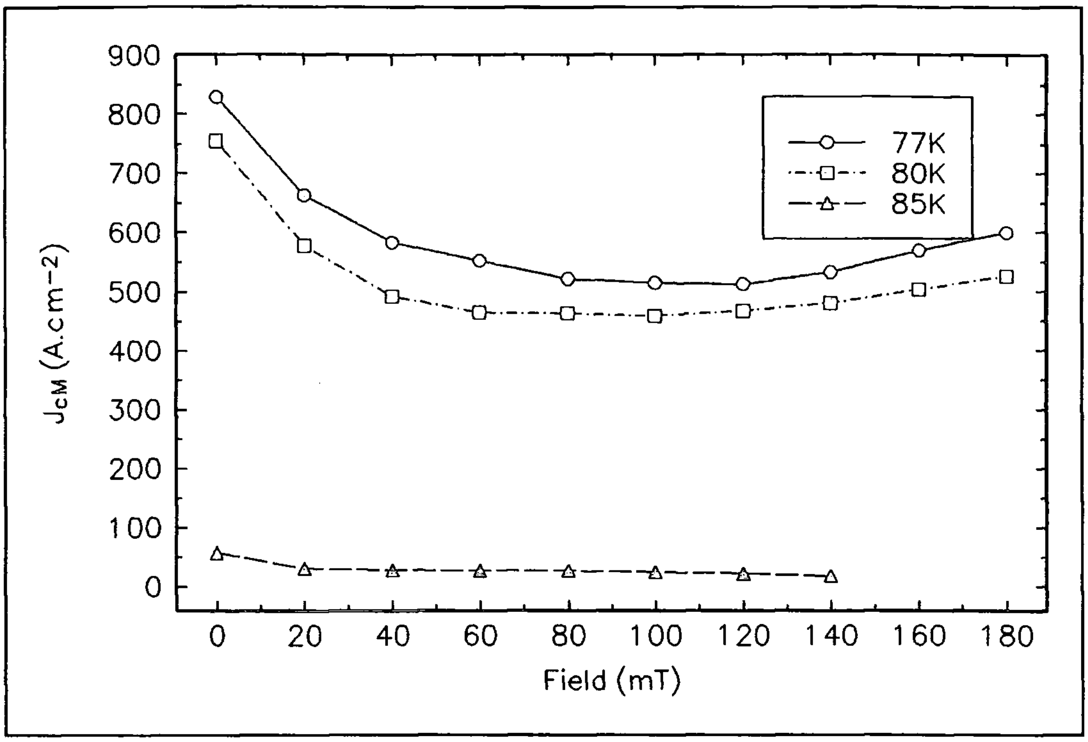

Figure 6.10 J_{cM} for sample F42 from 77K to T_c with applied field parallel to the c-axis of the crystal.

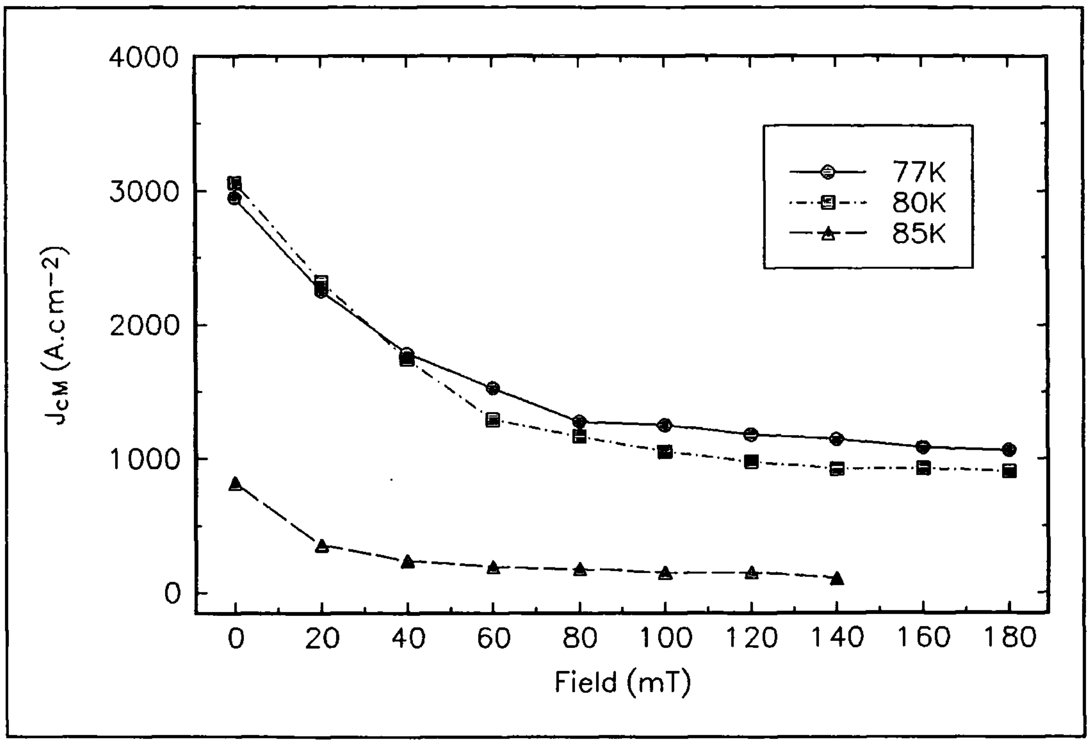

Figure 6.11 J_{cM} for sample F42 from 77K to T_c with applied field perpendicular to the c-axis of the crystal.

6.5 Discussion.

While the two crystals have been manufactured under nominally identical conditions, it is easily seen through the difference in transition temperature that their superconducting properties are not identical. Sample F21 shows small hysteresis at 90K, which has disappeared at 95K as seen in figures 6.5 and 6.6. However figures 6.7 and 6.8 show that sample F42 displays no hysteresis at 90K, independent of orientation to the magnetic field.

The work on magnetic hysteresis as a function of magnetic field sweep rate agrees with similar data taken by Caplin et.al [12]. The effects of flux creep in the sample are more pronounced at lower field sweep rates and cause the observed magnetic moment to be lower at lower magnetic field sweep rates. Magnetisation critical current densities deduced for sample F21 show that the critical current density is defined by the sweep rate. Caplin and co-workers point out that "critical current" is an arbitrary choice and that in general a three dimensional E-J-B surface is mapped out. While they are correct, plots of J-B are valid for comparison provided that the magnetic field sweep rate is identical in all the traces that are to be compared. In order that the variable temperature measurements made on the crystals could be properly compared they were all made at a magnetic field sweep rate of $0.5mT.s^{-1}$. Plots of the derived critical current density against the sweep rate (or effective voltage criteria) may be used to construct a "V-I" trace at constant applied field, similar to those taken in transport current measurements. A good example is in work by Oussena et.al [13] on single crystals of $Tl_2Ba_2CaCu_2O_8$ and $Bi_2Sr_2CaCu_2O_8$. To construct Oussena's traces magnetic field sweep rates of up to $20mT.s^{-1}$ were used, much higher than those used here. This type of analysis can be applied to the data in figure 6.7, but not much information may be gained as the relationship between magnetisation critical current density and magnetic field sweep rate is simply linear within the range measured.

It may be seen from the variable temperature magnetic hysteresis work that for both samples the volume magnetisation is larger for field parallel to the c-axis (figures

6.3 and 6.5) than for field perpendicular to the c-axis (figures 6.4 and 6.6) by a factor of approximately 3-4. This agrees with the data taken on similar crystals of $YBa_2Cu_3O_{7-\delta}$ by Yang et.al [14] within the range studied. At 77K Yang's crystal shows a minimum in magnetic hysteresis when applied field is parallel to the c-axis, as has been seen here in sample F42. This effect has been widely reported in $YBa_2Cu_3O_{7-\delta}$ [15 ,16, 17], and also in $Bi_2Sr_2CaCu_2O_y$ [17].

Values of volume magnetisation for the samples studied are typically in the range of $10^3A.m^{-1}$ and $10^4A.m^{-1}$ for applied field perpendicular and parallel to the applied field respectfully at 77K. This compares to $10^4A.m^{-1}$ and $10^5A.m^{-1}$ quoted for the crystal of Yang [14]. This difference could be accounted for by a difference in the magnetic field sweep rate (as detailed above), unfortunately it is not quoted by Yang and co-workers.

Magnetic hysteresis curves taken at low fields on polycrystalline samples of $YBa_2Cu_3O_{7-\delta}$ [18] also display a local minimum in magnetisation as a function of applied field. The magnetisation of this polycrystalline sample was approximately $10^3A.m^{-1}$ at a temperature of 82K.

Values of the magnetisation critical current density were derived using the critical state model from the variable temperature magnetic hysteresis data. Firstly considering the orientation where applied magnetic field is perpendicular to the c-axis of the crystal it is seen that the magnetisation critical current density falls asymptotically at all temperatures. The highest value of magnetisation critical current density at 77K for sample F21 was nearly $1000A.cm^{-2}$ and for sample F42 was $3000A.cm^{-2}$.

The orientation of applied magnetic field parallel to the c-axis of the crystal is that most studied as the anomalous magnetisation effects happen in this orientation (see above). At 77K the magnetisation critical current densities for the samples measured were between $400A.cm^{-2}$ and $900A.cm^{-2}$. Rough comparisons may be made with other workers as their data usually covers much greater ranges of applied field.

Data taken by Däumling et.al [17] in 1990 shows single crystals of $YBa_2Cu_3O_{7-\delta}$ at 80K with magnetisation critical current densities of the order of $10^4 A.cm^{-2}$ in the low field region. In 1992 Ren et.al [15] measured the magnetisation critical current density in similar single crystals of $YBa_2Cu_3O_{7-\delta}$ at 80K to be of the order of $2\times10^3 A.cm^{-2}$.

Transport critical current density measurements on films of $YBa_2Cu_3O_{7-\delta}$ deposited by a pulsed laser technique at 75K [19] give critical currents densities in excess of $10^6 A.cm^{-2}$, much higher than that measured for single crystals. This could be due to a greater defect density within the film. Microstructure has been shown to be very effective in pinning in films of $YBa_2Cu_3O_{7-\delta}$ [22].

In polycrystalline $YBa_2Cu_3O_{7-\delta}$ there will be a very large number of defects and grain boundaries that may act as good pinning sites. Penn et.al [18] found magnetisation critical current densities of approximately $200A.cm^{-2}$ at 77K and fields below 25mT. Transport critical current measurements on samples of aligned polycrystalline $YBa_2Cu_3O_{7-\delta}$ give values for critical current measured along the a,b plane (so it is analogous to a magnetisation critical current density with applied field parallel to the c-axis) of $100A.cm^{-2}$ at 77K and a field of 0.1T [20]. These values of critical current density are similar to those found in a similar system studied by Nakagawa and co-workers [21]. While there are many potential pinning sites in the polycrystalline material their low values of critical current density suggest other problems.

Magnetisation critical current densities along the c-axis, i.e. those here measured with magnetic field perpendicular to the c-axis, while higher than those within the a-b plane, i.e with magnetic field parallel to the c-axis, are not in general measured by other workers.

The difference between the values of magnetisation critical current density in the crystals measured here and others quoted in literature could be due to one or both of the following effects:

(i) Different magnetic field sweep rates being used in the measurements. Neither of the groups measuring single crystals quote the magnetic field sweep rate for their measurements.

(ii) Improvements in crystal quality. As the science of growing crystals of $YBa_2Cu_3O_{7-\delta}$ improves, the density of defects and dislocations within the crystal decreases. This means that there are fewer potential pinning sites available, leading to a lower critical current density.

The first reason cannot be properly tested here, but data from crystals of $Tl_2Ba_2CaCu_2O_8$ and $Bi_2Sr_2CaCu_2O_8$ [13] suggest that these effects may make only a factor of two or three difference to the magnetisation critical current density, and not an order of magnitude. The second explanation may be more attractive and its validity may be probed by looking at results obtained for the critical current density of other forms of $YBa_2Cu_3O_{7-\delta}$. The thin film data supports this suggestion as the higher critical current density may be attributed to more potential pinning sites, whereas data from polycrystalline samples would seem to suggest otherwise.

6.6 Summary.

Magnetic hysteresis measurements have been made on two single crystals of $YBa_2Cu_3O_{7-\delta}$ prepared under identical conditions at the U.K National Crystal Growth Facility for Superconducting Oxides at the University of Birmingham.

The first part of the study looked at the effect of magnetic field sweep rate on the magnetic hysteresis of a sample. One of the samples was measured at 77K with the applied field perpendicular to the c-axis, at three magnetic field sweep rates. Analysis of the data showed that the measured magnetisation critical current density increases for increasing magnetic field sweep rate. In order that valid comparisons of the data taken on subsequent runs could be made they were all performed at a unique magnetic field sweep rate of $0.5mT.s^{-1}$.

Both crystals were measured at variable temperatures with the field parallel and perpendicular to the c-axis. Volume magnetisation was shown to be higher in both samples for applied field parallel to the c-axis. The two crystals were shown to have different transition temperatures and therefore are not identical as their manufacture route would suggest. The field dependence of the volume magnetisation was very different for applied field parallel or perpendicular to the c-axis. Some evidence of the widely reported local minimum in magnetisation as a function of field is seen in one of the crystals.

Magnetisation critical currents have been derived from the magnetic hysteresis data in accordance with the critical state model. For applied field perpendicular to the c-axis they are of the order of a few $10^3A.cm^{-2}$. When the magnetic field is applied parallel to the c-axis the magnetisation critical current densities are all below $10^3A.cm^{-2}$, lower than any values at similar temperatures and fields that were found. This may be due to improved crystal quality. The magnetisation critical current densities also showed that the crystals did not have the same superconducting properties.

6.7 References.

[1] M.K. Wu, J.R. Ashburn, C.J. Torng, P.H. Hor, R.L. Meng, L. Gao, Z.J. Huang, Y.Q. Wang and C.W. Chu "Superconductivity at 93K in a New Mixed-Phase Y-Ba-Cu-O Compound System at Ambient Pressure" *Phys.Rev.Lett.* **58** (1987) 908.

[2] J.G. Bednorz and K.A. Müller "Possible High T_c Superconductivity in the Ba-La-Cu-O System" *Z.Phys.B.* **64** (1986) 189.

[3] B.W. Veal, W.K. Kwok, A. Umezawa, G.W. Crabtree, J.D. Jorgensen, J.W. Downey, L.J. Nowicki, A.W. Mitchell, A.P. Paulikas and C.H. Sowers "Superconductivity in $YBa_{2-x}Sr_xCu_3O_{7-\delta}$" *Appl.Phys.Lett.* **51** (1987) 279.

[4] J.C. Phillips "Physics of High-T_c Superconductors" *Academic Press* (1989)

[5] U.Welp, M. Grimsditch, H. You, W.K. Kwok, M.M. Fang, G.W. Crabtree J.Z. Liu "The Upper Critical Field of Untwined $YBa_2Cu_3O_{7-\delta}$ Crystals" *Physica.C.* **161** (1989) 1.

[6] T.R. McGuire, T.R. Dinger, P.J.P Freitas, W.J. Gallagher, T.S. Plaskett, R.L. Sandstrom and T.M. Shaw "Magnetic properties of Y-Ba-Cu-O superconductors" *Phys.Rev.B.* **36** (1987) 4032.

[7] U. Welp, W.K. Kwok, G.W. Crabtree, K.G. Vandervoort and J.Z. Liu "Magnetic Measurements of the Upper Critical Field of $YBa_2Cu_3O_{7-\delta}$ Single Crystals" *Phys.Rev.Lett.* **62** (1989) 1908.

[8] Y. Iye, T. Tamegai, H. Takeya, and H. Takei "Superconductive properties of single crystal $YBa_2Cu_3O_x$" *Physica.B.* **148** (1987) 224.

[9] F. Gencer and J.S. Abell "The growth of $YBa_2Cu_3O_{7-\delta}$ single crystals with the aid of a NaCl-KCl flux" *J.Cryst.Growth* **112** (1991) 337.

[10] C.P. Bean "Magnetisation of Hard Superconductors" *Rev.Mod.Phys.* **36** (1964) 31.

[11] R.L. Peterson "Magnetization of anisotropic superconducting grains" *J.Appl.Phys.* **67** (1990) 6930.

[12] A.D. Caplin, L.F. Cohen, G.K. Perkins and A.A. Zhukov "The electric field within high-temperature superconductors: mapping the E-J-B surface" *Supercond.Sci.Technol.* **7** (1994) 412.

[13] M.Oussena, S. Porter, A.V. Volkozub, P.A.J. de Groot, P.C. Lanchester, D. Ogborne, M.T. Weller, G. Balakrishnan and D.McK. Paul "Comparative study of pinning and creep in $Tl_2Ba_2CaCu_2O_8$ and $Bi_2Sr_2CaCu_2O_8$ single crystals" *Phys.Rev.B* 48 (1993) 10575.

[14] G. Yang, J.S. Abell and C.E.Gough "Anomalous magnetisation of YBCO and BSCCO single crystals" *IEEE.Trans.Appl.Supercon.* 3 (1993) 1671.

[15] Y. Ren, P.A.J. de Groot, F. Gencer and J.S. Abell "Field-dependence anomaly in critical currents and granularity for flux-grown single-crystal $YBa_2Cu_3O_{7-\delta}$" *Supercond.Sci.Technol.* 5 (1992) 349.

[16] L.F. Cohen, J.R. Laverty, G.K. Perkins, A.D. Caplin and W. Assmus "Fishtails, scales and magnetic fields" *Cryogenics* **33** (1993) 352.

[17] M. Däumling, J.M. Seuntjens and D.C. Larbalestier "Oxygen-defect flux pinning, anomalous magnetization and intra-grain granularity in $YBa_2Cu_3O_{7-\delta}$" *Nature* **346** (1990) 332.

[18] S.J. Penn, N.McN. Alford, T.W.Button and G.R. Court "The magnetic hysteresis of polycrystalline $YBa_2Cu_3O_x$" *IEEE.Trans.Appl.Supercon.* **3** (1993) 1157.

[19] S.R. Foltyn, P. Tiwari, R.C. Dye, M.Q. Le and X.D. Wu "Pulsed laser deposition of thick $YBa_2Cu_3O_{7-\delta}$ films with $J_c > 1MA/cm^2$" *Appl.Phys.Lett.* **63** (1993) 1848.

[20] J.W. Ekin, H.R. Hart Jr. and A.R. Gaddipati "Transport critical current of aligned polycrystalline $YBa_2Cu_3O_{7-\delta}$ and evidence for a nonweak-linked component of intergranular current conduction" *J.Appl.Phys.* **68** (1990) 2285.

[21] Y. Nakagawa, H. Yamasaki, M. Umeda and S.Kosaka "Transport critical currents in field-oriented $Y_1Ba_2Cu_3O_y$ polycrystals" *J.Appl.Phys.* 71 (1992) 800.

[22] D.A. Cardwell, A.R. Jones, N.J.C. Ingle, A.M.Campbell, N. McN. Alford, T.W. Button, S.J. Penn, F. Wellhofer and J.S. Abell "Magnetisation and Transport Critical Current Densities in Melt Processed $YBa_2Cu_3O_{7-\delta}$ Thick Films" *Applied Superconductivity vol.1 p.641.* ed. H.C.Freyhardt

7. High Field Magnetisation Measurements.

7.1 Introduction.

In order to characterise and understand the superconducting state it is necessary to study superconducting materials over as wide a range of applied magnetic field and temperature as possible. Analysis such as this is also vital for assessing the suitability of new materials for use in high magnetic field applications. Magnetisation measurements made with a vibrating sample magnetometer can be very useful for such analysis. As has been shown in chapter 3 the critical current density of the material under question may be determined as a function of applied magnetic field and temperature without the complication of contacts on what are often small samples. This method does not require D.C. transport currents of up to several hundred amps, which have many problems associated with them [1].

This chapter presents magnetisation data from several superconducting materials taken in the Durham high field magnet system, and various problems that have been encountered with the measurements are highlighted. Early magnetisation measurements are presented on a multifilamentary wire of the low temperature superconducting alloy niobium-titanium. This material has been widely studied previously and the implications of these measurements on the system is discussed. Magnetisation measurements on the same wire with and without the copper matrix, taken after improvements to the VSM are presented and discussed. A silver clad tape of a bismuth based high temperature cuprate superconductor has also been measured at high fields. While this material is not comprehensively understood the data do point to some problems with the apparatus. The final measurements that are presented were made on a high temperature $Bi_2Sr_2CaCu_2O_x$ superconducting multifilamentary wire. The magnetisation data has been used to calculate the magnetisation critical current density by using the critical state model. This is compared and contrasted to transport critical current density data. At the end of the chapter there is a summary of the work, and the conclusions that may be drawn.

7.2 Niobium Titanium Multifilamentary Wire.

Niobium Titanium (NbTi) is an alloy of two elements, the superconducting properties such as critical temperature and upper critical field of the alloy are dependent upon the composition. The maximum critical temperature is approximately 10K for a Nb70at%Ti composition, and the upper critical field peaks at about 11T when the composition is Nb40at%Ti. Niobium-titanium alloys are used extensively in low temperature, high field superconducting applications. The wire measured here consists of 61 filaments of 28μm diameter Nb46.5wt%Ti within a copper matrix. It is from the same batch of wire used by Friend [2] for transport studies.

7.2.1 Early Experimental Measurements.

Measurements have been made on twenty 5mm lengths of the wire, complete with the copper matrix. The samples were aligned perpendicular to the applied field so that the current induced by the magnetic field would be along the length of the wire. These measurements were made before the low-field insert had been commissioned. Magnetic hysteresis was measured at 4.2K in the liquid helium bath, and in a 5Torr helium gas atmosphere every Kelvin from 5K to 9K. The first group of measurements were in applied magnetic fields up to 7T at a magnetic field sweep rate of 1.8T.min^{-1}. Representative data from 4.2K and 6K are presented in figure 7.1. The data at 4.2K shows monotonically decreasing hysteresis up to 7T, and the loop does not close. The hysteresis in the 6K data is zero to within the noise level at fields above 4.5T.

Figure 7.2 presents data on the wire samples at 4.2K and 6K in applied magnetic fields up to 13T, taken at a magnetic field sweep rate of 0.36T.min^{-1}. The data at 4.2K is fully reversible above 7.2T, which is well below 11T, the upper critical field for this wire measured through magnetoresistance [2]. At applied fields between 7.2T to 10T the reversible magnetisation shows curvature, but then the reversible magnetisation has a discontinuity. Above 10T the magnetisation is linear. This behaviour is mirrored in the 6K data, but at lower applied magnetic fields.

7.2.2 Discussion of Early Measurements.

In all the measurements that were taken very high noise at low magnetic fields ($B < 2T$) was observed. This has been attributed to flux jumping in the Nb_3Sn sections of the Oxford 15/17T magnet. This problem was solved in later measurements by the use of a low field insert (see chapter 4).

At applied magnetic fields below 4T the data sets taken with magnetic field sweep rate of $1.8T.min^{-1}$ agree with commonly found magnetisation behaviour for multifilamentary NbTi wires as reported elsewhere [3]. Fully reversible magnetisation is seen at applied magnetic fields above 4.5T at 6K. This is similar to the so-called "irreversibility line" seen in the high temperature ceramic superconductors. There is also a discontinuity in this reversible magnetisation. For the data taken with the magnetic field sweep rate of $0.36T.min^{-1}$ the features of both reversible magnetisation and a discontinuity in the reversible magnetisation are seen at both 4.2K and 6K.

It was observed at the time of the above experiments that the out of phase signal detected by the lock-in amplifier on the VSM was rather high, and sometimes higher than the in-phase signal. To check if this reversible magnetisation effect was due to setting the incorrect reference phase on the lock-in amplifier the magnetisation of a nickel sample was measured up to 15T. Above the magnetic saturation field the signal should be perfectly in phase. This was observed to be the case, and so the reference phase of the lock-in amplifier was eliminated as a cause of the observed reversible magnetisation behaviour.

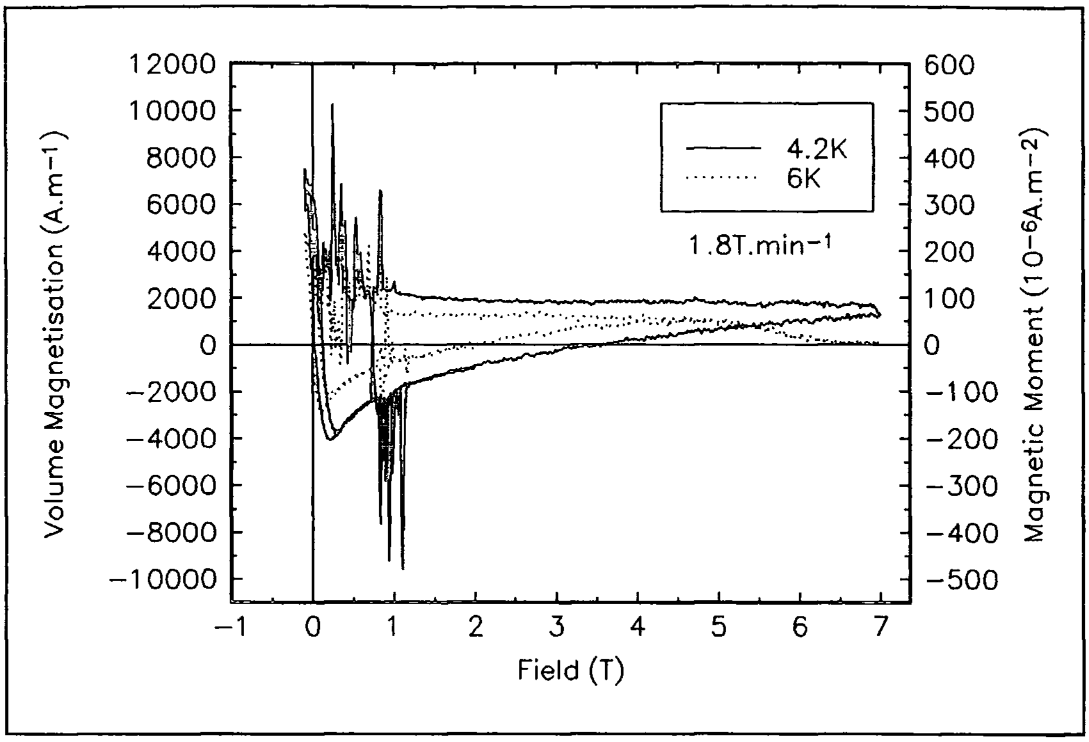

Figure 7.1 Magnetic moment of Nb46.5wt%Ti multifilamentary wire at 4.2K and 6K as a function of applied field.

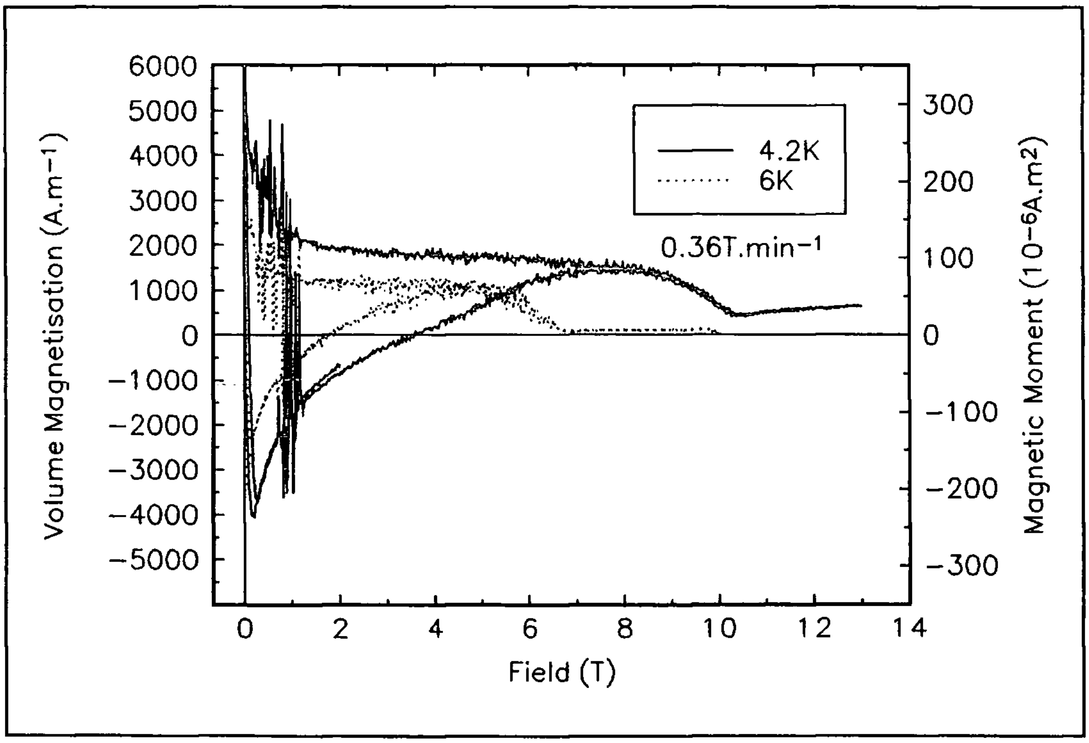

Figure 7.2 Magnetic moment of Nb46.5wt%Ti multifilamentary wire as a function of applied magnetic field.

7.2.3 Improved Experimental Measurements.

After the previous measurements the low field insert was commissioned in response to the high noise in the low magnetic field range. As further investigation into the high magnetic field effects a sample of identical wire that had its copper matrix removed was measured. The copper matrix was removed by immersing a length of the wire overnight in a 50:50 solution of nitric acid and distilled water. The sample consisted of 8 sets of the 61 filaments of niobium titanium, each set being 5mm long.

Figure 7.3 presents the magnetisation curves taken at 4.2K in applied magnetic fields up to 11.6T at a magnetic field sweep rate of 0.9T.min^{-1}. The solid trace is data from the same sample as measured in figures 7.1 and 7.2. Here the magnetisation becomes reversible at approximately 9T. The dotted line represents the results given by the sample with the copper matrix removed. At applied magnetic fields below 7T the volume magnetisation is slightly higher for the wire without the copper matrix. The magnetisation becomes reversible at the same field as the wire with the copper matrix. Curvature on the reversible sections is not seen in either sample. A discontinuity in magnetisation is seen at approximately 10T in the sample with the copper matrix. No such discontinuity is seen in the sample without copper matrix.

7.2.4 Discussion of Improved Measurements.

Data in the low magnetic field region has much lower noise due to the use of the low-field insert. For both samples the low-field and high-field sections of the hysteresis curve are consistent showing the quality of the measurements. There have also been improvements to the high magnetic field data. The magnetisation becomes reversible at 9T, and there is no large curvature on the reversible magnetisation. While this is better than without the low-field insert it is still somewhat below the reported B_{c2}. It is thought that this improvement in the high magnetic field data is due to the low-field insert restricting motion of the probe within the Oxford 15/17T magnet.

The measurement of the wire with the copper matrix removed was performed to check if currents in the copper were causing the reversible magnetisation effect. The data taken show that there is no difference in the onset of reversible magnetisation within the limit of the noise on the data. Therefore it is unlikely that the copper matrix is the cause. A discontinuity is seen in the reversible magnetisation for the wire with the copper matrix, at approximately 10T, but no such discontinuity is seen in the wire without copper matrix.

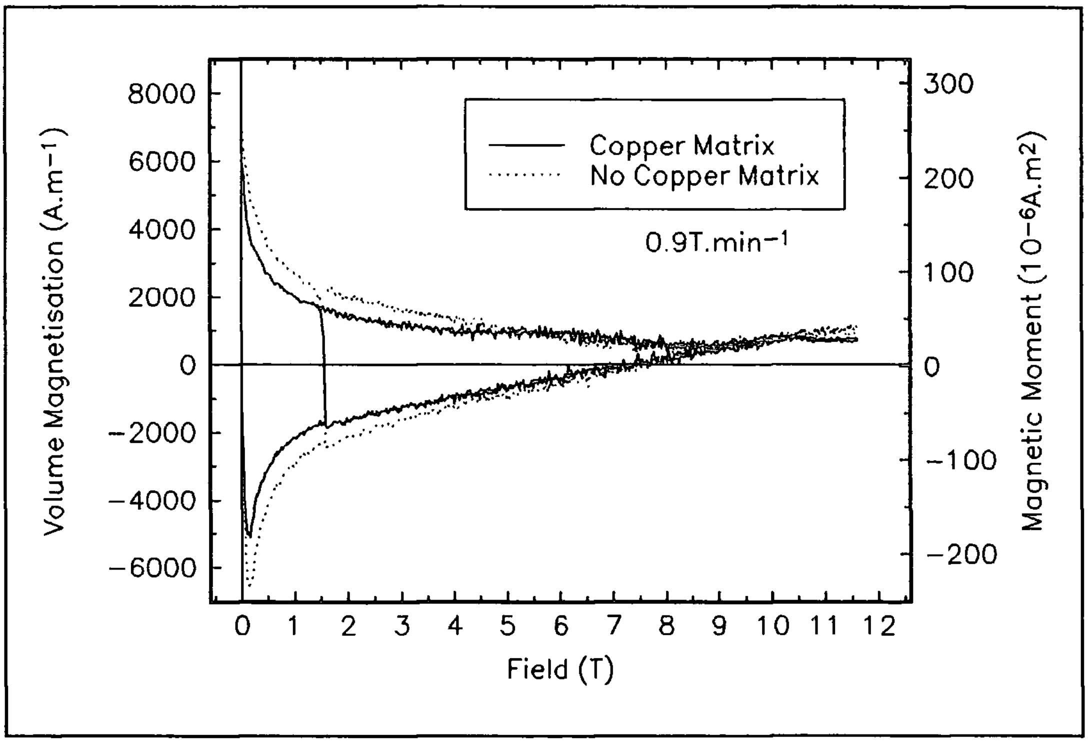

Figure 7.3 Comparison of NbTi wire with copper matrix and without copper matrix.

7.2.5 General Discussion.

It may be noted from all the data sets obtained that the magnetisation curves are not qualitatively the same at different values of magnetic field sweep rate for the same sample. (Compare figures 7.1, 7.2 and solid trace in figure 7.3). The magnetisation of multifilamentary NbTi wires has been reported elsewhere [3, 5] to depend not only on the magnetic field sweep rate but the twist pitch of the filaments. However, it is unlikely that these effects are caused by these variables, as they point to the wire being unstable above a certain sweep rate. Here it is observed to be similar at low and high sweep rates and different at an intermediate one.

The reversible magnetisation and discontinuity in reversible magnetisation shown in figure 7.3 may be seen in the data of Zheng [4]. The onset of reversible magnetisation occurs at 9T, a lower field than that the 9.5T found by Zheng for multifilamentary NbTi wires of unquoted composition. The discontinuity in the reversible magnetisation according to Zheng is a signature of the upper critical field. The value here is 10T at 4.2K. This is lower than the reported value of 10.5T [4]. There is reasonable agreement and so this point may be a signature of the upper critical field. If the discontinuity in the reversible magnetisation is a signature of the upper critical field then the result may be consistent with the data of Friend [2] for the identical wire, where removing the copper matrix is observed to increase the upper critical field of the wire.

In conclusion, improvements have been made to measurements on NbTi multifilamentary wires by addition of the low-field insert to the system. These improvements have eliminated the low-field noise due to flux jumping, and have restricted the motion of the probe relative to the Oxford 15/17T magnet at high magnetic fields.

7.3 $Bi_2Sr_2Ca_2Cu_3O_x$ Tape.

The group of superconducting ceramics of which $Bi_2Sr_2Ca_2Cu_3O_x$ is a member was discovered in 1988 [6]. Its high critical temperature ($T_c \approx 110K$) gives many possibilities for applications. This material is very anisotropic and for high current applications it is desirable to align the grains of superconducting material such that the current can flow along the a-b plane of the material. This can be achieved mechanically by making a flat tape sheathed in silver. This process is commonly known as the "powder in tube" method [7]. Using this method, lengths of tape measuring up to many metres carrying $10^4 A.cm^{-2}$ have been made [8].

The section of tape measured here was made via the powder in tube method by BICC Ltd. [9]. The dimensions of the tape were $4.0 \times 4.0 \times 0.5mm^3$ with the silver sheath, the superconductor itself was $4.00 \times 2.33 \times 0.02mm^3$. It had previously been measured for transport critical current density [10] and displayed a sharp increase in transport critical current density at applied fields below 1T and temperatures below 10K. The measurements here were intended to study this further by measuring the magnetisation critical current density.

7.3.1 Experimental Measurements.

Magnetic hysteresis was measured for the tape at 4.2K in two orientations. The first had the surface of the tape perpendicular to the applied field. The second had the tape surface parallel to the applied magnetic field, unfortunately it was not noted whether the drawing direction of the tape was parallel or perpendicular to the applied magnetic field.

Figure 7.4 presents the data taken on the tape with the applied magnetic field perpendicular to the tape surface. In this configuration the induced current will be in the plane of the tape, which is analogous to the transport measurement. In the low applied magnetic field ($B < 1.5T$) section the noise level is much higher than that in the high applied magnetic field data. The major and minor loops are not consistent in both halves of the trace which does imply that the operation of the low field insert and the associated power supply and control system may not be correct.

The magnetic hysteresis observed when applied magnetic field is parallel to the surface of the tape is presented in figure 7.5. The noise is at a level of approximately 4×10^{-6}A.m^2, which is about five times greater than that seen at high fields in the other orientation. The magnetisation is effectively reversible at applied magnetic fields above 3.5T. At 9T there is a discontinuity in the magnetisation. Again it is seen that the major and minor loops do not agree.

7.3.2 Quality of the Data.

The noise observed in the low applied magnetic field data when the tape surface was perpendicular to the applied field is similar in form to flux jumping in $YBa_2Cu_3O_7$ [11]. However as these features are confined to the section of the measurement on which the low field insert was used the problem should be assumed to arise from the low field insert. The hypothesis of the low field insert being the cause is strengthened by noting that in neither figure 7.4 or 7.5 are the major and minor loops consistent.

Very high noise has been found when the tape was measured with the applied field parallel to the surface of the tape. It is felt that this noise level may be caused by the detection coils moving with respect to the Oxford 15/17T magnet and the low-field insert. The discontinuity in magnetisation may suggest a sudden shift of position of components of the VSM relative to each other. Other data taken with the same sample did show definite jumps in the magnetisation at random values of high magnetic field. A possible solution for this is to prevent all components of the system moving relative to each other. This may be achieved through the addition of the stabilising spike and copper disks, as in chapter 4.

7.3.3 Discussion.

The purpose of the measurements was to look for a sharp increase in the magnetisation below 1T. From the analysis of the critical state model this would correspond to a large increase in transport critical current density observed in earlier measurements. This large increase in the magnetisation (and hence critical current density) is not seen when the surface of the tape is perpendicular to the applied magnetic field, the induced current being in the plane of the tape. Therefore the magnetisation data does not support the transport measurement in this instance, but further investigations are needed fully to investigate the effect. The magnetisation critical current density has been calculated to be 4×10^4A.cm^{-2} at 3T. This is similar to the critical current density as measured by transport current. This would discount a theory by which intragranular currents were responsible for most of the magnetisation critical current density.

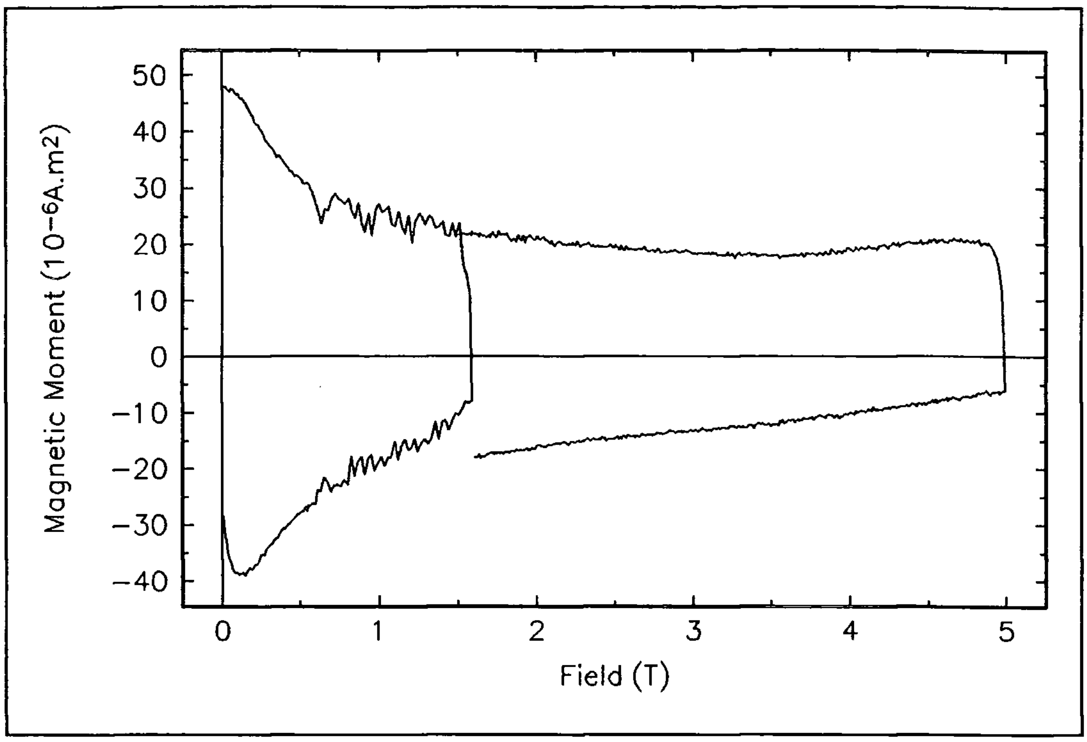

Figure 7.4 Magnetisation of a $Bi_2Sr_2Ca_2Cu_3O_x$ silver clad tape with applied field perpendicular to the tape surface.

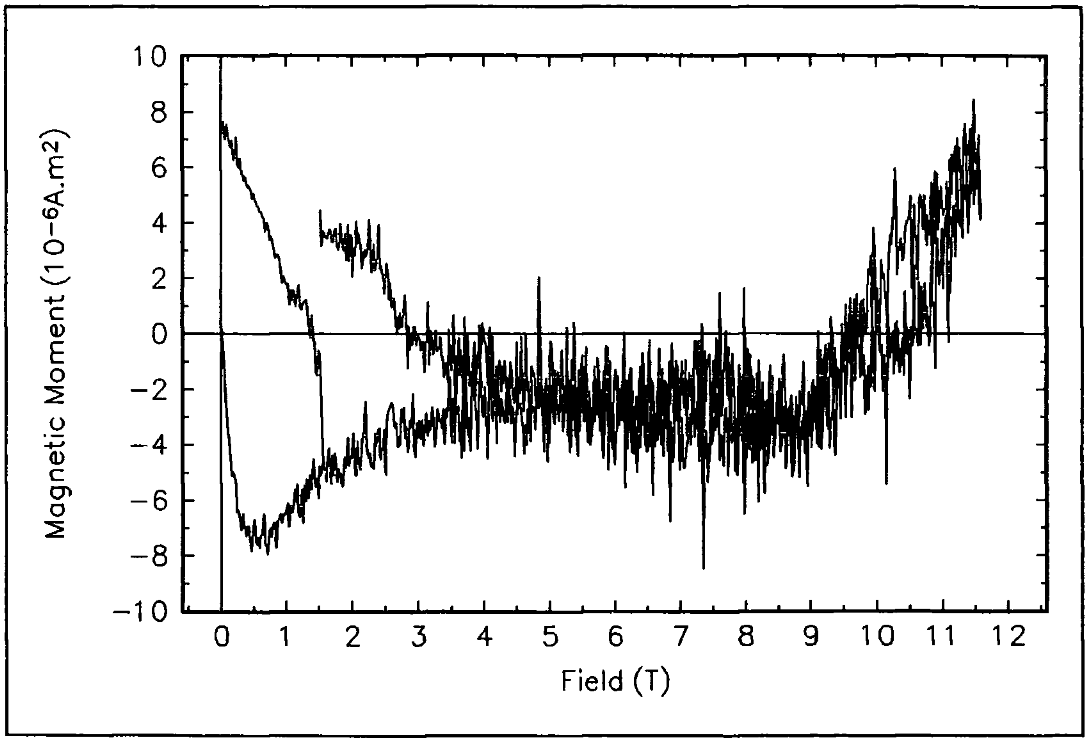

Figure 7.5 Magnetisation of a $Bi_2Sr_2Ca_2Cu_3O_x$ silver clad tape with applied field parallel to the tape surface.

7.4 Multifilamentary $Bi_2Sr_2CaCu_2O_x$ Wire.

In parallel with the developments of tapes of $Bi_2Sr_2Ca_2Cu_3O_x$ tapes (see previous section) there is also effort to make wires of the material that may be used for high current applications. For mechanical reasons silver is the preferred material for the matrix. The wire measured here was fabricated by Vacuumschmelze GmbH [12]. Single core silver sheathed wires are made from the appropriate oxide powders, in a similar procedure to the powder in tube method used to make $Bi_2Sr_2Ca_2Cu_3O_x$ tapes [7]. These are then bundled together in another silver tube which is drawn to make the multifilamentary wire.

7.4.1 Experimental Measurements.

Magnetic hysteresis has been measured for the wire at 4.2K. The wire was laid with its axis perpendicular to the applied magnetic field, in this orientation the induced current will be along the filaments of the wire. The measurement was done with an applied magnetic field sweep rate of $0.9T.min^{-1}$ and the maximum applied field was 11T.

The measurement is presented in figure 7.6. The high field noise is approximately $5\times10^{-6}A.m^2$. The magnetic hysteresis decreases monotonically at all fields, hysteresis being non-zero at the maximum applied magnetic field. Unlike the measurements on the $Bi_2Sr_2Ca_2Cu_3O_x$ tape (section 7.3) the major and minor hysteresis loops show excellent agreement with each other.

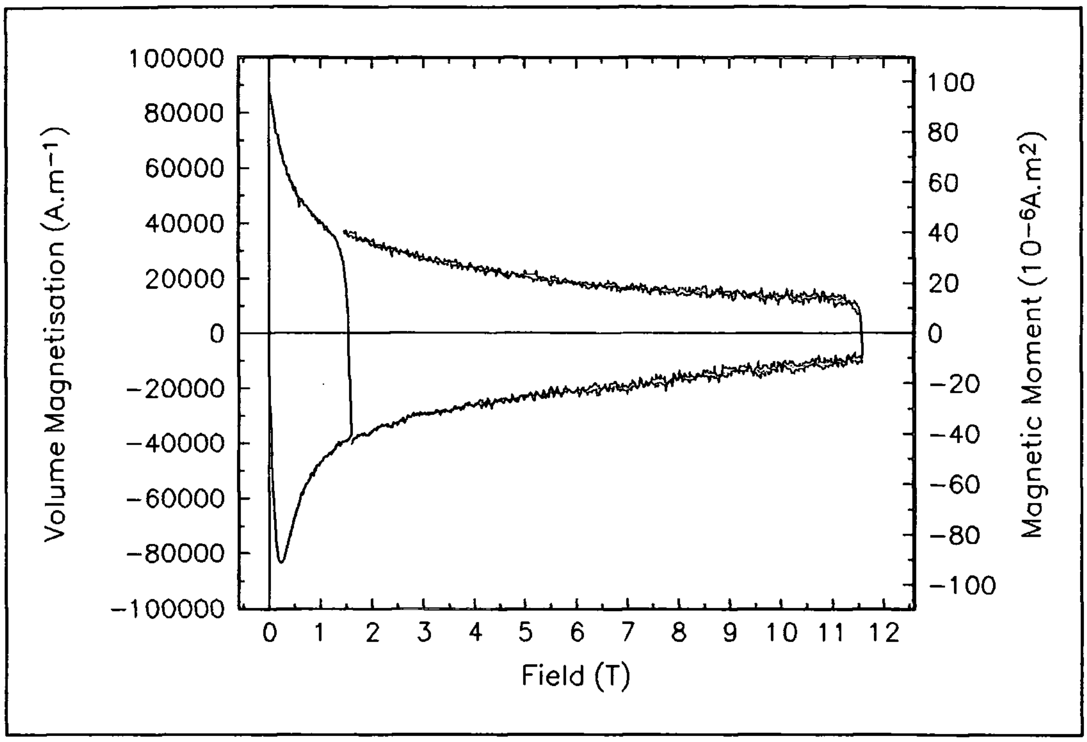

Figure 7.6 Magnetic hysteresis of a 19 filament $Bi_2Sr_2Ca_2Cu_3O_x$ wire at 4.2K.

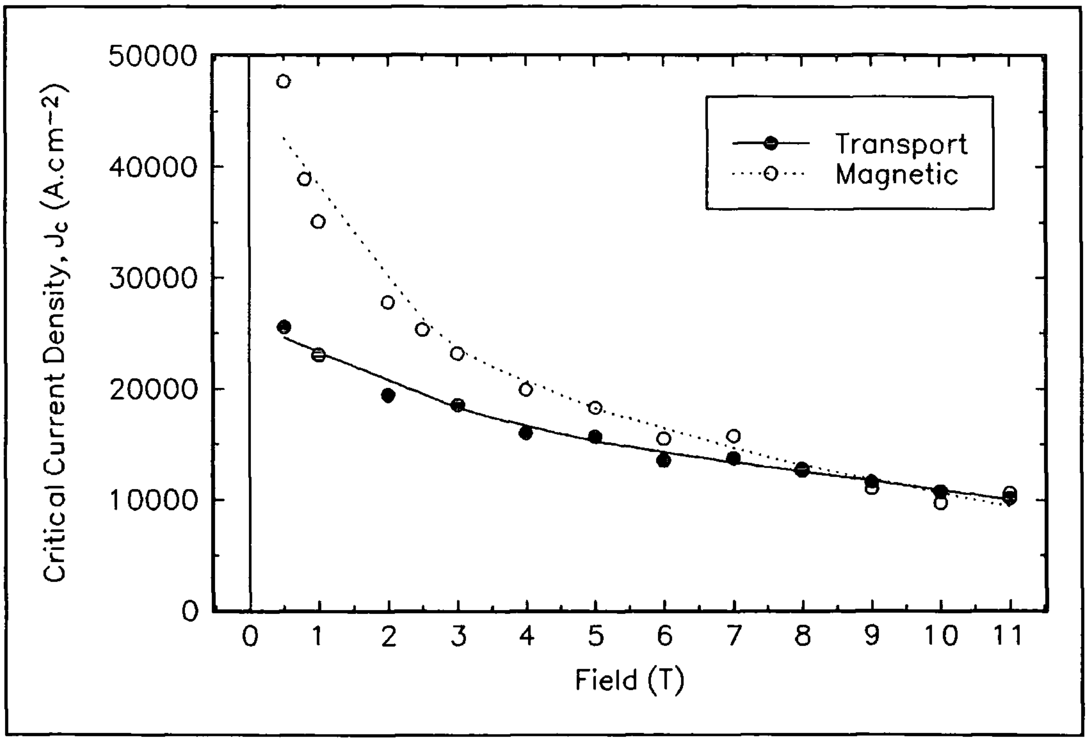

Figure 7.7 Comparison of transport and magnetisation critical current densities for a 19 filament $Bi_2Sr_2Ca_2Cu_3O_x$ wire at 4.2K.

7.4.2 Data Analysis.

Figure 7.7 presents magnetisation critical current density as derived from the magnetic hysteresis data. This was done using the critical state model [13] (see chapter 3). The magnetisation critical current density is related to the magnetic hysteresis by the equation:

$$J_{cM} = \frac{\Delta M}{a}$$

An appropriate value has to be chosen for ***a***, the length scale. In this case the sample is approximated to a bar $4.00\times0.53\times0.53\text{mm}^3$. Then the length ***a*** is given by:

$$a = \frac{1}{2}l_1\left(1-\frac{l_1}{3l_2}\right)$$

where $l_1 < l_2$ both being dimensions of the bar perpendicular to the applied magnetic field.

Also presented in figure 7.7 are transport critical current density data taken on the same section of wire by Friend [10]. The transport critical current data was determined at a voltage criteria of $2\mu\text{V.cm}^{-1}$. Using the analysis of Caplin et.al [14] the effective voltage criteria for the magnetisation measurements is $4.5\times10^{-2}\mu\text{V.cm}^{-1}$.

7.4.3 Discussion.

The measurement of the magnetic hysteresis of the wire shows that the combination of the high field magnet and low field insert is good. Noise in the measurement could probably be improved upon, following the suggestions of the stabilising spike and copper disks made in the previous section.

The calculations of magnetisation critical current density are of the same order of magnitude (10^4A.cm^{-2}) as the transport critical current densities. These are similar to the values quoted for similar wires elsewhere [15]. At fields below 9T the magnetically derived critical current density is higher than the transport, but at higher fields they are in agreement. It would be expected that the magnetisation critical current density is higher than the transport critical current density in a granular material such as this. The transport measurement measures only the current that can flow along the whole sample. The magnetisation arises from both currents flowing over the whole area of the sample and also within any individual grain.

Both measurements of critical current density have similar dependencies on the applied magnetic field, although the magnetisation critical current density decreases a little faster with magnetic field. Below 3T both measurements show an increase in the rate of change of critical current density with applied magnetic field.

7.5 Summary.

The vibrating sample magnetometer built in Durham has been used to make magnetisation measurements on several superconducting materials at high magnetic fields. High magnetic field measurements are necessary for a complete understanding of the superconducting state.

Early measurements made on a multifilamentary wire of NbTi were not successful due to two reasons. Firstly, there was very high noise observed in the low applied magnetic field region and secondly the magnetisation became reversible at fields much below the upper critical field. The copper matrix on the wire and the reference phase of the lock-in amplifier have been eliminated as causes of the problem at high magnetic fields. The addition of the low-field insert into the system eliminated the high noise in the low magnetic field range, and improved the high magnetic field data. The variable temperature work done on this wire up to T_c did show that as temperature increased the magnetic hysteresis decreased and the upper critical field shifts to lower fields as expected.

The $Bi_2Sr_2Ca_2Cu_3O_x$ tape sample that was measured showed up some problems with the measurement. These measurements suggest that the low field insert system may not be fully functional at all times and therefore investigations are needed of its smoothness and speed of magnetic field ramping. The noise was very high on the measurements. It is suggested that a solution may lie in ensuring that none of the constituent components of the system (detection coils, low field insert and Oxford 15/17T magnet) are able to move relative to each other. This has been attempted by the addition of the stabilising spike and copper disks to the probe. The work on the tape is inconclusive and other measurements will need to be done to see if the enhanced transport critical current density seen below 1T and 10K is accompanied by a similar enhancement in the magnetisation critical current density.

The 4.2K measurement on a sample of a multifilamentary $Bi_2Sr_2CaCu_2O_x$ wire showed that the system does work. The minor and major magnetisation loops were consistent with each other. Calculations of magnetisation critical current density are similar to transport measurements on the same sample, and wires measured by other groups.

7.6 References.

[1] C.M. Friend and D.P. Hampshire "A probe for the measurement of the transport critical current density of superconductors in high magnetic fields and at temperatures between 2K and 150K" *Submitted to Measurement Science and Technology.*

[2] C.M. Friend and D.P. Hampshire "Transverse and Longitudinal Critical Current Densities in Nb46.5wt%Ti multifilamentary wire from 2K up to T_c in Magnetic Fields up to 15 Tesla." *Applied Superconductivity vol.1 p.641.* ed. H.C. Freyhardt

[3] M.P. Mathur, M.S. Walker, D.W. Deis and C.K. Jones "Anisotropy of the critical current density in the NbTi filaments of round composite superconductors" *J.Appl.Phys.* **43** (1972) 3831.

[4] D.N. Zheng "An experimental study of flux pinning in high temperature superconductors" *Ph.D. Thesis, University of Cambridge, U.K.* (1994)

[5] M.P. Mathur, M. Ashkin and D.W. Deis "Scaling laws for flux pinning in Nb and NbTi multifilamentary superconductors" *J.Appl.Phys.* 45 (1974) 3627.

[6] H. Maeda, Y. Tanaka, M. Fukutomi and T. Asano "A new high-T_c oxide superconductor without a rare earth element" *Jap.J.Appl.Phys.* 27 (1988) L209.

[7] Y. Feng, K.E. Hautanen, Y.E. High, D.C. Larbalestier, R. Ray II, E.E. Hellstrom and S.E. Babcock "Microstructural analysis of high critical current density Ag-clad Bi-Sr-Ca-Cu-O (2:2:1:2) tapes" *Physica.C.* **192** (1992) 293.

[8] K. Sato, T. Hikata, H. Mukai, M. Ueyama, N. Shibuta, T. Kato, T. Masuda, M. Nagata, K. Iwata and T. Mitsui "High-J_c silver-sheathed Bi-based superconducting wires" *IEEE.Trans.Mag.* 27 (1991) 1231.

[9] T.P. Beales "Towards a high temperature superconducting power transmission cable" *Appl.Phys.Comm.* 12 (1993) 205.

[10] C.M. Friend "Transport Measurements of the Critical Current Density of Superconductors" *Ph.D. Thesis, University of Durham, U.K.* (To be submitted)

[11] J.L. Tholence, H. Noel, J.C. Levet, M. Potel and P. Gougeon "Magnetization jumps in $YBa_2Cu_3O_7$ single crystal, up to 18T" *Solid.State.Comm.* **65** (1988) 1131.

[12] J. Tenbrink and H. Krauth "Recent results on test windings and coils using Bi-2212/Ag HTSC wires" *ICMC'93, Albuquerque, USA.*

[13] C.P. Bean "Magnetisation of High-Field Superconductors" *Rev.Mod.Phys.* (1964) 31.

[14] A.D. Caplin, L.F. Cohen, G.K. Perkins and A.A. Zhukov "The electric field within high-temperature superconductors: mapping the E-J-B surface" *Supercond.Sci.Technol.* 7 (1994) 412.

[15] J. Tenbrink, M. Wilhelm, K.Heine and H.Krauth "Development of high-T_c superconductor wires for magnet applications" *IEEE.Trans.Mag.* 27 (1991) 1239.

8. Conclusions and Suggestions for Further Work.

In this thesis it has been shown that a superconductor is not simply a material with infinite electrical conductivity. The phenomenological theories of the London Brothers and Ginzberg and Landau have been covered. A description of the mechanism of superconductivity provided by Bardeen, Cooper and Schreiffer was introduced, along with predictions of superconducting properties that it made. However evidence suggests that this successful theory is not valid for the high-T_c superconductors.

The nature of magnetic flux entering a superconductor and its interactions with the material have been detailed. The Critical State Model, which describes magnetic hysteresis in superconductors has been covered in detail. It has been shown how this model may be used along with magnetisation measurements for a contactless determination of the critical current density.

The major part of this work has been the construction of the vibrating sample magnetometer (VSM) and its associated thermometry. Mathematical modelling of detection coil response has been very successful and resulted in excellent detection coil design, saving much time in development work. A probe has been designed and built that provides physical protection for the detection coils and the necessary electrical connections to them. A major noise problem due to flux jumping in the Nb_3Sn sections of the Oxford 15/17T magnet has been overcome by use of a low-field insert within the bore of this magnet. The VSM has been calibrated against the saturation magnetic moment of nickel. Consideration of the calibration and the noise levels achieved leads to the conclusion that the VSM's sensitivity is 10^{-6}A.m^2.

The other purpose of the probe is to provide a closed variable temperature environment for the sample, within a 20mm diameter. The probe has been designed to minimise the heat leaks out of the sample space in order to reduce the boil-off rate of liquid helium. The greatest difficulty has been ensuring that the sample and the probe's temperature sensors are in thermal equilibrium. This has been investigated length. A method of ensuring temperature measurement accurate to ±200mK has been found to work over the following ranges: 77K to 130K from a liquid nitrogen base and 4.2K to 30K from a liquid helium base. For measurements in other temperature ranges it is necessary to mount a carbon-glass temperature on the sample holder itself.

The VSM has been used to study the magnetic response of single crystals of $YBa_2Cu_3O_{7-\delta}$ grown at the U.K. National Crystal Growth Facility for Superconducting Oxides at the University of Birmingham. They were measured from 77K to 95K in applied magnetic fields up to 200mT. From measurements of the critical temperature and the magnetisation critical current density it is concluded that crystals grown under identical conditions do not have identical superconducting properties.

A limited range of magnetisation measurements have been made on several materials with the VSM in high magnetic fields. Studies of multifilamentary niobium-titanium wires have prompted major improvements to the VSM, namely the addition of the low-field insert which has reduced both low field and high field noise. Apart from eliminating the flux jumping in the Oxford 15/17T magnet it restricts relative motion of the detection coils and magnetic field. The need for further restriction has been highlighted by measurements on a $Bi_2Sr_2Ca_2Cu_3O_x$ tape that displayed discontinuities in the magnetisation. This further restriction has been supplied by copper disks and the stabilising spike. The measurements on the tape also raise questions about the reliability of the low-field insert system. The final group of measurements were made on a multifilamentary $Bi_2Sr_2CaCu_2O_x$ wire. Transport and magnetisation critical current densities for the same wire compare well, as they do with values for other wires.

Future work on the VSM should focus on fully testing temperature measurement and control when the carbon-glass sensor on the sample holder is used, and improving the sensitivity of the magnetic moment measurement. Sensitivity may be improved by the addition of the copper disks and the stabilising spike, which have not yet been tested at high magnetic fields. These will prevent the detection coils moving relative to the outside of the probe. It may also be advantageous to ensure that the probe, low-field insert and Oxford 15/17T magnet cannot move relative to each other.

To make operation of the probe easier the length of the probe and the sample rods should be reduced as much as possible. This along with replacing the brass sample rods with rods made of carbon fibre should help to ensure that the vibration of the sample is truly vertical, which may result in enhanced sensitivity of the instrument. Carbon fibre is a possibility for sample rods that has not been investigated. As carbon fibre is both light and non-flexible it may be better than the brass currently in use.

Appendix A - Flux Jumping in Superconductors.

A1. What is a Flux Jump?

A flux jump is a spontaneous, violent movement of flux into a sample [1] (c.f. flux creep which is a gradual process [2]). The effects of a flux jump may be seen on an M(B) trace as in figure A.1.

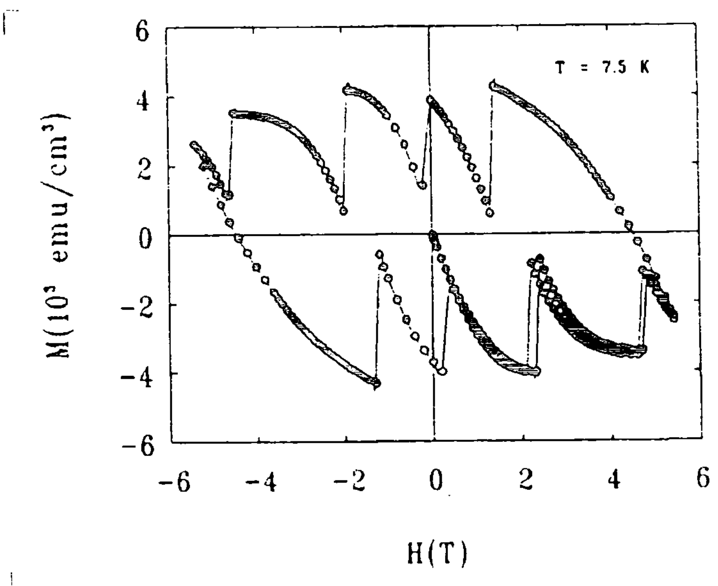

Figure A.1 Flux Jumping in a bulk sample of $YBa_2Cu_3O_{7-\delta}$ [3].

There are two properties of the superconductor that contribute to this effect [4]:-

a) the critical current density (J_c) decreases as the temperature (T) increases,

b) flux motion in the sample generates heat.

If one considers a slab of superconductor given a small heat pulse then the resulting temperature rise causes the critical current to fall, forcing the screening currents to decay. This allows magnetic flux to penetrate further into the slab, the flux motion leading to heat input feeding the process. Once this has started the process will avalanche and a flux jump results.

A2. The Adiabatic theory of Flux Jumping.

The adiabatic theory assumes that there is no heat exchange with the surroundings, i.e. the magnetic diffusion time is much less than the thermal diffusion time. This is an extension of Bean's Critical State Model [5], called the adiabatic critical state [6]. There are two ways of analysing the model, both assuming that $J_c(T)$ is linear, the first being a field dependent analysis [7]. This predicts a "fluxjump field" (B_{fj}) above which there is a danger of flux jumping.

$$B_{fj} \geq \sqrt{3\mu_0 c(T_c - T_0)} \tag{1}$$

An alternative analysis by Wilson [4] is based on a dimensional approach. If the "stability parameter" (ß) is greater than 3 then flux jumps may occur.

$$\beta = \frac{\mu_0 J_c^2 a^2}{C(T_c - T_0)} \tag{2}$$

If one re-arranges (1) and (2) then equates:

$$B = \mu_0 J_c a \tag{3}$$

i.e. the critical field is equal to the full penetration field. What this means is that if full penetration can be reached without flux jumping then the danger of flux jumping decreases. This means that stability may in theory be achieved by the use of fine wires. For NbTi the critical diameter at 6T is 230μm, while at 1T it is 68μm. This is not very practical.

A3. Methods of achieving stability.

The specimen size may be reduced below the critical dimension by using multi-filamentary wires. These consist of many fine filaments of the superconductor within a copper matrix. To prevent coupling between the filaments they are twisted, such that the E-field between the filaments reverses every half twist pitch.

Another advantage of the copper in the multi-filamentary wire is that it may act as a heat sink to the helium bath, conducting heat away before the jump avalanches. This is helped by the fine nature of the filaments within the wire as the greater surface area allows more efficient heat transfer.

The final method for eliminating flux jumps is to make a material such that:

$$\frac{\partial J_c}{\partial T} \geq 0 \qquad (4)$$

i.e. an increase in temperature gives an increase in J_c. An example of this is an alloy of (57 at.% Pb, 22 at.% In, 21 at.% Sn) [8].

References - Appendix A

[1] A. Gerber, J.N. Li, Z. Tarnawski, J.J.M. Franse and A.A. Menovsky "Magnetic instabilities in high-temperature superconductors under rapidly varying magnetic fields" *Phys.Rev.B* **47** (1993) 6047.

[2] P.W. Anderson "Theory of Flux Creep in Hard Superconductors" *Phys.Rev.Lett.* **9** (1962) 309.

[3] K.Chen, S.W. Hsu, T.L. Chen, S.D. Lan, W.H. Lee and P.T. Wu "High transport critical currents and flux jumps in bulk $YBa_2Cu_3O_x$ superconductors" *Appl.Phys.Lett.* **56** (1990) 2675.

[4] M.N. Wilson "*Superconducting Magnets*" Oxford University Press, UK.

[5] C.P.Bean "Magnetisation of Hard Superconductors" *Rev.Mod.Phys.* **36** (1964) 31.

[6] P.S. Swartz and C.P. Bean "A Model for Magnetic Instabilities in Hard Superconductors: The Adiabatic Critical State" *J.Appl.Phys.* **39** (1968) 4991.

[7] S.L. Wipf "Review of stability in high temperature superconductors with emphasis on flux jumping" *Cryogenics* **31** (1991) 936.

[8] J.D. Livingston "Flux Pinning by Superconducting Precipitates" *Appl.Phys.Lett.* **8** (1966) 319.